Single Cell Study of Malaria and Antimalarial Drug Impacts on Platelets and Mast Cells

A DISSERTATION
SUBMITTED TO THE FACULTY OF THE
UNIVERSITY OF MINNESOTA
BY

Kang Xiong-Hang

IN PARTIAL FULFILLMENT OF THE REQUIREMENTS
FOR THE DEGREE OF
DOCTOR OF PHILOSOPHY

Christy L. Haynes, Adviser

December 2020

Acknowledgements

Graduate school is an adventure where there are combinations of excitement, unforeseen and unpredictable outcomes, stress, frustrations, challenges, and rewards. My graduate school journey would not have been successful without the supports of my advisor Christy L. Haynes, colleagues, families, and friends. Christy has helped me to become the scientist I am today. I am thankful for her guidance and the many discussions and encouragements during times when life was difficult, and research seems impossible. I am thankful for her cheers and every support to make my journey possible.

In the Haynes lab, I am thankful to all the group members for providing me insights and feedbacks on my graduate works. Specifically, I am thankful to my two mentors Solaire Finkenstaedt-Quinn and Sarah Gruba, who trained me when I first started in the Haynes lab. I am thankful to Amani Lee who I have known since the start my graduate school and my go-to person for data analysis and computer questions. I am thankful to Jiayi He for spending her first year in lab with me trying to troubleshoot cyclic voltammetry issues. I am thankful to Audrey Meyer for her help in troubleshooting mast cells measurements with me, for advocating for my internship at Boston Scientific, and for being a great mentor.

Finally, I am thankful to my family. I am thankful to my husband, Ying Hang, for always encouraging me to keep going when I feel like giving up. I am thankful to my brother, Fue Xiong, for his support when I was young and for his encouragement to pursue higher education. I am extremely grateful to have someone to spark an interest in higher education in me and someone to keep encouraging me to reach my goal. What follows are acknowledgements for the technical assistance and funding for each chapter.

Chapter 2

Dedication

This thesis is dedicated to my spouse, Ying Hang, who has always encouraged me to shoot for the farthest star.

Abstract

Platelets and mast cells are among the first responders against foreign substances within a biological system. Understanding how the fundamental mechanisms of these two cell types act in a diseased vs. healthy environment is particularly important for any therapeutic approach. By using an electrochemical single cell technique, carbon-fiber microelectrode amperometry (CFMA), platelets and mast cells were studied during malaria infection. Lastly, platelets were studied for their response to two common antimalarial drugs using the same single cell technique.

Chapter 1 gives an overview of single cell analysis techniques (optical, electrochemical, mass spectrometric, and microfluidic methods) and their recent progress in biological applications. Single cell analysis techniques allow not only for quantification of intracellular biological molecules, but also for characterization of dynamic cellular processes with ultrahigh spatiotemporal resolution. Thus, the obtained information allows for analysis of fundamental mechanisms underlying cellular behavior and function.

Chapter 2 focuses on platelets and malaria and established the malaria model that will also be used for mast cells and malaria studies in Chapter 3. Chapter 2 starts with an emphasis on creating a live malaria-infected mouse model system and establishing two distinct stages of infection (ascending and descending parasitemia). Then, the chapter goes into detail about the use of CFMA to capture information on how platelets from malaria-infected conditions were impacted compared to platelets from malaria-free mice.

Chapter 3 focuses on mast cells and malaria and a comparison to platelets data in Chapter 2. The work in this chapter first involves obtaining mast cells from malaria-infected and healthy mice and co-culturing the mast cells with fibroblast cells to achieve successful primary culture for single cell studies. Then, the chapter details the use of CFMA to obtain relevant biological information about mast cells in the context of malaria. Finally, the chapter concludes with a comparison to the information obtained from platelets.

Chapter 4 focuses on platelets and their response to two select antimalarial drugs. The selected drugs are commonly used drugs to treat malarial infection by targeting the lifecycle of the malarial parasites. The work in this chapter involves using CFMA and a bulk electrochemical technique to study the effect of chloroquine and quinine on platelets and to obtain relevant biological information about platelet performance during malaria treatment. In all, CFMA as a single cell technique was able to reveal that platelets and

mast cells were affected at the fundamental level in the context of malaria and antimalarial drugs.

Table of Contents

List of Tables

List of Figures

List of Abbreviations

A-β	Amyloid-β
ACh	Acetylcholine
ACD	Acid citrate dextrose
ANOVA	Analysis of variance
CARS	Coherent anti-stokes Raman spectroscopy
CE-ESI	Capillary electrophoresis electrospray ionization
CFMA	Carbon-fiber microelectrode amperometry
CMOS	Complementary metal-oxide-semiconductor transistor
CNTs	Clostridial neurotoxins
CTCs	Circulating tumor cells
CQ	Chloroquine
ECL	Electrochemiluminescence
EDTA	Ethylenediaminetetraacetic acid
ESI	Electrospray ionization
FSCV	Fast scan cyclic voltammetry
FET	Field effect transistors
GCIBs	Gas cluster ion beams
IVIEC	Intracellular vesicle impact electrochemical cytometry
GI-SIM	Grazing incidence structured illumination microscope
GluOx	Glutamate oxidase
HPLC	High performance liquid chromatography
5-HT	5-hydroxytryptamine
IACUC	Institutional animal care and use committee
IL-8	Interleukin-8
iRBC	Infected red blood cell
MALDI	Matrix-assisted laser desorption
MAMS	Microarray for mass spectrometry
MCs	Mast cells
MRP1	Multidrug resistance-associated protein 1
MS	Mass spectrometry
NIMS	Nanostructure initiated mass spectrometry
NIR	New near-infrared (NIR) fluorescent
P. chabaudi	*Plasmodium chabaudi*

PALM	Photoactivation localization microscopy
PF4	Platelet factor 4
QN	Quinine
SNOM-MS	Scanning near-field optical microscopy-mass spectrometry
SECM	Scanning electrochemical microscopy
SICM	Scanning ion-conductance microscopy
3D-SIM	Three dimensional structured illumination microscope
SIM	Structured illumination microscope
SIMS	Secondary ion mass spectrometry
STED	Stimulated emission depleted microscopy
STORM	Stochastic optical reconstruction microscopy
SRH	Stimulated Raman histology
SRS	Stimulated Raman scattering
TEM	Transmission electron microscopy
TOF	Time-of-flight
RBC	Red blood cell
VAMP-3	Vesicle-associated membrane protein-3
VEGF	Vascular endothelial growth factor

Chapter 1

Single Cell Analysis: Recent Advances and Future Developments
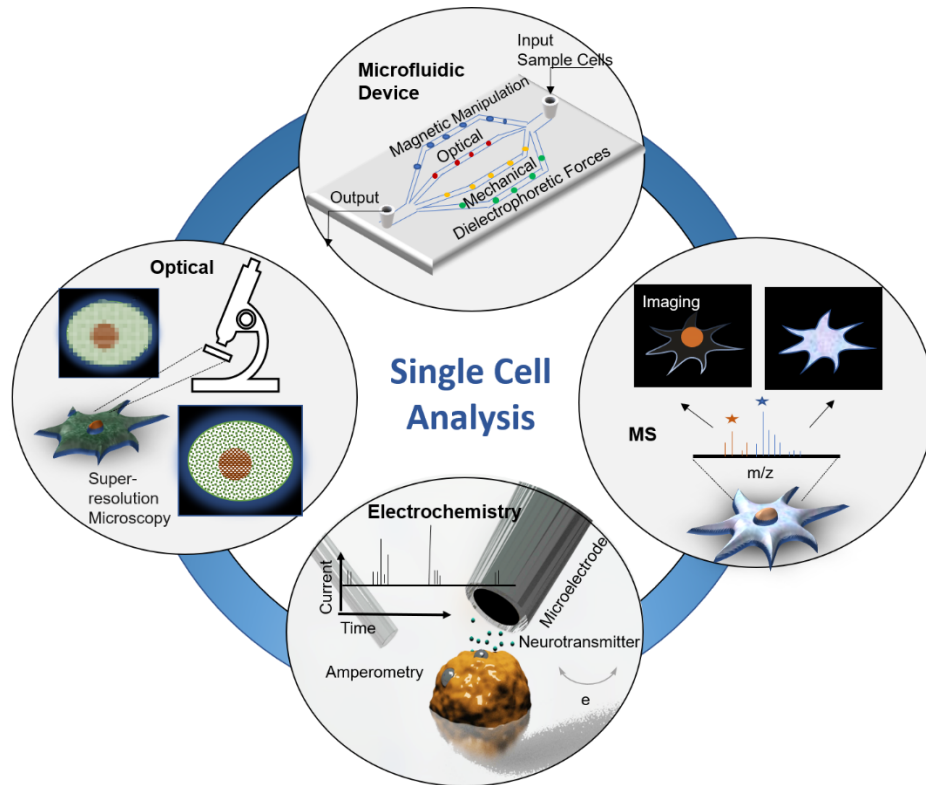
Kang Xiong-Hang, Jiayi He, Xiaojie Wu[1], Sarah M. Gruba[1], Anna C. Krieger, and Christy L. Haynes (Unpublished Manuscript)

[1]Parts of earlier drafts of this manuscript also appeared in Drs. Sarah M. Gruba and Xiaojie Wu's theses.

1.1 Overview

This chapter briefly describes single cell analysis techniques including optical, electrochemical, mass spectrometric, and microfluidic methods along with recent representative biological applications for the analysis of single cells using these techniques. Then, the chapter concludes with a summary of the current limitations, future challenges, and potential improvements. Analysis of the fundamental mechanisms underlying cellular behavior and function is one of the most important issues in cell biology and medicine. Conventional measurements based on pooled cell populations obscure detailed information about the biological events taking place inside single cells and important outlier cell subpopulations. Recent progress in single cell analysis techniques allows for the quantification of intracellular biological molecules as well as the characterization of dynamic cellular processes with ultrahigh spatiotemporal resolution. These techniques reveal nuances in cellular function and enable the detection of unknown cell subpopulations that are highly correlated to functional variations in tissues or organs.

1.2 Introduction

With the rapid development of new analytical techniques, the focus of biophysical and analytical chemistry has gradually shifted from investigating only ensemble cellular behavior and bulk cell contents to performing analysis at the single cell level. The motivation for this shift is attributable to two major factors. First, single cell analysis is one of the best ways to dig deeply into the features of a particular cell type, often revealing detailed real-time behavior or quantitative information. Second, even within a largely homogeneous cell population, subtle microenvironment changes or inherent stochastic factors in a small sub-population may result in cell cycle malfunction or disease state transition.[1-2] Exploration of these heterogeneities using single cell analyses will not only reveal mechanistic insights into the cellular behavior, but also may elucidate the relationship between cell-specific changes and biological phenomena pertaining to disease-related dysfunction. In recent years, state-of-the-art single cell techniques developed by analytical chemists have been used to characterize intracellular events pertaining to genes, proteins, metabolites, organelle function, as well as the subcellular dynamics, cell communication, and pharmaceutical effects.

This chapter will provide a review of recent single cell analysis developments during the past seven years in four major technical areas, including optical techniques,

electrochemical methods, mass spectrometry, and microfluidics. These areas of focus were chosen because they represent exciting analytical chemistry advances that have delivered previously unavailable biological insight. To maintain a reasonable scope, some gold standard methods, such as single cell transcriptomics, are not described herein, while less often discussed single cell analysis methods are introduced in detail. Excellent reviews on single cell transcriptomics can be found in published literature.[3-5] The optical techniques section describes the application of super-resolution fluorescence microscopy and coherent Raman scattering spectroscopy for single cell analysis, with an emphasis on tracking subcellular dynamics and intracellular chemical mapping. The electrochemical techniques include cyclic voltammetry, amperometry, field effect transistors, patch clamp, and electrochemical microscopy, with an emphasis on monitoring cellular communication as well as measurement of intracellular and non-electroactive species. Imaging-based mass spectrometry and mass cytometry approaches for intracellular molecule quantification at the single cell level are described in the third section. Finally, with the excellent ability to achieve single cell isolation in microchannels, the final section explores microfluidic-based single cell manipulation and detection. Finally, a perspective on single cell analysis including limitations, challenges, and potential improvements are discussed. Overall, single cell analysis techniques are important tools for understanding how cells work to impact disease and cellular function. In later chapters, the use of one electrochemical technique, carbon-fiber microelectrode amperometry (CFMA), will be used to understand platelets and mast cells in the context of malarial and anti-malarial drugs.

1.3   Optical Techniques

In recent years, the ability to image single cells has been extended to visually track subcellular dynamics with high spatiotemporal resolution and to quantify intracellular chemical species; meanwhile, structural and molecular information can be provided on essential cellular behaviors. Herein, two major categories of single cell imaging techniques, super-resolution fluorescence microscopy and coherent Raman spectroscopy, are introduced with illustrative examples of their recent applications.

1.3.1 Super-Resolution Fluorescence Microscopy

Super-resolution fluorescence microscopy, the subject of the 2014 Nobel Prize in Chemistry, overcomes the diffraction limit, achieving spatial resolution in the tens of nanometers.[6-7] Super-resolution fluorescence microscopy falls into two broad groups: one

approach uses special illumination patterns to spatially modulate fluorophores and the other relies on the stochastic nature of single-molecule switching. In both approaches, the captured images are then algorithmically reconstructed to surpass the diffraction limit.

Structured illumination microscopy (SIM) was first observed by Guerra through the fringes from two diffraction gratings with 50-nm-pitch, rotated with respect to one another.[8] In current methodology, SIM applies sinusoidal illumination patterns in phased rotation to excite the sample region of interest. The image is algorithmically reconstructed by analyzing the frequency information retrieved from each phase to typically achieve a two-fold lateral resolution enhancement over the traditional diffraction limit.[9-10] Because of the high speed and low phototoxicity of SIM, Li et al. recently employed the grazing incidence structured illumination microscopy (GI-SIM) method to visualize the dynamic interactions between organelles and the cytoskeleton to reveal a new endoplasmic reticulum interaction mechanism.[11] They also achieved sub-100-nm resolution with ultrahigh numerical aperture and non-linear SIM to image the dynamic assemblies of clathrin and caveolin near the plasma membrane during endocytosis (Error! Reference source not found.**A**).[12] This method measured the size of individual clathrin-coated pits and revealed details about the interactions between filamentous actin and clathrin. Three-dimensional SIM (3D-SIM) has been used for live cell imaging to provide better axial and lateral resolution by taking images at different focal planes.[13] Kraus et al. established a protocol for sample preparation and 3D-SIM mapping of nuclear structures in mammalian cells.[14] Banerjee et al. employed 3D-SIM to study key components involved in platelet endocytosis;[15] they found that the vesicle-residing protein, cellubrevin/vesicle-associated membrane protein-3 (VAMP-3) is critical in platelet endocytosis.

Stimulated emission depletion microscopy (STED) was first proposed by Hell et al. to overcome the diffraction resolution limit, achieving 35 nm spatial resolution in 1994.[16] STED relies on a pair of lasers to reduce the point spread function of the illumination light provided through a microscope objective. The first conventional laser beam stimulates a well-defined area of molecules to fluoresce, while a second doughnut-shaped de-excitation beam illuminates the sample to deplete the emission of the fluorophore outside the central region. Kamper et al. recently developed a new near-infrared (NIR) fluorescent protein, known as SNIFP, to act as a fusion tag for live human cells that can be used for STED microscopy in the NIR regime.[17] They also combined SNIFP with the traditional red fluorescent protein mCherry to facilitate dual color NIR-STED/red-confocal image for living cell and future deep tissue imaging (Error! Reference source not found.**B**).[17] Additionally,

the combination of STED with scanning fluorescence correlation spectroscopy has been used to characterize the interactions within lipid membranes. By tracking the diffusion of fluorescent phospholipid and cholesterol analogues in the plasma membrane of live cells, transient molecular interaction hotspots and mechanisms can be identified.[18] These observations would not be possible using only ensemble measurement techniques.

Photoactivation localization microscopy (PALM) and stochastic optical reconstruction microscopy (STORM) are single-molecule localization techniques that have quickly become mainstays of single cell analysis. PALM was first introduced by Betzig in 2006 when the group successfully imaged target proteins in subcellular organelles with a photoactivatable fluorescent probe at nanometer spatial resolution.[19] STORM was developed at nearly the same time by Zhuang's group and Hess et. al in 2006.[20-21] Zhuang's group used a photoswitchable cyanine dye pair (Cy3-Cy5) to image double-stranded DNA with ~ 20 nm spatial resolution.[20] The principle of these techniques is based on triggering the sequential on/off cycles of a series of sparsely distributed photoactivatable or photoswitchable fluorophores that are associated with the structure of interest. The super-resolution image can be reconstructed by processing thousands of image frames.[22-23] Puchner et al. employed the PALM technique to characterize the size of individual vesicles as well as the number of approachable phosphatidylinositol 3-phosphate (PI3P) binding sites they contain in the yeast endocytic pathway.[24] This work revealed the vesicle maturation trajectory by tracking the size change of vesicles and the temporal process of PI3K production. Zhuang's group pioneered 3D-STORM imaging of neurons with ~10 nm spatial resolution and revealed that actin, spectrin, and other associated proteins form a periodic skeletal structure in axons.[25] Their recent work provides a more detailed quantification of the periodic structure, demonstrating that the 2D polygonal lattice structure also exists in somatodendritic cells.[26] Recently, the unique capabilities of a multi-color STORM platform for screening neural circuitry in mouse retinae were reported. In this example, the synaptic input fields of neurons were mapped to explore the mechanisms behind direction-selective responses (**Error! Reference source not found.C**).[27] The combination of super-resolution PALM and STORM allowed Spahn et al. to image RNA polymerase, membrane, and chromosomal DNA in *E. coli*.[28] In this work, PALM provides quantitative super-resolution imaging of interacting proteins while STORM reveals precise structural information about the nucleoid, namely changes in structure depending on growth pace.
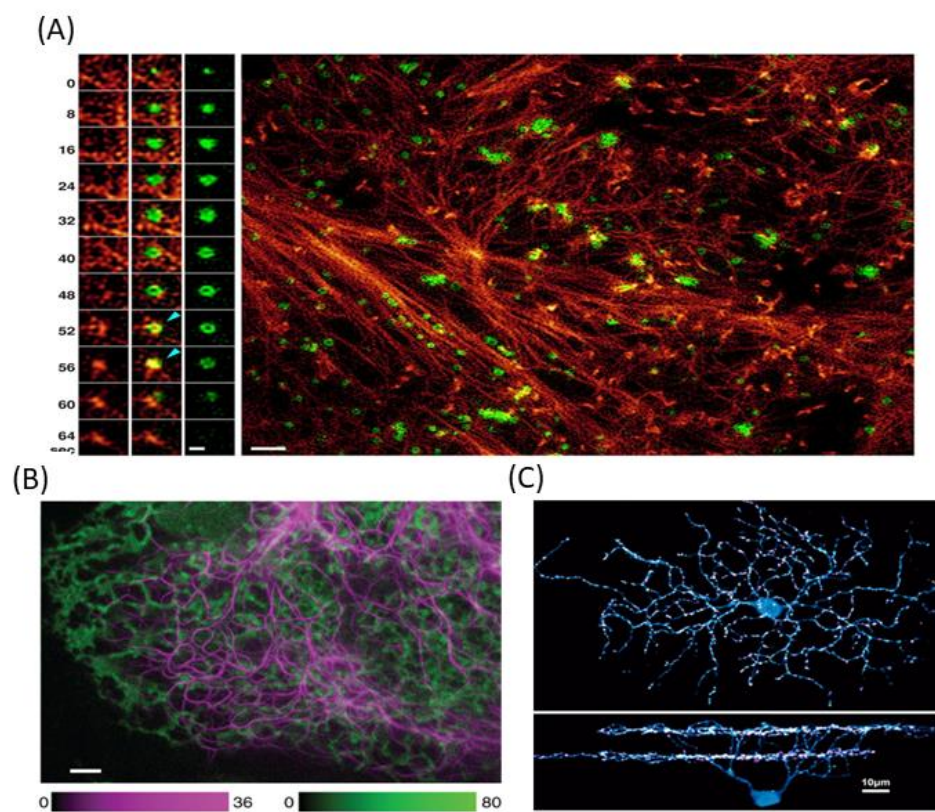
Figure 1.1. Super-resolution fluorescence microscopy for single cell analysis. (A) Left: SIM shows development of an individual clathrin-coated pit (green) and pit localization with cortical f-actin (red) in a COS-7 cell. (scale bar: 200 nm) Right: Image of one time point demonstrating the dynamics of individual clathrin-coated pits.[12] (scale bar: 1 μm) Reprinted with permission from Ref.12. Copyright 2015 American Association for the Advancement of Science. (B) Two-color NIR-STED/red-confocal microscopy of living human cells, mCherry fluorescent protein-labeled endoplasmic reticulum (green) and SNIFP fusion proteins (magenta).[17] (scale bar: 2 μm) Reprinted with permission from Ref. 17. Copyright 2017 National Academy of Sciences. (C) The top and side view of the STORM projection of a single cell (blue) with associated synaptic gephyrin (green) and presynaptic (magneta) clusters.[27] Reprinted with permission from Ref. 27. (scale bar: 10 μm) Copyright 2015 Elsevier Inc.

1.3.2 Coherent Raman Scattering Spectroscopy

Raman spectroscopy is a non-destructive and label-free measurement method that reveals the vibrational character of molecules upon laser excitation. One advantage of Raman spectroscopy is the ability to produce molecular "fingerprints" of small biomolecules inside single cells. However, the naturally weak signal and the slow Raman imaging data acquisition speed are often insufficient to capture intracellular dynamics. Coherent Raman scattering microscopy, developed for overcoming these limitations, is an approach enabling real-time imaging of vibrational signatures within single biological cells.

The coherent anti-stokes Raman spectroscopy (CARS) phenomenon was first observed in 1964 by Maker et. al.[29] and formally named ten years later by Begley et al.[30] CARS is a third-order nonlinear optical process requiring multiple laser inputs. The lasers interact with the sample to generate a coherent optical signal at an anti-Stokes frequency for a vibrational feature of interest. This signal is resonantly amplified when the frequency difference between the Stokes beams and the pump beam equals the frequency of a Raman-active vibrational mode.[31] One classical application of CARS spectroscopy is for lipid biology studies. Xie's group pioneered the imaging of lipid bilayers by tuning laser frequencies to highlight the aliphatic C-H stretching vibration frequency in live *Shewanella puutrefaxiens* bacteria.[32] Potcoava et al. used CARS to generate a lipid profile for breast and prostate cancer cells upon hormone treatment, indicating that hormone-treated cells had larger number and volume of intracellular lipid droplets compared to untreated controls in several cell lines.[33] This result may help explain the importance of lipids in drug resistance and cancer cell growth. Masia et al. used the CARS platform to identify two chemical components for phospholipidosis and steatosis and screened 15 drugs and neutral lipids for human HepG2 liver cells through the vector machine's analysis of spatial and spectral information.[34] They also demonstrated a volumetric quantitative CARS imaging method to identify the dry mass of lipid components in single human osteosarcoma (U-2 OS) cells (**Error! Reference source not found.A**).[35]

Similar to CARS microscopy, when the frequency difference between the pump and Stokes photons equals a specific molecular vibrational frequency, the Raman signal is amplified in stimulated Raman scattering (SRS) microscopy, another type of coherent Raman scattering microscopy originally discovered in 1962 during the operation of liquid filled ruby-laser cavity.[36-37] Instead of generating signal amplification at the anti-Stokes frequency, the signal amplification occurs at the frequency of the excitation beams for SRS imaging.[38] SRS microscopy has been used for detecting and imaging neurotransmitters[39] and landmark proteins associated with Alzheimer's disease[40] and brain tumors.[41] Xie's group employed multicolor SRS as a label-free method to visualize amyloid-β (A-β) plaque formation in brain tissue and to observe morphological changes.[40] These data suggested that Aβ peptide misfolding and the resulting insoluble plaques are hallmarks of Alzheimer's disease. They also developed an unique SRS processing technique called stimulated Raman histology (SRH) to image brain tumors and used a machine learning approach to distinguish different classes of brain tumors.[41] Fu et al. used the newly developed frequency-modulated spectral-focusing SRS to image a label-free small molecular

neurotransmitter, acetylcholine (ACh), in frog muscle; this approach shows great promise for future brain studies and imaging of other neurotransmitters (**Error! Reference source not found.C**).[39] Clearly, optical imaging techniques have advanced significantly in the last couple decades, making it possible to visualize dynamic molecular-level events within or on individual biological cells. The enhanced ability of these methods have made biological heterogeneity, and the importance of this heterogeneity, more obvious than ever. Similar to CARS microscopy, when the frequency difference between the pump and Stokes photons matches a particular molecular vibrational frequency, the Raman signal is amplified in SRS, another type of coherent Raman scattering microscopy originally discovered in 1962 during the operation of liquid filled ruby-laser cavity.[36-37] Instead of generating signal amplification at the anti-Stokes frequency, the signal amplification occurs at the frequency of the excitation beams for SRS imaging.[38] SRS microscopy has been used for detecting and imaging neurotransmitters[39] and landmark proteins associated with Alzheimer's disease[40] and brain tumors.[41] Xie's group employed multicolor SRS as a label-free method to visualize A-β plaque formation in brain tissue and to observe morphological changes.[40] These data suggested that Aβ peptide misfolding and the resulting insoluble plaques are hallmarks of Alzheimer's disease.

Figure 1.2. Coherent Raman scattering spectroscopy for single cell analysis. (A) CARS imaging of a U-2 OS human somatic cell in anaphase. Panel I shows the nuclear material (DNAP) in red and DAPI fluorescent molecular in blue, panel II shows C1 protein in green and Mitotracker

fluorescent probe in red.[35] (Note: scale bar not present in original publication.) Reprinted with permission from Ref 35. Copyright 2019 American Chemical Society. (B) Label-free two-color SRS image of misfolded amyloid proteins in brain tissue at 1658 cm^{-1} shift.[40] Reprinted with permission from Ref 40. Copyright 2018 American Association for the Advancement of Science. (C) Stimulated Raman scattering microscopy image of the acetylcholine (ACh) neurotransmitters in synaptic vesicles of frog neuromuscular junctions.[39] (Note: scale bar missing) Reprinted with permission from Ref 39. Copyright 2016 American Chemical Society.

1.4 Electrochemistry

Single cell electrochemistry is a powerful method to monitor cellular communication via exocytosis as well as ion channel function. Single cell electrochemical methods have also been employed to monitor various intracellular processes including generation of oxidative stress and oxygen consumption. With the use of micro- and nanoelectrodes, real-time monitoring of extracellular communication and intracellular contents can be accomplished with minimal cell damage.[42-44]

1.4.1 Voltammetry, Amperometry, and Intracellular Measurement

The most common electrochemical techniques in single cell measurement, namely cyclic voltammetry and amperometry, were made possible through pioneering work from Wightman and co-workers where stable, low current noise microelectrodes were originally used for measurements of neurotransmitters from individual chromaffin cells.[45] Since that early work, these methods have been used to monitor exocytosis in a variety of cells including mast cells, chromaffin cells, platelets, PC12 cells, and more recently BON cells (cells derived from a human carcinoid tumor) and Weibel-Palade bodies from endothelial cells.[46-53] These electrochemical methods give information pertaining to the concentration of electroactive molecules secreted and kinetics of secretion via the fusion pore. Fast scan cyclic voltammetry (FSCV), which capitalizes on the relatively broad range reactivity of the most commonly used carbon-based microelectrodes, is used to confirm the molecular identity of cell-secreted species by comparison to known voltammograms. In single cell studies, FSCV is often used (1) to confirm the electroactive species secreted from cells before performing carbon-fiber microelectrode amperometry (CFMA) or (2) in complex samples and cells that contain more than one electroactive species in the specified redox potential range.

The role of neurotransmitters in biological systems is often studied using FSCV. Pyakurel et al. recently developed a FSCV method to understand the role of octopamine in invertebrates.[54] Octopamine helps support locomotion, egg laying activity, learning,

memory, and courtship. This research on *Drosophila* indicated that octopamine is released through exocytosis, followed by a rapid clearance in the body. However, octopamine clearance was not accomplished using dopamine or serotonin transporters, and more work is needed to understand how the body takes up octopamine. Another neurotransmitter, adenosine, released by neurons, has been known for its role in duration and depth of sleep and seizures. Adamah-Biassi et al. used FSCV to analyze the role of adenosine fluctuations in Long Evans rats and found that adenosine release fluctuates after physical stimuli were monitored in the motor cortex and dorsal striatum.[55] In the study, using a tail pinch test, the amount of adenosine increased with a greater augmentation of adenosine in the dorsal striatum. These data suggest that adenosine has a dynamic role in response to external stimuli and may play a similar role to that of dopamine and norepinephrine. Adenosine has also been studied via FSCV for its role in patients with Essential Tremor undergoing deep brain stimulation which helps to reduce tremors.[56] From the study, adenosine levels increased to a maximum of 1.76 ± 0.99 μM compared to the normal basal levels of 20-200 nM after deep brain stimulation, along with releasing several other unidentified biologically active molecules.

CFMA, which enables sub-microsecond time resolution detection of redox-active species, is utilized for in-depth studies of exocytotic biophysical variations due to drugs, environment, disease, or membrane components. The technique involves placing an electrode near the cell surface with a constant applied potential while the change in current is measured over time, resulting in current spikes that correlate with individual granular release events. With the high temporal resolution, the stability of the exocytotic granule fusion pore opening and closing can be measured by observing features (known as "feet") that deviate from the standard current spike (**Error! Reference source not found.A**).[57-58] Recent research utilizing CFMA has focused on fundamental aspects of cell communication, including the impact of membrane components on exocytosis and cell communication changes in response to various diseases and drugs. The data collected gives a greater understanding of chemical messenger secretion and fusion pore opening and closing kinetics, including the stability of these processes.[59-62] The stability is studied by analyzing pre, post, and non-traditional secretion events. Figure 1.3A demonstrates an example of a traditional secretion event with both pre- and post-spike feet, which can indicate an inefficiency of the fusion pore during opening or closing, respectively. Finkenstaedt-Quinn et al. classified the differences in exocytotic event types.[57] In PC12 cells, and more recently, platelets, it was discovered that pre-spike foot events could be

characterized as a ramp, plateau, or a combination, suggesting distinct secretion profiles. In PC12 cells, a correlation between flux in the pre-foot and the flux in the spike was noted.[57, 63] Recent advances on the role of lipids in exocytosis have also utilized CFMA. Finkenstaedt-Quinn et al. have demonstrated the role of cholesterol on fusion pore stability by analyzing the changes in platelet foot features and non-traditional events as membrane cholesterol levels were varied.[57] These data show an increase in the percentage of platelets with foot features as cholesterol levels increase (**Error! Reference source not found.B**). This was primarily due to a greater number of platelet granules undergoing non-traditional secretion (**Error! Reference source not found.C**). The roles of phospholipids including phosphatidylethanolamine (PE) and phosphatidylserine (PS) on fusion pore kinetics and secretion have been studied using CFMA on PC12 cells and platelets. Results show that PE incubation causes changes in PC12 cell granule secretion time, and PS incubation causes changes in both platelet and PC12 cell secretion. In platelets, PS induced longer secretion times ($T_{1/2}$) and had a greater number of pre-spike features. In PC12 cells, the number of granule secretion events changed.[46, 63] These differences suggest that the role of phospholipids in exocytosis are complex and depend on other cellular components, but these roles would be immeasurable without fast and sensitive measurements like single cell CFMA.
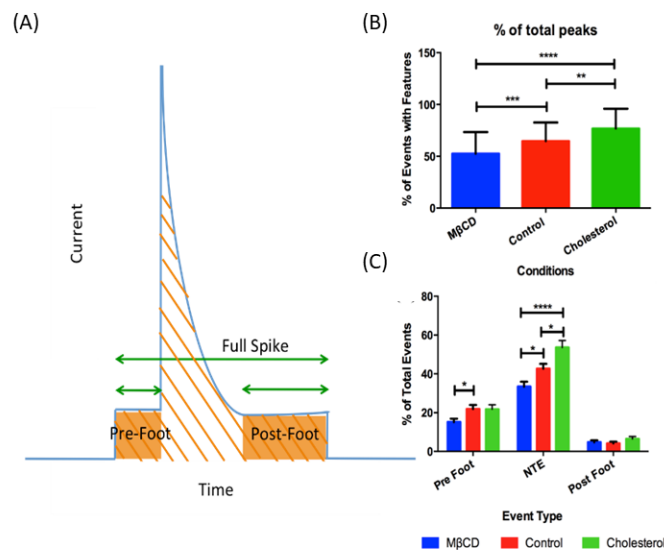
Figure 1.3. Pre- and post-foot schematic and variations in spike features due to cholesterol.[57] (A) Schematic showing terminology used to describe various current spike attributes. (B) The frequency of secretion events with pre- or post-spike features when platelets display different cholesterol levels, where the blue bar labeled with "MβCD" represents a cholesterol-depleted platelet, the red bar labeled with "Control" represents a platelet with unmodified cholesterol content, and the green bar labeled with "Cholesterol" represents platelets enriched with exogenous cholesterol. (C) Relative frequency of pre-spike feet, non-traditional

events, and post-spike feet when platelets display the different cholesterol levels. (*p ≤ 0.05, **p ≤ 0.01, ***p ≤ 0.001, ****p ≤ 0.0001) Reprinted with permission from Ref. 57. Copyright 2016 Elsevier Inc.

CFMA has also been used to study the effects of various disease-associated stimulants on exocytosis. Mast cells, a type of immune cell involved in asthma, secrete serotonin along with a variety of other chemical messengers when exposed to the common chemoattractants CXCL10 and CCL5. This secretion was marked by decreased serotonin secretion and prolonged kinetics of release when compared to stimulation of allergic reaction pathway exocytotic events without the additional chemoattractants.[64] Single cell CFMA can also be used to understand how diseases impact cell communication by comparing cells in a disease model to control cells. Manning et al. studied the effects of sickle cell disease on mast cells and found that mast cells associated with sickle cell disease had impaired serotonin secretion and variations in their biophysical kinetics; however, mast cells from sickle cell mice treated with morphine did not show a difference relative to control mice.[65] In later chapters, CFMA was used to explore platelet and mast cell exocytosis in the context of malaria for the first time.

While the exocytosis process of cells has been well-characterized using single-cell voltammetry and amperometry methods where the electrodes stay outside the cell, various electrochemical strategies have been developed to measure intracellular electroactive species as well. The study of intracellular electrochemistry gives significant insight on cellular function, especially for living cells. For example, Zhang et al. reported a unique SiC-core/carbon-shell designed to produce cylindrical nanowire electrodes with superior mechanical toughness and excellent electrochemical performance.[66] They applied the design to quantify reactive oxygen species (ROS) and reactive nitrogen species (RNS) in individual phagolysosomes of living macrophages and the measured amperometric spikes were attributed to the oxidation of ROS/RNS inside phagolysosomes when in contact with the inserted platinized electrode surface. Since the shell material can be tailored for various detection purposes, this electrode design can be applied to quantify other intracellular species as desired. Nascimento et al. presented nanopipettes functionalized with glucose oxidase on the tip to measure intracellular glucose levels in single cancer cells with high temporal and spatial resolution.[67] Glucose oxidase at the tip catalyzes the oxidation of bound β-D-glucose to D-gluconic acid, resulting in an impedance change due to the drop in pH at the nanopipette tip. A direct relationship between impedance changes and glucose levels indicate the reliable increase in glucose

levels of cancer cells compared to normal cells, which help to distinguish between the two cell types for future diagnostic applications. Ewing's group introduced a novel tool, intracellular vesicle impact electrochemical cytometry (IVIEC), to quantify the neurotransmitter content in a single vesicle without cell stimulation.[59, 68-70] A special nanotip conical carbon-fiber microelectrode was fabricated to penetrate cell membranes without inducing cell death to measure the total amount of electroactive neurotransmitters in individual PC-12 cell vesicles. By comparing the results from chemically stimulated exocytosis, they demonstrated that only ~64% of the catecholamine in each vesicle is released during exocytosis, supporting the conclusion that the intravesicular matrix does not fully expand during normal exocytosis. They also combined single cell amperometry and IVIEC to monitor the regulatory effects of lidocaine on neurotransmitter release from PC12 cells and found that low concentration lidocaine enhances exocytosis while high concentrations inhibits secretion. This biphasic effect is shown to be correlated with the size and duration of fusion pore opening as the intracellular granules fuse with the cell's plasma membrane. The combination of different characterization techniques provides a comprehensive understanding of the drug effects on cellular function. Pan et al. designed a novel nanocapillary coated with Pt for isolation of a single lysosome from a living cell and analysis of glucosidase activity within that lysosome.[71] The glucosidase activity was quantified through the generation of byproduct (hydrogen peroxide) from an enzyme-associated reaction.[71] The combination of sorting and assaying processes allow the analysis of multiple compartments from the same cell or the same compartment from different cells, which enables the direct study of heterogeneous protein function at subcellular resolution.

1.4.2 Field-Effect Transistors and Non-Electroactive Species Measurement

Pioneers such as Lilienfeld,[72] Heil,[73] and Shockley[74] were critical in the early development of field effect transistors (FETs). While not originally intended for single cell measurements, FETs can be used for the detection of cell-secreted electroactive or non-electroactive compounds with the use of antibodies (or other affinity agents) for target molecules. FETs consist of a source, a gate, and a drain. A voltage is applied to the gate, which can be functionalized with affinity agents specific to a non-electroactive molecule or protein of interest, changing the conductivity between the source and gate. Upon capture of the molecule or protein of interest, the conductivity change causes a measurable change in current between the source and drain. One type of FET used for single cell

exocytosis analysis is a single-walled carbon nanotube FET modified with anti-chromogranin A (CgA). CgA has several important biological functions including neuron inflammation mediation, assisting in the secretion of biomolecules after Ca^{2+} chelation, and is hypothesized to be a marker for neurodegenerative diseases. The use of FETs for measuring the secretion of non-electroactive CgA has been shown to be highly biocompatible, sensitive to low secretion concentration, and displays a correlation between conductivity and concentration in both neurons and single chromaffin cells.[75-76] Another non-electroactive species measurement example from Qiu et al. reported an enzymatic micro-biosensor to detect glutamate using glutamate oxidase (GluOx) and Pt nanoparticle-coated CFMEs.[77] Glutamate was transformed by GluOx, producing H_2O_2 which enables the indirect electrochemical measurement of glutamate's presence in a single neuron. With high sensitivity and spatiotemporal resolution, this sensor demonstrated great ability to detect this non-electroactive neurotransmitter at the single-cell level.

Recently, two FET platforms involving impedance spectroscopy with an ion-sensitive field-effect transistor have been used to study non-exocytotic cellular processes to understand the adhesion, apoptosis, and detachment of single cancer cells in response to nanoparticles and anti-cancer drugs. [78-80] Zhang et al. created a nanometric FET by coating a dual electrode for the source and drain with polypyrrole to form the transistor channel with a final diameter of 200 nm to study pH and ATP changes in cells (**Error! Reference source not found.**).[81] The pH sensor detects changes of ~0.1 pH units with a linear response between pH 5.0-7.5. The probe was used for the detection of pH in melanoma breast cancer tissue as well as on a single cancer cell. Typically, melanoma cells have more acidic environments than non-cancerous cells and researchers found that the probe was able to measure an increase in acidity in both the tissue and cluster of melanoma cells as it approached the cells. However, no decrease in pH was noted on a single cell level, which was likely due to the rapid diffusion of the proton not obstructed by other cells. With the addition of hexokinase (an enzyme that cleaves ATP and releases protons) to the tip of the nanometric-FET, the researchers also showed the applicability of this probe to detect the release of ATP at concentrations as low as 10 nM.
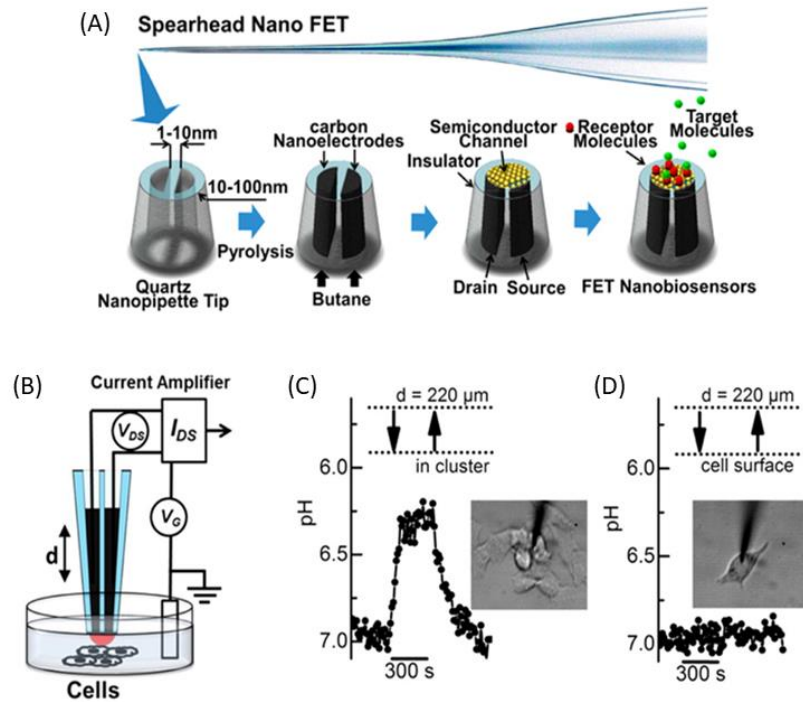
Figure 1.4. Nano-FET pH Biosensor.[81] (A) Schematic of the FET used for (B) local pH measurement in cell samples in (C) a cluster of melanoma cells and (D) a single melanoma cell. Reprinted with permission from Ref. 82. Copyright 2016 American Chemical Society.

1.4.3 Patch Clamp

Unlike FETs, patch clamp measures cell capacitance, which is proportional to the cell membrane surface area. In patch clamp, a gigaseal is formed between the cell and an electrolyte-filled pipette to reduce noise and prevent interference from ions in the extracellular solution. Neher and Sakmann first utilized patch clamp to monitor the ionic current from the membrane of frog muscle fibers.[82] Since then, two major patch clamp methods have emerged: cell-attached and whole-cell.[83-84] In the cell-attached method, the capacitance is measured on a small area of the cell, providing lower noise and greater sensitivity to small changes. In the whole-cell method, the entire cell's capacitance is measured, providing information on larger changes in the cell membrane area. Both methods are completed by puncturing the cell membrane with the pipette. To obtain in-depth information on exocytosis, either methods can be utilized in parallel with amperometry to obtain both fusion pore size and molecular secretion information.[83, 85]

Patch clamp can also measure the release of ions from ion channels located throughout the plasma membrane. Upon stimulation, the ion channels open and selectively allow ions to pass through based on charge and size, creating an electrical

signal. Since the gigaseal is formed over the ion channels of interest and the potential is held constant in the pipette, ions that pass through the channels induce changes in current that are measured. Nanopipettes combined with patch clamp for ultrafine probe positioning allows for precise ion channel scanning over the membrane and ample data collection.[86-87]

Beske et al. have shown the viability of using single cell patch clamp to replace the mouse lethality assay for determining the concentration of clostridial neurotoxins (CNTs) (bacterial-derived protein toxins including tetanus and botulinum) which cleave SNARE proteins.[88] Their results indicate that SNARE cleavage causes detectable changes in synaptic release. Over 99% of all spontaneous neurotransmission rates were eliminated after 20 hours of exposure to a variety of CNTs. In addition, patch clamp was able to distinguish differences in cells after exposure to the toxin in a variety of complex environments including pharmaceuticals (BOTOX), food products (milk, green beans, and apple cider), and human serum.

1.4.4 Electrochemical Microscopy

The two major electrochemical microscopy techniques used for studying single cells are scanning electrochemical microscopy (SECM) and scanning ion-conductance microscopy (SICM). In SECM, an ultramicroelectrode (UME) tip approaches a cell surface and records the electrochemical current signals with high accuracy probe tip positioning. SECM is a powerful tool to probe the topography and electrochemical activity of a cell surface by introducing a non-endogenous mediator that will do electrochemistry at the cell surface to allow for detection. The technique was first introduced in 1989 by Bard and coworkers to study various surfaces immersed in solutions.[89] Since then, work in biological samples ranging from a *Ligustrum sinensis* leaf,[90] mouse skin,[91] dentinal surface,[92] bone slice,[93] *Escherichia coli*,[94] to single protoplasts[95] have been completed. For comparison, SICM is a technique to monitor the ionic current and conductance between the two electrodes when the pipette tip approaches a generally non-conducting surface. The changes in the ionic microenvironment due to (electro)chemical reactions occurring at interfaces can be used by SICM to characterize surface electrochemical activity and map the detailed topography. SICM was introduced in 1989 by Hansma et al. to image electrolytic solutions.[96] Since then, improvements to SICM have been made to adapt to single cell imaging applications.[97-101] Both SECM and SICM are non-invasive techniques

allowing electrochemical detection with high temporal and spatial resolution, thus enabling biological function studies at the single-cell level.

For example, Polcari et al. reported the measurement of multidrug resistance-associated protein 1 (MRP1), the mediator of drug efflux in cancer cells, in individual cancer cells using SECM.[102] The SECM results indicated that functional activity of MRP1 adhering to the plastic substrate augments after the dimensions of the adhesive islands become smaller. The drug effect experiments indicate that expression and functional activity of MRP1 are not directly correlated, which suggests that the functional activity is an independent parameter to explain the response of cancer cells to chemotherapeutic treatment. A second example from Santos et al. developed a SECM system to monitor oxygen consumption characteristics, which is an effective manner to evaluate energy metabolism of single cells.[103] The system employed platinized Pt disc microelectrodes to measure oxygen concentrations and consumption rates with inter- and intra-cell heterogeneity in response to modifiers of mitochondrial oxygen consumption, CCCP and antimycin A. The method is comparable to the commercial gold-standard detection system and enriches the understanding of metabolic characteristics on a single-cell level.

In electrochemical microscopy, electronic noise can result in low chemical sensitivity; however, Sen et al. reported sensitivity improvement by using a combination of SECM-SICM using double barrel carbon nanoprobes deposited with Pt to increase the electrochemical signal and flux of chemicals species.[104] The optimized probe enables imaging of electrochemical features and spatial distribution of epidermal growth factor receptor on the membrane of the A431 cells. Similarly, Page et al. used dual-barrel SICM-SECM nanoprobes to measure the topography while monitoring the uptake of delivered molecules following delivery from the dual-barrel probes.[105] Specifically, they observed the uptake of hexaammineruthenium by single *Zea mays* root hair cells with qualitative probe current response and quantitative finite element method simulation. Electrochemistry methods have shown great ability for single cell measurements, ranging from direct detection of granule-by-granule secretion of electroactive chemical messengers as will be done in this thesis to capacitance measurements of the changes in an individual cell membrane to electrochemical imaging of cells in the presence of judiciously chosen electroactive species. As detection systems and electrodes continue to improve, the range of detectable molecules and the temporal resolution of these measurements will yield even more biological insights.

1.5 Mass Spectrometry

Mass spectrometry (MS) is a technique used to analyze the molecular species present in a cellular sample via the ionization and subsequent detection of fragment ions. Early developmental phases of electrospray ionization (ESI)[106] and matrix-assisted laser desorption (MALDI)[107-108] in MS to probe biomolecules have allowed for its extension into single cell analysis. Based on the ability to detect ions from the sample directly, MS often does not require labeling of the species of interest, allowing for both the detection of known and unknown ions, without theoretically limiting the number of different ions detected (accounting for the range of masses and resolution of the instrument). Mass spectrometers can be directly coupled with microfluidic devices, liquid chromatography, capillary electrophoresis, cell pressure probes, and nanoelectrospray tips.[2, 109-111]

1.5.1 Mass Spectrometry Imaging

To directly measure single cells within tissue samples, researchers often use MS imaging (MSI). MSI can be accomplished using a secondary ion MS (SIMS)[112] or MALDI[113] setup. These techniques allow for the detection of molecules, proteins, and unique lipid compositions that could be obscured in bulk analyses. Recently, mass spectrometric ionization methods under ambient conditions have been explored extensively and have created a subfield in MS. The rise in popularity of ambient ionization usage can be attributed to (1) no sample preparation is needed, (2) samples are not introduced into a vacuum environment, and (3) no matrix or tagging agents are required. Here, SIMS and MALDI will be discussed in detail, whereas ambient ionization MS and other MSI techniques can be found in other recent reviews.[114-116]

SIMS was first introduced in 1960 by Castaing and Slodzian to describe an electrostatic collection system.[117] In static SIMS and dynamic SIMS, the species on the top layer of the cell or several layers in the cell, respectively, can be identified. Dynamic SIMS is advantageous in that it gives a 3D picture of the cellular components. The bombardment of the surface with high-energy particles (typically Cs^+ or O^-) or clusters (Bi_3^+ and C_{60}^+) allows for the desorption of atoms, molecules, and clusters. The secondary ions produced from this process are then analyzed.[118-119] The layer thickness is typically several nanometers with a lateral resolution of $\leq$ 100 nm and attomolar detection limits. The high spatial resolution allows the concentration of various membrane components, including lipids and polysaccharides, to be analyzed on a single cell level. Medically, this

can be used to understand the impacts of disease on cellular membrane components or reveal disease biomarkers and to understand drug distribution.

Park et al. modified the traditional time-of-flight (TOF)-SIMs method to better differentiate ovarian cancer cells from control cells by using multi-dimensional SIMS (MD-SIMS).[120] In this method, samples first undergo TOF-SIMS then have gold deposited on them before a second SIMS analysis (metal-assisted-SIMS (MetA-SIMS)). The data showed that TOF-SIMS and MetA-SIMS identified 206 and 533 unique compounds, respectively, and 426 compounds were found in both methods with 250 signals enhanced using MetA-SIMS compared to TOF-SIMS. When comparing the results between cancerous and non-cancerous tissues using partial least square discriminate analysis, MD-SIMS enhanced the number of cancer cells discriminated from non-cancer cells from 68.4% with TOF-SIMS to 82.6%. (**Error! Reference source not found.**).[120]

Percent Variance Captured by PLS Model (A)

| | X-Block | | Y-Block | |
LV	This LV	Total	This LV	Total
1	46.47	46.47	40.98	40.98
2	7.89	54.36	15.25	56.23
3	5.74	60.11	12.18	68.40

Percent Variance Captured by PLS Model (B)

| | X1-Block | | X2-Block | | Y-Block | |
LV	This LV	Total	This LV	Total	This LV	Total
1	52.20	52.20	44.95	44.95	50.12	50.12
2	9.00	61.20	10.25	55.20	22.58	72.70
3	12.06	73.26	5.18	60.39	9.89	82.60
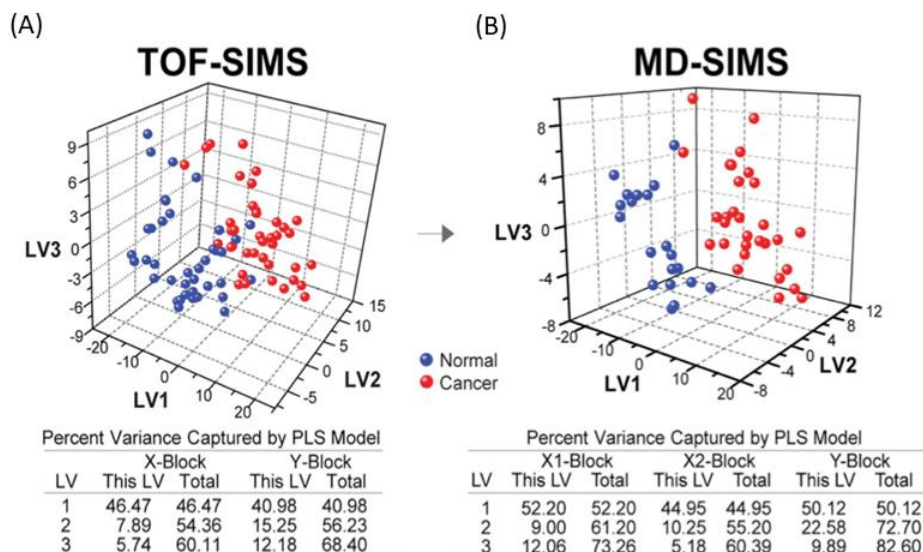
Figure 1.5. TOF- and metal assisted-SIMS integrated analysis.[120] 3-D partial least square-discriminate analysis score plots for (A) TOF-SIMS and (B) MD-SIMS. Tables below each plot show that multi-dimensional SIMS was better able to discriminate ovarian cancer samples (red) from non-cancerous cells (blue). Reprinted with permission from Ref. 120. Copyright 2015 Nature Publishing Group.

The ability to detect drug distribution and metabolism inside a cell is important to characterize drug efficacy. To locate and distinguish organelles of interest within a cell, Bloom et al. established a new technique using dye-enhanced imaging.[121] This technique uses a molecular tag that is detectable by SIMS, but provides spectra distinguishable from cellular components such as the phosphocholine head group and cholesterol. Using a

nuclear stain, the stain was verified to successfully display in the image. Utilizing this staining method, further studies can probe various biological pathways and drug uptake while being able to correlate detected species with particular organelles of interest. Bloom et al. have also used cluster SIMS for detecting the uptake and location of nanoparticles and subsequent delivery and degradation of the nanoparticle-delivered drug within the cell.[122]

MALDI imaging is another widespread approach with the ability to recognize subcellular structures and to reveal molecular changes at the single cell level. The MALDI concept initially reported in 1985 by Karas et al. revealed that wavelength impacts the desorption of ions from organic molecules. et al.[123] For MALDI, the sample to be analyzed is mixed with a matrix, usually containing an aromatic core that can absorb the energy of a pulsed laser beam. After laser irradiation, the energetic desorption of matrix together with the sample is triggered, and then the analyte molecules are ionized in the hot plume of ablated gases before entering the mass spectrometer. As one of the most powerful mass spectrometric techniques, MALDI imaging can achieve lateral resolution of 20 µm or less with high mass range. Hossen et al. developed MALDI imaging mass spectrometry (MALDI-IMS) to analyze the lipid status of multiple myeloma cells compared to that of normal plasma cells.[124] Individual multiple myeloma cells were purified by flow cytometry, and the MALDI-IMS results showed significantly lower levels of phosphatidylcholine in disordered vs. normal plasma cells based on peak intensity and ion signals. This study can serve as a suitable tool for single cell study and help to further understand multiple myeloma progression. Krismer et al. combined MALDI-IMS with high-throughput microarray sample-preparation technology to study over 25 various lipids and pigments in the *Chlamydomonas reinhardtii* as a time progression.[125] This study provided dynamic insights into phenotypic constituents and adaptions. Results indicated that, although genetically diverse cell populations generated equal or greater phenotypic variation vs. isoclonal cell populations, isoclonal cell population was significantly affected by non-genetic factors such as nitrogen stress. Clearly 20 µm spatial resolution is not ideal for cell imaging. As such, the efforts from several groups have greatly improved the spatial resolution of MALDI-IMS. Zavalin et al. combined a transmission geometry ion source with MALDI-ToF-MS to achieve sub-cellular spatial resolution.et al.[126] Using this geometry, images were obtained at a standard raster scan rate of 5 pixels/s and continuously at a rate of 40 pixels/s. With similar motivation, Kompauer et al. invented a novel atmospheric pressure MALDI-IMS with lateral resolution of 1.4 µm. Using the developed system, they

demonstrated that high resolution can be obtained from brain and kidney sections as well as subcellular components within the model system, *Parmecium caudatum*.[127] Also, Feenstra et al. was able to achieve 5 µm resolution in their MALDI-IMS setup through spatial filtering, beam expansion, and decreased final focal length, allowing reduction in laser spot size from ~9 µm to ~4 µm.[128]

1.5.2 Mass Cytometry

More recently, the technique of mass cytometry has increasingly been used when studying cancer and the immune system.[129-131] Mass cytometry was developed to overcome the spectral overlap limitations found in flow cytometry. Unlike the aforementioned label-free imaging techniques, mass cytometry uses antibodies attached to non-radioactive rare earth metal isotopes that bind to a protein of interest. After the cells are tagged with up to 45 different antibodies, the cells are individually introduced into an inductively coupled plasma by nebulization. Only the heavy ions pass through the quadrupole before undergoing separation by TOF. Finally, the number and identity of the rare earth metal are recorded for each individual cell.

Lombard-Banek et al. combined capillary electrophoresis, electrospray ionization, and high-resolution mass spectrometry (CE-µESI-HRMS) to study frog *Xenopus laevis*.[132] From the study, they identified a total of 1709 protein groups and identified protein groups important for embryonic development. Recent efforts in mass cytometry research have focused on implementing the instrument into clinical settings for patient diagnosis since the severity of surgical trauma is often related to immune response. Gaudillière et al. demonstrated the ability of mass cytometry to survey immune cells in a clinical setting and correlated immune signatures with recovery time, pain, and functional impairment.[133] By using a series of whole-blood samples, three signaling responses in CD14$^+$ monocyte subsets were found to correlate with surgical trauma. The use of mass cytometry in clinical applications is still a young field, with new methodologies under development.

1.6 Microfluidics

In addition to the three major technical areas discussed above, recently, microfluidics has been used to understand underlying cell biology at the single cell level due to its high resolution and sensitivity, high throughput, low cost, and ease of miniaturization and automation. One promising advantage of microfluidics in single cell research is the ability to do single cell manipulation and detection by employing different

types of forces in the microchannels. Here, several common microfluidic techniques are introduced for single cell analysis. In many cases, these microfluidic platforms can be combined with one of the earlier discussed detection techniques.

1.6.1 Single Cell Manipulation

The four major forces applied to manipulate cells within microfluidic devices include magnetic, optical, mechanical, and dielectrophoretic forces. In the magnetic manipulation mode, target cells are labeled with antibodies coupled to nano/micro-magnetic beads and isolated through the interaction with magnetic fields inside microfluidic devices. The relatively small sizes of magnetic beads induce little detrimental effect on cellular function and viability. Because of the high specificity and efficiency, magnetic manipulation is quite suitable for rare cell type separation, especially in obtaining circulating tumor cells (CTCs). Using antibody-coated magnetic microbeads to label biological samples, several groups demonstrated the highly efficient isolation of CTCs in microfluidic channels with different magnetic structures (Error! Reference source not found.**A**).[134-136] Following capture, cancer cells can be further analyzed using other detection methods. In some instances, the native magnetic properties of cells are employed to act as the driving force for separation. Wu et al. designed a new microfluidic magnetophoretic separator to isolate paramagnetic deoxygenated red blood cells from malaria-infected blood samples, greatly improving the separation efficiency compared to the previous method.[137] One interesting application of magnetic manipulation is that the magnetic properties of cells can be chemically changed. For instance, live cardiomyocytes were transferred from diamagnetic to paramagnetic through myoglobin oxidation with sodium nitrite treatment and can then be isolated using a magnetic microfluidic system.[138]

Optical manipulation, also known as optical tweezers, the subject of 2018 Nobel Prize in Physics, is gaining more attention due to its ability to provide contact-less and contamination-free manipulation. Specifically, optical manipulation utilizes the focused laser beam to generate an electric field gradient that contains both scattering and gradient forces. Scattering forces act as a repulsive force and push cells away from the source of light, whereas gradient forces act as an attractive force and pull cells to the focal point. The balance between these two forces lies in the refractive index of cells in comparison to their surrounding fluid. The laminar nature of flow in microfluidic allows for targeted cells to be easily focused by the laser beam, generating overall better cell population recovery rate and purity of isolates (**Error! Reference source not found.B**). Liberale et al. reported

that the integration of micro-optical tweezers inside the microfluidic devices not only allows stable single-cell trapping, but also enables mechanical, chemical, and spectroscopic analyses.[139] However, the major drawback of microfluidic optical manipulation is the low throughput in comparison to conventional throughput generated from optical-assisted cell sorting systems. To solve the issue, Chen et al. introduced a 3D microfluidic device that is able to sort and provide high throughput of 23,000 cells per second at 90% purity.[140] This enrichment is accomplished through the use of a laser-induced cavitation mechanism within a microchannel to produce high-speed liquid jets to deflect cells focused by the sheath flow.

The introduction of specific microstructures into the microfluidic systems will impact the fluid dynamics that help the collection of single cells. These microstructures can be fabricated directly inside the microfluidic channels to separate cells, such as microfilters, microwells, dam structures, and microgrippers. An early study by Di Carlo et al. utilized a device consisting of U-shaped arrays to trap only single cells (**Error! Reference source not found.C**).[141] They used the device to study rates of cell death and division following cell trapping and found that more than 85% of the trapped cells still grow and adhere to the trapped site after 24 hours. Lin et al. presented a microfluidic sieve-like trap array to position single cells onto the designed micropatterns.[142] Various paired micropattern configurations also allow for placement of different cell populations next to each other. In another study by Wang et al, an array of bypass structure was designed to trap cells without the need for further surface modification.[143] With a high single cell trapping efficiency (~90%) achieved, cell apoptotic analysis and anticancer drug effects were examined.

Similar to optical manipulation, in dielectrophoretic cell positioning, individual cells are moved by the forces generated in a non-uniform electric field. Dependent on the properties of the surrounding medium and the polarity of the target cells, the electric field force is able to draw the cells to the field maximum or minimum. Cells moving in the direction of a strong electric field is called positive DEP, whereas cells moving toward the direction of a weak electric field is called negative DEP. Wang et al. employed a set of electrodes in the sidewall of the microchannels to generate negative DEP forces that repel cells from the sidewalls.[144] Furthermore, the generated negative DEP forces could be adjusted to position cells at different equilibrium points to direct them into different outlet channels. Moon et al. developed a continuous separation method which combined hydrodynamic fractionation and DEP separation to obtain CTCs from a spiked blood cell

sample.[145] DEP separation enhance the efficiency of cell isolation after initial hydrodynamic fractionation, and the blood cells were removed with the efficiency of more than 94%. In addition to isolating cells in the buffer solution, emulsified droplets are created inside the microchannels to encapsulate single cells for DEP separation, providing for safe and rapid single cells analysis to reveal gene mutation and enzyme reactions (Error! Reference source not found.**D**).[146]
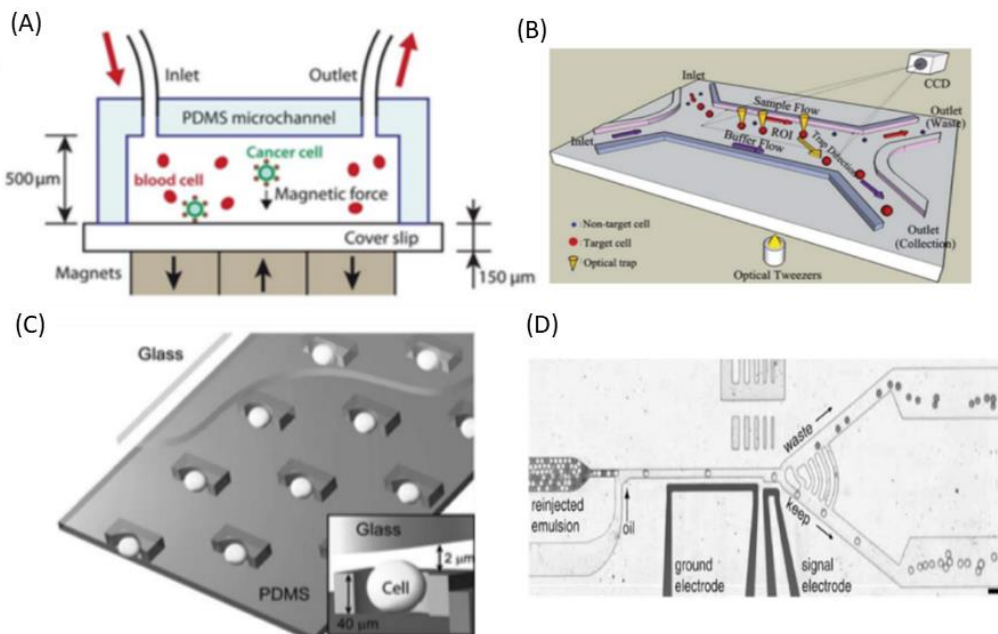
Figure 1.6. Microfluidic devices for single cell manipulation. (A) Magnetic single cell manipulation to capture magnetic microbead-labeled cancer cells in blood samples.[134] Reprinted with permission from Ref. 134. Copyright 2011 The Royal Society of Chemistry. (B) Optical tweezers to guide target cells into the desired channel by generating optical scattering and gradient forces.[147] Reprinted with permission from Ref. 147. Copyright 2011 The Royal Society of Chemistry. (C) U-shaped trap array developed in a microfluidic device to isolate cells through mechanical manipulation.[141] Reprinted with permission from Ref. 141. Copyright 2006 The Royal Society of Chemistry. (D) Dielectrophoretic separation of single cells combined with droplet encapsulation.[146] Reprinted with permission from Ref. 146. Copyright 2010 National Academy of Sciences.

Acoustophoresis, droplet microfluidics, and passive cell sorting are some other techniques available to manipulate single cells within microfluidic devices. Acoustophoresis, the movement of cells in response to an acoustic pressure wave, is a label-free cell handling technique with little detrimental effect and high spatial resolution. As an example, the application of acoustic waves in microfluidic cell sorting was performed by Ding et al., wherein tunable acoustic waves were able to precisely direct cells into different outlet channels in continuous flow.[148] Droplets in one phase surrounded by

another immiscible phase were generated in the microfluidic channels by co-flowing these two laminar fluids simultaneously. The main function of droplet microfluidics is for molecular analysis of single cell lysates allowing for independent biochemical reactors with ultra-small volume that reduce the dilution. Zinchenko et al. designed microfluidic devices to generate monodisperse droplets to study single *E. coli* cells during directed evolution.[149] Passive cell sorting is a category of cell manipulation methods that do not require labeling and only rely on cellular physical properties (e.g., size, shape, and density). One typical manifestation of passive fluid phenomena is Dean flow, which is caused by the inertial forces that emanate from boundary effects of fluid flow adjacent to the channel walls. Warkiana et al. exploited the Dean vortex flows to isolate CTCs from blood with high throughput and purity.[150] Other passive isolation methods, mainly focusing on deterministic lateral displacement and pinched flow, can be found in these specific reviews.[151-152]

1.6.2 Microfluidics for Single Cell Detection

Although microfluidics technology has the excellent ability to achieve single cell resolution by using different forms of force manipulation, they must still be paired with single cell detection methods and thus, the resultant output on cellular characteristics or behaviors is still dependent on the use of traditional detection tools. In fact, there are many examples demonstrating combinations of microfluidic systems with traditional detection approaches for single cell characterization. Here, we will feature a few microfluidic single cell detection examples that provide analysis in a rapid, sensitive, and high throughput fashion.

In biological systems, cells are activated by various environmental signals and, in many cases, respond by releasing a series of signaling molecules. The environmental factors initiating the cell activation range from cytokines, pathogens, and bacteria, to other cells and biophysical responses. Investigating cellular responses to these external factors is crucial to understand cellular behaviors in the context of biological interactions as well as the mechanisms behind relevant disease pathogenesis. The study of pooled populations with conventional assays may hide important heterogeneity of cellular response. Therefore, the high spatiotemporal resolution and the single cell capacity of microfluidics make it a suitable platform for exploring cell activation and secretion to provide quantitative information about natural cellular heterogeneity. Herein, two examples are introduced to reveal the significance of microfluidics technology in cell

activation and secretion studies. Zaretsky et al. developed a deep microwell platform that allows capture and growth of primary T lymphocytes.[153] Quantitative data about gene expression, cell activation, and proliferation can be obtained at the single cell level through 72 h live cell imaging (**Error! Reference source not found.A**).[153] Deng et al. used an integrated microfluidic system to isolate, purify, and profile CTCs from whole blood.[154] Using a poly-L-lysine barcode patter to efficiently capture the cells, it was clear that CTC cells exhibited highly heterogeneous secretion profiles for interleukin-8 (IL-8) and vascular endothelial growth factor (VEGF).

Cell migration has been recognized as another hallmark of immune response and disease pathogenesis.[155] Following the chemical gradients of signaling molecules, cells are able to migrate towards target sites and play an important role in defending against pathogen invasion or accelerating disease progression. For instance, neutrophils, the major type of white blood cells in the human immune system, migrate to infection sites once they receive inflammatory signals; on the other hand, cancer cells circulate in the blood to search new organs for tumor spreading. Compared to other traditional assays, microfluidic platforms facilitate the creation of stable chemical gradients with high spatiotemporal resolution and allows for quantitative tracking of single cell migration instead of characterizing the movement of cell population. Neutrophil directional migration, the critical immune response against inflammation, has been studied extensively using microfluidic platforms. Wu et al. established chemical gradients within a microfluidic device by mixing flow streams in a series of serpentine channels, and the laminar flow property of flow streams carrying different cytokine concentrations made a gradient available for neutrophil migration studies. They tracked the migration of individual neutrophils in the presence of competing gradients,[156] endothelial cell interaction,[157] and drug inhibitors,[158] which provide a detailed mechanistic analysis about neutrophil migratory behaviors. Nguyen et al. efficiently captured single metastatic cancer cells using an on-chip microstructure array while the migration of cancer cells into 3D matrixes were recorded with a change in impedance of patterned electrodes (**Error! Reference source not found.B**).[159]

Probing the effects of drugs on cellular behaviors is of great importance in drug discovery, which is a time-consuming, complicated, and costly endeavor. Hence, several groups have made great efforts to develop robust, rapid, and high-throughput approaches to address issues in the field pharmaceutical research. As a powerful bioanalytical platform, microfluidics offers numerous advantages over other biological assays, such as

sustaining highly parallel and multiplex detection, fast drug screening with small volume consumption, and automated dynamic data processing. Moreover, cell culture systems, even organ-like microenvironments have been created inside microfluidic devices to potentially replace traditional animal models for drug discovery. One typical application of microfluidic systems in drug-cell interaction studies is the evaluation of drug cytotoxicity. Sarkar et al. used a droplet microfluidics-based approach to study drug uptake and cytotoxicity in drug-sensitive and drug-resistant breast cancer cells.[160] The approach was used to encapsulate single cells for real-time imaging while heterogeneous drug effects were found for drug-sensitive cells and uniformly low uptake was shown in drug-resistant cells. Chen et al. performed drug-induced cell metabolism measurements using microfluidic chip electrospray ionization mass spectrometry (ESI-MS) (Error! Reference source not found.**C**).[161] Drug molecules were injected through the micro-chamber to incubate with microfluidic-cultured cells and the released metabolites were easily identified by ESI-MS without contamination from complex biological matrixes.
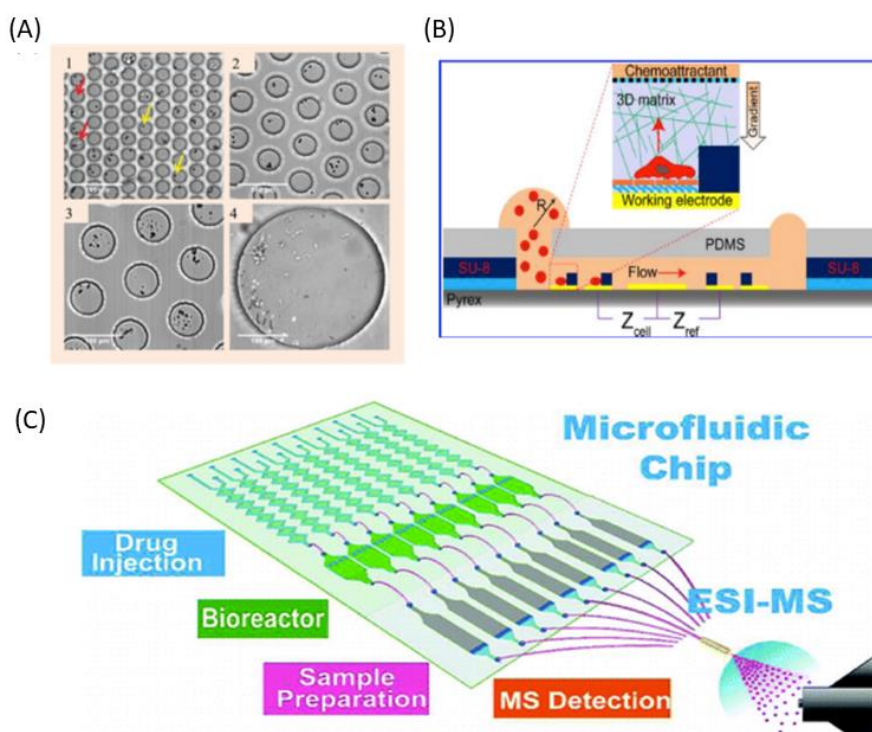
Figure 1.7. Microfluidic devices for single cell detection. (A) Single cell activation and secretion assays within the microfluidic microarray (panels 1-4 show different scale bars).[153] Reprinted with permission from Ref. 153. Copyright 2012 The Royal Society of Chemistry. (B) Cell migration studies in a 3D matrix based on the electric impedance signal change.[159] Reprinted with permission from Ref. 159. Copyright 2013 American Chemical Society. (C) Microfluidic device connected with mass spectrometry for examining pharmaceutical effects on cellular function.[161] Reprinted with permission from Ref. 161. Copyright 2012 American Chemical Society.

Perhaps the largest advance for microfluidic technology in single cell analysis is to assist single cell sequencing. Compared to traditional sequencing approaches, microfluidic platforms are able to provide unparalleled throughput in analysis by using highly integrated scalable devices. Currently, most single cell sequencing methods are based on the use of droplet microfluidics. Moon et al. demonstrated a droplet microfluidic platform for single cell RNA-sequencing with high throughput.[162] They were able to achieve high throughput by using a spiral microchannel, concentrated beads with a barcode were ordered by an inertial effect and were then co-encapsulated into droplets one-by-one in a droplet maker with diluted cells. This new strategy provides accurate high-throughput single cell analysis compared to the normal droplet sequencing device (which usually underestimates transcript numbers and overestimates cell numbers). In a study reported by Guo et al., a rapid, enzyme-free, single-cell microRNA assay was developed to differentiate cancer cells from non-cancer cells based on a continuous-flow droplet microfluidic process.[163] In the study, individual cells were encapsulated with the DNA amplifiers in water-in-oil droplets and then lysed to release microRNA. The released microRNA then interacted with DNA amplifiers in an isothermal cyclic cascade reaction to produce strong fluorescence signals. Multiple microRNAs within a single cell can be detected via the use of different DNA amplifiers to produce distinct fluorescence signals. Using this method, a throughput of 300-500 cells per minute was achieved. Furthermore, Hosokawa et al. used a droplet microfluidic platform to amplify single cell genomes with high accuracy and specificity.[164] From the study, thousands of single cells were compartmentalized in millions of picoliter droplets and subjected to lysis and multiple rounds of amplification This work allowed the whole genome amplification of both single bacterial cells and human cancer cells. An outstanding example without using droplet microfluidics for whole genome analysis was shown by Marie et al.[165] They fabricated an injection-molded, valveless microfluidic device to trap single cells by hydrodynamic force and then lysis the cells to extract genomes for sequencing using multiple displacement amplification. The results by analyzing colorectal cancer cell lines indicate a sub-nanoliter analysis volume and a ~90% genome coverage without contamination from non-human sources.

1.7 Perspective on Single Cell Analysis

Significant limitations to each technique class still exist, and the contributions scientists have made to overcome these technical barriers are discussed below as well as potential future developments.

1.7.1 Optical Techniques

Currently, there is no perfect super-resolution single cell imaging system available to address the intrinsic trade-off between acquisition speed and spatial resolution of fluorescence microscopy. Recently, scientists have focused on three technical areas to improve current methods. First, the modification of the optical detection system may improve the performance of super-resolution fluorescence microscopy. The development of scientific complementary metal-oxide-semiconductor transistor (CMOS) camera technology enables the acceleration of data acquisition, enlargement of the field of view, and the increase in effective quantum efficiency. Huang et al. further optimized CMOS technology by presenting algorithms to overcome the CMOS intrinsic noise and provide precise localization of single molecules while imaging in living cells at rates of up to 32 images per second.[166] Xu et.al. employed a dual-objective detection scheme to enhance the image resolution of STORM and to achieve <10-nm lateral resolution and <20-nm axial resolution.[167] From the study, they successfully imaged individual actin in BSC-1 cells.[167] Also, the combination of SIM illumination with light-sheet geometry prevents out-of-focus light and allows for three-dimensional, fast dynamic imaging of hundreds of volumes with resolution that beats the diffraction limit.[168] Second, newly engineered fluorescent probes, including small photocontrollable organic molecules and nanobody technology reduce labeling toxicity and promote high spatial resolution.[169-170] Lee et al. presented newly developed rhodamine spirolactam derivatives with switching wavelength in the visible region; these derivatives covalently attached to the cell surface for 3D super-resolution imaging.[169] Ries et al. developed GFP-tagging approaches with antibody-conjugated organic dyes for imaging in super-resolution microscopy.[170] This method can be applied to any protein by combining with libraries encoding GFP-tagged proteins. Lastly, state-of-the-art image processing methods can enhance signal-to-noise ratio as well as automatically quantify target molecules.[171-172] Zanella et al. minimized Poisson noise using a general scaled gradient projection method, outperforming the most efficient gradient projection method.[171] Levet et.al. implemented the freely available and open-source SR-

Tesseler software to develop a segmentation framework that allows precise and automatic detection of protein organization.[172]

Recently, efforts have been made to extend the single cell imaging techniques to the application of multicolor imaging, live cell imaging, and single molecule imaging, mostly based on the three technical areas discussed above. Lukinavicius et al. presented a far-red, cell permeable, carboxy-silicon-rhodaminefluorophore (SiR700) for multicolor live cell imaging. SiR700-based probes, together with carboxy-SiR650 probes, permit super-resolution fluorescence imaging of various single cell microstructures.[173] Fox-Roberts et al. demonstrated a mathematical simulation model to optimize the application of localization super-resolution microscopy in the field of live-cell imaging. Using this new method, they found that the activation density required to achieve the optimum imaging speed and the imaging speed that can be achieved, both vary by roughly an order of magnitude with each increase in the local dimensionality of the sample, which allows the optimized calculation of acquisition parameters in advance. Jin et al. reviewed the application of luminescent nanoparticles, such as carbon dots, quantum dots and polymer dots, in super-resolution imaging for single molecule tracking.[174] For example, He et al. reported the use of carbon dots for imaging the clustering and distribution of protein receptors in the plasma membrane.[175] The performance of carbon dots was compared to Cy3, Cy5, Alexa Fluor 647, and CdSe/ZnS quantum dots 605, and the carbon dot-based STORM super-resolution imaging exhibited a low duty cycle and high photon output per switch event with higher resistance to photobleaching than the comparators.

Interestingly, some powerful gene-editing strategies have been designed to achieve single-cell imaging without using traditional super-resolution microscopy platforms. Qin et al. demonstrated a confocal imaging platform which utilized the CRISPR-Cas9 based techniques to target and image low repeat genomic regions in live cells.[176] With this imaging platform, they were able to track multiple endogenous loci and monitor the position and dynamics of distinct chromatin regions. Morisaki et al. developed a technique called nascent chain tracking to image the messenger RNA translation process with single molecule resolution.[177]. The protein synthesis dynamics with mRNA translation kinetics were characterized in this work. Similar to super-resolution microscopy improvements, advances in improving detection systems of coherent Raman scattering spectroscopy have been made to enhance signal. Freudiger et al. developed a high speed and low noise fiber laser source for SRS imaging which overcomes the high-frequency noise problem and achieved.an imaging speed up to 1 frame s^{-1}.[178] Wei et al. reported a

technique to image nascent proteome synthesis quantitatively by using deuterium-labeled amino acids which has a specific carbon-deuterium bonds for quantitative SRS imaging.[179] The same group utilized alkyne tags as a general strategy in SRS imaging for studying small biomolecules such as DNA, RNA, phospholipids, and triglycerides in live cells and animals.[180]

There is still significant room to improve on single cell optical analyses, especially in the following areas: (1) most of the super-resolution techniques do not yield intrinsic chemical information; (2) thick samples, such as cells within tumor or tissue samples, are difficult to image, especially if the labeling density is high, and (3) because super-resolution images are generated via reconstruction (rather than direct imaging), avoiding imaging artifacts can be difficult. To address these weaknesses and others, there are several published examples where multiple optical techniques have been combined. For instance, the successful combination of super-resolution microscopy with TEM,[181-182] AFM,[183-185] and fluorescence, and the combination of confocal-PALM,[186] confocal-STORM[187-188] and SIM-STORM[189] have offset some of the weaknesses of each technique and provide new insights into biological phenomena.

1.7.2 Electrochemical Methods

Recent FSCV experiments have focused on improving the technique by overcoming limitations including balancing the amount of data collected with the high time resolution, eliminating interference from electroactive molecules that obscure the molecules of interest, and calibration of electrodes for *in vivo* experiments.[50, 190-192]

A high scan rate is often needed to capture most real-time cell-cell communication, which requires large amounts of data storage, slowing wireless data transfer, and increasing energy consumption, causing decreased device lifetime. The balance between data storage and the scan rates needed for meaningful biological measurements has been considered by several groups with several different collection rates being analyzed for sensitivity and electrode stability.[190-191] Findings suggest that higher scan rates increased sensitivity and change measured release and uptake time; however, the faster scan rates were not needed in cell lines with slower kinetics. Electrode stability was unaffected over the studied 8-hour period between a 10 and 1 Hz scan rate. Collectively, the data suggest that scan rate should be determined by the actual timescale of cell line performance to obtain the most valuable data. In addition to changing collection rate, the waveform (a pattern that defines what potential will be held on the electrode at each time point relative

to the reference electrode) can be modified to enhance FSCV detection of the molecules of interest. Recently, Schmidt et al. created a modified sawhorse waveform to quantify small tyrosine-containing peptides, which typically oxidize at higher potentials than catecholamines, to better understand the role of opioid peptides.[192] The waveform voltage increased from -0.02 V to 0.6 V at 100 V/s, increased from 0.6-1.2 V at 400 V/s and remained stable for 3 ms, then decreased at 100 V/s. In the traditional waveform, the oxidation of catecholamines masks the detection of peptides; however, in the modified waveform, the initial slow increase in voltage within the catecholamine's oxidation potential range helps decrease the current produced due to catecholamine oxidation and causes the oxidation of dopamine to occur at 400 mV, minimizing interference. Fouling is also decreased by holding the potential constant for 3 ms.

Homemade electrodes used for FSCV have high performance variability, requiring calibration for quantification of the molecule of interest. Since post-experiment calibration is often difficult or impossible, Roberts et al. developed a method to calibrate the electrode using the background charging current.[50] The approach was validated by comparison to traditional post-experiment calibration methods and the method can be done at any point during the experiment, making it ideal for longer experiments where electrode sensitivity may decrease or increase over the span of hours or days.

CFMA measurements are often constrained to *in vitro* studies due to several limitations. For instance, CFMA alone cannot be used to identify the oxidized or reduced molecule. Initial experiments on uncharacterized cell lines utilize cyclic voltammetry to determine the molecules being secreted before conducting amperometry experiments. However, this method does not allow for stoichiometric quantification if two or more secreted molecules oxidize at the potential being measured nor does it allow accurate measurement of real-time secretion events. Modification of the electrode surface to be selective for the molecule of interest or lowering the potential so only one type of molecule can be oxidized can mitigate this problem. Also, the difficult trade-off between an electrode's propensity for adsorption (required for sensitive detection) and fouling is the major hurdle when considering long-term implantation for single cell measurements within more complex tissues or organisms. Future work designing new electrode materials or formats that address this trade-off may make it possible for broader application of single cell electrochemistry.

The implementation of semiconductor nanowires or nanotubes in FETs allows for coalescence of cells with higher spatial resolution and achieves intracellular electrical

recording in addition to extracellular measurements.[193] In general, nanoelectrode-based detection may provide higher sensitivity compared to microelectrodes due to faster analyte diffusion as well as better spatial resolution for fine cellular compartment access. Several successful examples of secreted species detection have demonstrated the use of nanoelectrodes made with various materials and geometries for single cell analysis.[42-43, 194-195] A further technical advance is the incorporation of micro- or nano-electrode array formats into the chip system for cell-derived electrochemical signal detection.[196-198] Using the chip-based multi-electrode assays, single cell behaviors can be probed in a high-throughput fashion, and information about cell network dynamics is gleaned by electronically stimulating multiple cells at the same time.

One of the largest problems with patch clamp is the scale-up of single cell measurements *in vivo* on a large scale, particularly in the brain to study the effects of drugs and disease on brain signaling because of the human hours needed for electrode placement. Training personnel to operate the patch clamp can also be time consuming. As an initial approach to this limitation, Kodandaramaiah et al. developed an automated whole cell patch clamp system.[199] In 3-7 minutes, the robot is able to fully patch clamp neurons with a success rate of 32.9%, which is higher than the success rate for trained personnel (28.8%). The resulting data was found to have a similar quality relative to manual patch clamp.

Recently, electrochemiluminescence (ECL) imaging has been recognized as a powerful electrochemistry tool to study single cell function. ECL is a form of luminescence where light is emitted from an excited state species formed following electron transfer. Compared to photoluminescence-based methods, ECL has distinct advantages such as: (1) simple excitation source, (2) low interference and background for biological applications, and (3) better control of electrical and optical signal acquisition process with high spatial and temporal resolution. Liu et al. performed ECL imaging of single cells using TiO_2 modified conductive glass covered by a permeable chitosan film. .[200] Using this platform, the chitosan decreases the steric hindrance of cell attachment to increase the signal while the TiO_2 NPs improve visual ECL signal in luminol solution. Using this strategy, they analyzed the H_2O_2 released from cells at the single-cell level. Valenti et al. reported for the first time that the ECL can be used to image single cells and their membrane by functionalizing inkjet-printed CNT electrodes with selected antibodies targeted to overexpressed receptors on tumor cells. with low background signals. A novel ECL single-cell analysis platform introduced by Qiu et al. used carbon dot nanocomposites

containing Zn to evaluate CD44 expression levels in breast cancer cells.[201] This new probe recognized the cell membrane receptor through the specific interaction and exhibited a good analytical performance with detection linear range at the single-cell level. Based on the unique advantages and potential for further technical improvement, ECL imaging has the potential to be an important strategy for single cell analysis in the future.

As with optical techniques, there are several examples where the coupling of electrochemical and other analytical methods is done to overcome some limitations of single-cell analysis using electrochemistry alone. For example, Liu et al. synthesized a dual probe, fluorescent false neurotransmitter 102 (FFN102), and loaded it into cell granules to study the exocytosis behaviors within vesicles.[202] Upon stimulation of target cells, FFN102 diffuses out of the acidic microenvironment to the neutral extracellular space,which results in simultaneous electrochemical and fluorescence signal changes on the ITO surface. The coupled electrochemical/optical probe provides a good platform for cell exocytosis studies. for Huang et al. used photocleavable hairpin probes as functional units to detect mRNA optically and electrochemically in single cancer cells.[203] The final example here is a combined MS and patch clamp platform. Zhu et al. used this combined technique to analyze nanoliter samples of mouse neuronal cytoplasm for more than 50 metabolites in a high-throughput fashion without the loss of cell viability. The coupling of patch clamp with MS measurement may provide a powerful single-cell technology in future neuroscience research.

1.7.3 Mass Spectrometry

To alleviate molecular fragmentation effects in mass spectrometry detection, a number of primary ion sources, including electrospray droplet impact, cluster ion beams, and high-brightness C_{60} clusters, have been implemented to increase SIMS sensitivity.[204-206] Recently, gas cluster ion beams (GCIBs) consisting of thousands of particles in clusters have gained attention for bioimaging and molecular depth profiling applications.[207] Sheng et al. employed SIMS to visualize proteins and lipids involved in single HeLa cell growth and division.[208] They did this by using a small cluster projectile Bi_3^+ to acquire images and an Ar_{3500}^+ gas cluster ion beam to obtain depth profiles of cells. Extra efforts have focused on customized techniques, such as hybrid dual ion source, miniaturized single-probe sampling tip, and high throughput optical localization, to improve the performance of current mass spectrometric methods for single cell studies.[86-87, 209]

NanoSIMS is a nanoscopic scale version of SIMS that works based on a unique coaxial optical design of the ion beam, a normal incidence primary ion beam, and on an original magnetic sector mass spectrometer with multicollection. Compared to conventional dynamic SIMS, NanoSIMS allows simultaneously high lateral resolution, high mass resolution, and high sensitivity. The NanoSIMS is capable of various modes of operation including generation of chemical maps, depth profiles, mass spectra, isotopic ratios, and line scans. He et al. leveraged NanoSIMS imaging with ^{15}N-labeled cholesterol and sphingomyelin-binding proteins to visualize both cholesterol and sphingomyelin distribution in the plasma membrane of Chinese hamster ovary cells.[210] From the study, the images reveal that sphingomyelin preferentially binds to microvilli on the plasma membrane where the labeled cholesterol accumulates. Berthelot et al. combined NanoSIMS, carbon and nitrogen isotope labeling, and flow cytometry to study metabolic activity in photosynthetic pico-eukaryotes and cyanobacteria.[211] They found that there are differences in photosynthetic growth rates (based on C fixation), N acquisition, and N uptake for these picoplankton groups.

The new 3D OrbiSIMS instrument integrates SIMS with an Orbitrap to achieve high spatial resolution and high massresolving power. When the surface sensitivity and high mass/spatial resolution are combined with a depth profiling sputtering beam, the instrument becomes an extremely powerful tool for 3D chemical analysis.[212] Passarelli et al. used 3D OrbiSIMS to image the distribution of neurotransmitters such as gamma-aminobutyric acid, dopamine and serotonin in mouse hippocampus.[213] From the measurements, they were able to map the neurotransmitters within the hippocampus, generating important foundational data for further brain studies.

Sweedler and coworkers combined optical microscopy with MALDI-MS to achieve optically-guided MALDI-MS for single cell analysis.[214] et al. They used the combined approach to study the connections between dorsal root ganglia (DRG) chemical heterogeneity and cellular function.[214] They demonstrated that DRG cells can be divided into three distinct cell type based on the mass spectra results, a granularity that had not been obvious in previous liquid chromatography-MS analysis. Comi et al. utilized optically guided MALDI-MS and capillary electrophoresis electrospray ionization (CE-ESI)-MS to profile individual pancreatic islet α and β cells.[215] They did this by using MALDI-MS to identify individual pancreatic islet α and β cells and CE-ESI-MS to obtain quantitative information on metabolites and amino acids. Zenobi's group combined fluidic force microscopy with MALDI-MS to achieve nondestructive and quantitative withdrawal of

intracellular fluid from HeLa cells prior to MALDI-MS analysis.[216] They did this by inserting a microfluidic probe with negative pressure into the target cell to extract sampled material and transfer the sampled material onto the MALDI plate for analysis. Furthermore, they also proposed a high-density microarray for mass spectrometry (MAMS) sample preparation method prior to MALDI analysis.[216] MAMS enables high throughput and automatic sample aliquoting to give homogenous crystallization of the matrix-analyte mixture and facilitates a reproducible detection signal. Steinhoff et al. used this strategy to monitor metabolites and proteins from cell lysates without prior purification.[217] Despite these improvements in the resolution limit, many of the recent advances in MALDI single cell analysis involve the use of cell separation before performing MALDI-MS. To address this issue, Xie et al. combined microfluidic chip with MALDI to achieve automatic and high throughput detection of phospholipids in individual A549 lung cancer cells.[218] The setup flows cells into the device where they attach in individual wells. The matrix is injected into the device, encasing the cells for MALDI. In a different approach, Phelps et al. utilized microextraction to remove individual organelles from adipocytes differentiated from 3T3 L1 murine fibroblasts and placed them on a glass coverslide before being put into the MALDI.[219] This eliminated the need for extraction from multiple cells for each sample, reduced purification, and eliminated digestion compared to previous organelle extraction protocols.

Most mass cytometry methods require the sample to be in suspension before injection, therefore losing all spatial resolution. To increase spatial resolution, Giesen et al. combined high resolution laser ablation with mass cytometry.[220] In this method, the tissue of interest is extracted and fixed before staining with the metal-labeled antibodies. Using a UV laser, the sample is ablated and sent into the mass cytometer. The images are processed, giving single cell spatial resolution.

In addition, some non-traditional approaches, such as nanostructure initiated mass spectrometry (NIMS) based on a functionalized surface and scanning near-field optical microscopy-mass spectrometry (SNOM-MS) using laser focusing techniques, have been able to achieve high-resolution image acquisition.[221-222] These methods may be extended to single cell analysis in the future. Recent examples regarding the exciting application of 3D mass spectrometry imaging for single cell analysis are able to reveal the molecular distribution inside single cells with other new dimensions, providing enhanced spatial information compared to the 2D imaging.[223-224]

As with optical and electrochemical single cell analyses, there are many examples where MS is combined with other techniques to add new capability. For example, Hua et al. combined a vacuum compatible microfluidic module with SIM and ToF-SIMS to study single alveolar type II epithelial mouse louse lung C10 cells.et al.[225] In the study, SIM was able to image different components of a cell, whereas ToF-SIMS was able to describe intracellular molecule distribution. SIM and ToF-SIMS provide different spatial scales, allowing for both structural and molecular dynamics insight. Although, SIMS does not provide information on the roughness of the cell or tissue surface or differentiate between patchy and continuous signals. To enhance image quality, Tarolli et al. paired SIMs data with scanning electron microscopy.[226] By using a pan-sharpening algorithm, their results provide both topographical information and chemical information. This approach was used to understand how the environment impacts the adhesion of *B. braunii* algal cells, known for their role in biofuels. The data collected helped clearly define cellular boundaries in the biological matrix. Neupert et al. combined perforated patch clamp recordings, dye loading, and MALDI-MS to study neurotransmitters in neurons of intact brain samples.[227] In the study, they first utilized perforated patch-clamp to record Na^+ driven action potentials in uniglomerular projection neurons (uPN) upon depolarizing current injections. Then, they used dye loading to visualize the cell morphology and track the movement of different compartments. The collecting pipette was used to replace the recording pipette for cell soma separation. Finally, they used MALDI-TOF MS to profile the neuropeptide This strategy incorporates unambiguous mass spectrometric analysis and long-lasting current/voltage clamp recording and thus, will be an important tool for single neuron analysis.

One significant technical hurdle in mass spectrometric analysis of single cells lies in the challenge of data science and bioinformatics. Especially with untargeted analyses or hyphenated methods. The amount of data generated in a single experiment is significant, and methods to analyze massive correlated data sets are non-trivial. The insight gained from single cell mass spectrometric studies will be significantly enhanced as new data analysis methods become available.

1.7.4 Microfluidics

As discussed above, microfluidics technology is more likely to be used as an efficient tool for sample preparation with the follow-on analysis conducted by coupling to more traditional detection platforms. Currently, the research community has made great

efforts to integrate the interface between microfluidic platform and conventional analytical methods (optical, electrochemistry, and mass spectrometry methods), which greatly enhances the application of microfluidics in the field of single cell analysis. On-chip electrophoresis is a good example where the combination of microfluidic sample preparation and conventional detection strategy is very effective. Li et al. applied voltage onto different reservoirs a glass microchip to induce electrophoretic separation of various intracellular metabolites, hydrogen peroxide, glutathione, and cysteine, with different fluorescence labels were characterized through multicolor fluorescence detection.[228] In this work, microchip electrophoresis and fluorescence detection were combined to study single-cell metabolomics and intracellular oxidative/antioxidative molecular mechanism. The same strategy was employed to perform simultaneous detection of fluorescent derivatives of four metal ions (Na^+, K^+, Ca^{2+}, and Mg^{2+}) in PC-12 cells.[229] Results indicate the importance of the four metal ions in regulating neurological diseases at the single cell level. It is not difficult to integrate electrodes into microfluidic channels through deposition or printing processes ahead of biological application. Altinagac et al. fabricated a device with a titanium interdigitated electrode layer coated on the glass substrate for single cell DEP manipulation and impedance analysis.[230] Using this device, the signature difference between each cell type in electrochemical responses can be recorded. Lou et al. designed a microfluidic chip integrated with Au microelectrodes to detect CCRF-CEM cells.[231] By using an immobilized aptamer as the sensing element and Pt NPs as catalyst, the electrochemical oxidation of hydrazine was detected with high sensitivity, down to ten cells. In a study reported by Xie et al.al., a microwell-array-based microfluidic chip was combined with MALDI-MS to study single cell phospholipids with high-throughput analysis.[218] Another mass spectrometry-associated example provided by Yang et al. used microchambers to trap single cells followed by microvalve-controlled protein digestion/labeling/matrix delivery process.[232] They employed this approach to quantitatively assess the number of Bcl-2 molecules expressed on the single cell level. Although there have been successfully attempts to incorporate different detection methods into microfluidics technology, more efforts are still needed for future use. Usually, the adaption of detection platform to the microfluidic closed-channel structure or the specific geometry required can be complicated to avoid hampering the single-cell manipulation via microfluidics. Too often, the microfluidic design ends up being complex, which makes it expensive and time-consuming to fabricate. Lastly, there are many sensitive biosensing methods which can be combined with microfluidics for single cell

analysis, such as super-resolution microscopy, surface-enhance Raman spectroscopy, surface plasmon resonance, and electrochemical microscopy.

In addition to performing single-cell genomics studies, microfluidics has been increasingly utilized as a tool for single-cell functional proteomics. Compared to genomics studies, the investigation of single-cell proteomics faces the challenges of a small amount of protein and the enormous complexity of the proteome. Microfluidic platforms can precisely control the cellular microenvironment with low sample consumption and target cell loss, thus enhancing the sensitivity, specificity, and the automation of the assay. Also, high throughput analysis can be achieved through using special device design (microchambers and microdroplets) and combining with promising detection strategies. For instance, Yang et al. described a novel single-cell beads-on-barcode microarray chip to profile multiple protein markers in rare circulating tumor cells.[233] This assay detects proteins by assigning two independent markers: bead size and fluorescence color. This work allows multiplexed protein detection with high sensitivity for important rare cells at the single-cell level. In another study, a droplet-based microfluidic chip was developed by Debs et al. to measure proteins secreted by single cells.[234] A single cell is encapsulated in droplets together with fluorescent probes and a functionalized bead. The bead captures secreted proteins and fluorescent probes bind to captured proteins resulting in an optical signal for detection. From the perspective of single-cell proteomics study, the major technical bottleneck is the low multiplexing capacity of current single-cell proteomic methods. Usually, the microchip-based methods can achieve simultaneous detection of tens of protein markers, which is a very small part of the whole proteome. The development of new labeling approaches and antibody engineering techniques may increase multiplexing capacity for single cell proteomics. Also, some new mathematical approaches are required to extract the key information from experimental data to clarify the expression states of different proteins from single cells.

One of the major obstacles for the real application of microfluidics in single cell analysis is the disconnect between lab-scale development and commercialization. Most of the reported microfluidic devices are produced by the laboratory manufacturing methods, and the performance of these devices are not stable enough to give reproducible results due to the sophisticated instrument operation that supports the microfluidic chip and/or the complicated micro- or nano-structures contained within devices. Those who use microfluidic chips are usually required to undergo significant training before doing experiments. The potential broad application of microfluidics in the biomedical community

would require commercial investment for manufacturability standardization so that laboratory methods can be converted to robust industrial products. We can already see progress in this area as industrial production techniques such as injection molding, hot embossing, 3D printing, and screen-printing are being leveraged within the laboratory microfluidics fabrication process.

1.8 Conclusions

Single cell analysis is critical to understand heterogeneity in biological systems and the role of that heterogeneity in both function and dysfunction of these systems. In addition, single cell analyses often give otherwise unavailable insight into the actual timescale of biological processes. In this chapter, descriptions of selected technologies give an overall picture of the development of single cell analysis in recent years while focusing on applications in subcellular quantification, cellular dynamics tracking, single-cell disease diagnostics, and pharmacological research. There is a growing interest in the field of single cell analysis due to the need for deeper understanding of molecular-level cellular processes and the emergence of relevant state-of-the-art instrumentation and methodology. Continued developments in this area will require close communication between synthetic chemists, analytical chemists, chemical biologists, engineers, and data scientists. In later chapters, the use of CFMA will be used to understand the roles of platelets and mast cells in the context of malaria and antimalarial drugs. Thus, this serves as an example of single cell analysis techniques as tools for understanding how cells work to impact disease and cellular function.

Chapter 2

Insight into the Effects of *Plasmodium chabaudi* on Platelets Using Carbon-Fiber Microelectrode Amperometry
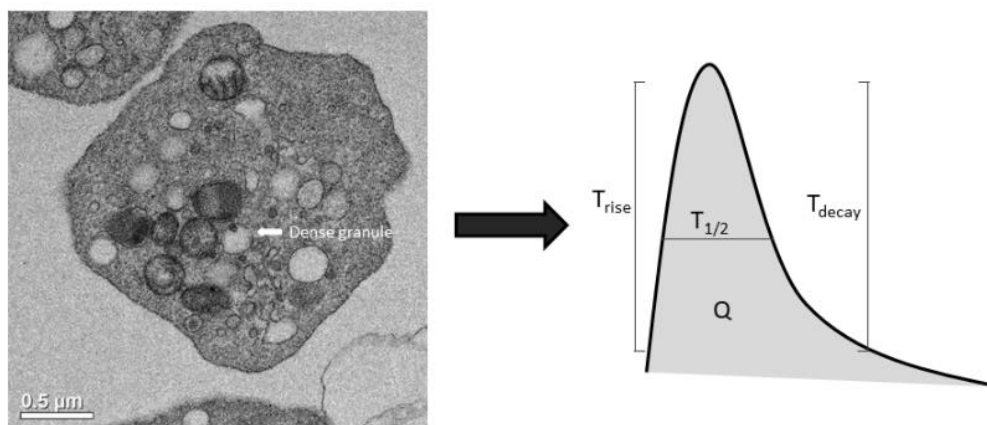
Reprinted from: Xiong-Hang, K.; Kemnetz-Ness, K.; Krieger, A.C.; Haynes C.L. Insight into the Effects of *Plasmodium chabaudi* on Platelets Using Carbon-Fiber Microelectrode Amperometry. *ACS Infect. Dis.* 2019, 5,4, 592-597. Copyright 2019, with permission from American Chemical Society.

2.1 Overview

This chapter makes use of a single cell technique, carbon-fiber microelectrode amperometry (CFMA) to understand how the fundamental function of platelets is affected during malarial infection. Platelets are anuclear circulating cell bodies within the bloodstream commonly known for their roles in clot formation during vascular injury to prevent blood loss. They also have significant impact in a range of diseases, including malaria. However, the role of platelets in malaria is controversial, with contradicting evidence suggesting that they either assist in destruction of malarial parasites or facilitate a severe form of malaria. Precedent work suggests that the timing of infection is critical in determining whether platelets switch roles from being protective to deleterious. As such, the work within this chapter makes use of the unique mechanistic perspective offered by CFMA to understand how platelet secretion is impacted in malarial infection stages (ascending parasite count versus descending parasite count). Malarial platelet behavior was compared to platelets from non-infected control mice by probing their exocytotic function. Results suggest that mouse-malaria caused by the parasite *Plasmodium chabaudi,* during both ascending and descending infection stages, reduces platelet exocytotic events and delays platelet granule fusion. In addition, platelets are more impacted by the disease early in the infection stages. In all, understanding platelet behavior in the malarial context may present new therapeutic routes to treat or cure malaria.

2.2 Introduction

Malaria is a debilitating infectious disease with infection occurring through the transmission of the Plasmodium parasites from an infected source.[1] Malaria is most common in children under the age of five and in equatorial and west Africa as well as parts of southern Africa.[2] Of the hundreds of known species in the Plasmodium genus, five are known to affect humans, through which a generic understanding of the Plasmodium parasite life cycle has been established.[3-4] Although it is clear that the parasites undergo cycles of invasion, multiplication, and further infection, the role of the immune system components during the cycle is not clear. Much research effort related to malaria has been geared toward disease elimination through drug discovery with a focus on direct parasite destruction; however, a major problem with drug usage and development is the building of drug resistance in parasites over time.[5-6] Therefore, an effort to reveal immune and inflammatory responses in the context of malaria is important to better understand the

fundamental biological interactions between cells and the parasites as well as suggest parallel treatment mechanisms that engage the immune system directly.

Platelets are anuclear cells generated by megakaryocytes, which originate from pluripotent hematopoietic stem cells within the bone marrow.[7] Platelets are the second most numerous circulating cell, numbering ~200,000/μL blood in humans, making them first responders to injury and infection.[7] Previous work on platelets and malaria has yielded contradictory results, with some studies suggesting that platelets serve in a protective role[8-13] and others suggesting that platelets play an aggressive role during infection.[14] The protective role of platelets has been demonstrated via platelet binding to infected red blood cells (iRBCs) and subsequent release of immunomodulatory molecules such as platelet factor 4, resulting in the eradication of parasites.[8-13] However, chronic inflammatory response from platelets has been demonstrated to lead to tissue destruction and breaching of the blood−brain barrier, as in cerebral malaria.[14] Cumulatively, these studies suggest that there may be a time or physiological trigger during which platelets switch from being protective to deleterious in the context of malaria and that the secretion of platelet chemical messengers is particularly important in immune response. However, additional studies suggest that platelets are unable to directly eliminate or evoke a protective immune response to malarial parasites.[15] The work done to date involving platelets and malaria, including the aforementioned studies, are focused at the bulk cell level, which can obscure any heterogeneity within the cell population as well as biophysical details about the chemical messenger secretion process. Therefore, this work uses single cell measurement techniques to provide a complementary approach to understand the fundamental role of platelets during the different malarial infection stages.

Carbon-fiber microelectrode amperometry (CFMA) is an electrochemical analytical tool for the real-time, label-free detection of secreted molecular species from single cells based on the high spatial resolution, high sensitivity, and low background current of the carbon microfiber working electrode.[16] The ability of the CFMA method to provide very fast time resolution (submillisecond) allows for real-time measurement of exocytosis events in platelets. Previous studies using this method have demonstrated that averaging of electrochemical measurements from single platelets corresponds well to measurements made from bulk platelet studies.[17-18] The setup involves placing a working electrode (the carbon-fiber microelectrode) in contact with a single platelet with the electrode held at a fixed potential (**Figure 2.1A**). Upon stimulation of the cell with stimulant, the cell releases chemical messengers via exocytosis, and the chemical messengers are oxidized at the

surface of the working electrode (**Figure 2.1B**). Each exocytosis event (i.e., release of chemical messengers from an individual granule) is then recorded as a spike on a trace of current vs time (**Figure 2.1C**). Analysis of each individual spike yields both quantitative and qualitative information regarding platelet exocytosis (**Figure 2.1D**). By comparing CFMA measurements from platelets collected from both healthy and malaria-infected mice, it is possible to characterize the impact of malaria on exocytotic machinery and stored chemical messengers, considering both earlier and later malarial stages. Though platelet granules contain a variety of chemical messengers, choice of the potential during CFMA measurements determines which chemical messengers are oxidized and thus quantified. Herein, the electrode potential was set such that it was sufficient to detect serotonin (5-hydroxytryptamine, 5-HT) released from the platelet-dense granules with no interference from other granule contents. While 5-HT has not been directly implicated in the malarial immune response, here easy-to-measure 5-HT was used as a proxy for all other platelet chemical messengers that are co-localized and co-released with 5-HT. Thus, it is hypothesized that if malarial parasites activate platelets (directly or indirectly), then malaria-exposed platelets will exhibit different exocytosis parameters compared to the malaria-free control.
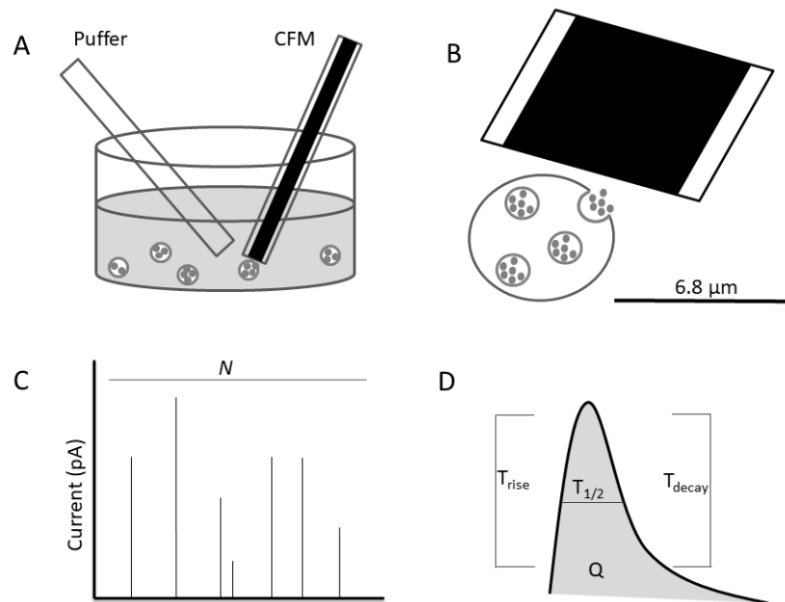
Figure 2.1. Schematic of CFMA setup and trace analysis. (A) CFMA setup with puffer loaded with stimulant and CFM as working electrode (Ag/AgCl reference electrode not shown). (B) Schematic depiction of an exocytosis event from a single platelet detected at the surface of the working electrode. (C) Schematic amperometric trace (current vs time), resulting from exocytosis events with each spike representing a single granular release event and N being the total number of exocytosis events observed per cell measurement. (D) Schematic of magnified individual current

spike showing T_{rise} (the time from 10 to 90% of the spike height in the rising phase), $T_{1/2}$ (time for full width at half-maximum), Q (integration of the spike area to reveal the amount of 5-HT secretion as charge), and T_{decay} (time from 90 to 10% of height in the decay phase).

The highly structured granules stored within platelets are exocytosed to facilitate chemical messenger secretion following activation.[19] Activation can be triggered by a variety of extracellular stimulants; in most cases, extracellular platelet activation leads to increased intracellular calcium ion concentration, triggering organization of the actin structure and movement of granules into close proximity of the plasma membrane. The subsequent interaction between members of the soluble N-ethyl maleimide sensitive factor and attachment protein receptors (SNARE) on the granule and plasma membranes (i.e., granule-plasma membrane fusion) facilitates release of granular contents to the extracellular environment (**Figure 2.2**). To gain information on how platelet exocytotic machinery is affected in malarial vs control conditions, mice were infected with mouse blood containing *P. chabaudi* to achieve two different parasitemia stages (ascending and descending) vs. uninfected mice. CFMA was used to probe the function of platelet exocytotic machinery and revealed that *P. chabaudi* reduced platelet secretion of 5-HT as well as delayed granule fusion during both ascending and descending parasitemia stages. Additionally, the severity of the infection on platelet is more prominent in the earlier infection stage compared with the later infection stage, as seen with platelets that appear visually more activated with significant delay not only in fusion pore opening to facilitate chemical messenger release, but also in pore closing. Thus, this suggests that malarial parasites do have biological interactions (directly or indirectly) with platelets and that this interaction impacts platelet function.
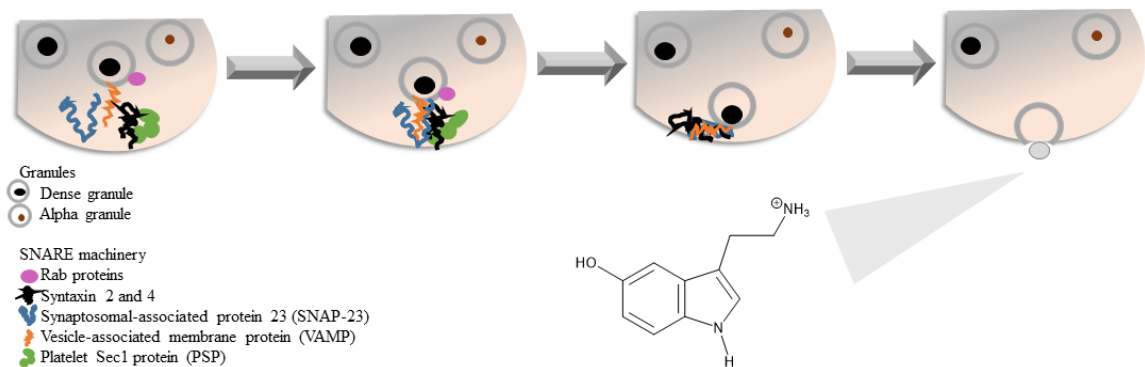

Figure 2.2. Platelet exocytosis process. Platelet exocytosis is driven by both lipid and protein interactions following stimulation. Serotonin molecules stored within platelet dense granules are

released during exocytosis, along with other granular contents. Serotonin can be detected as a proxy for the entire granular content.

2.3 Materials and Methods

2.3.1 Materials

10 X Phosphate buffered saline (PBS) was diluted to 1X and pH to 7.2-7.4. Giesma stain was diluted to 10% using 1X PBS. Acid citrate dextrose solution (ACD) was prepared by combining 41.64 mM citric acid ($C_4H_8O_7$), 76.16 mM sodium citrate ($Na_3C_6H_5O_7$), 11.10 mM dextrose ($C_6H_{14}O7$), and deionized water and pH to 5.1. Tyrode's buffer was prepared by combining 117 mM sodium chloride (NaCl), 2.62 mM potassium chloride (KCl),0.52 mM magnesium chloride hexahydrate ($MgCl·6H_2O$), 5.55 mM D-glucose ($C_4H_{12}O_6$), 5 mM 4-(2-hydroxyethyl)-1-piperazineethanesulfonic acid (HEPES), 12.14 mM sodium bicarbonate ($NaHCO_3$), and deionized water and pH to 7.2-7.4. Electrolyte solution was prepared using 3.0 M potassium acetate ($C_2H_3KO_2$) and 30.0 mM potassium chloride (KCl). Thrombin was stock prepared to 500 U/mL using Tyrode's buffer and diluted to 5 U/mL per experiment. pH adjustment was done using sodium hydroxide and hydrochloric acid. White's saline, a prepared 10% solution of 1:1 mixture of (1) 2.4 mM sodium chloride (NaCl), 0.1 mM potassium chloride (KCl), 46 mM magnesium sulfate ($MgSO_4$), and 64 mM calcium nitrate ($Ca(NO_3)_2*H_2O$) and (2) 0.13 M sodium bicarbonate ($NaHCO_3$), 8.4 mM monosodium phosphate (NaH_2PO_4), and 0.1 g/L of phenol red, pH 7.4. Glutaraldehyde ($C_5H_8O_2$) was prepared to 0.1% and 3% and osmic acid was prepared to 1% using White's saline. Ethanol were prepared to 30, 50, 70, 80, 95, and 100% with deionized water. Methanol, uranyl acetate ($C_4H_8O_6U$) and lead citrate ($C_{24}H_{20}O_{28}Pb_3$) were used as received. All materials were purchased from Sigma-Aldrich and used as received or prepared into specific solution. Deionized water (18.2 MΩ·cm) was purified using a Milli-Q Millipore water purification system (Billerica, MA).

Male C57BL/6J mice was purchased from Jackson Laboratories through Research Animal Resources (UMN, Twin Cities). *Plasmodium chabaudi* AS MRa-741 was purchased from BEI Resources (Manassas, VA).

2.3.2 *In Vivo Plasmodium chabaudi* Infection and Growth Tracking

The University of Minnesota Institutional Animal Care and Use Committee (IACUC) approved all protocols and procedures according to protocol #1702-34571A. Male

C57BL/6J mice purchased at 5−6 weeks were injected with *Plasmodium chabaudi* AS MRA-741 through an IP route. Further infections were completed by taking blood from an infected mouse and injecting 10^5 to 10^6 iRBCs into the peritoneal cavity of a naive mouse vs 1X PBS control. Beginning 5 days post-infection, thin blood smears were collected daily, fixed with methanol, and stained with 10% giesma stain to monitor parasite growth according to a previously established protocol.[20] At least 20 platelets were measured per mouse to get a combined total of 158 platelets from control (6 mice), 74 platelets from ascending parasitemia stage (3 mice), and 64 platelets from ascending parasitemia stage (3 mice). Each mouse infected in ascending and descending is independent from one another.

2.3.3 Platelet Collection

Whole blood from control and malaria-infected mice was collected in 200 µL of ACD, separated at 130xg for 10 min to obtain the platelet-rich plasma (PRP) layer, and platelets were obtained following centrifugation at 520xg for 10 min. Separated platelets were resuspended in Tyrode's buffer, and experiments were conducted on the same day as collection. Different mice were used for ascending and descending stages to allow for sufficient sample purification and studies.

2.3.4 Microelectrode Fabrication

Carbon-fiber microelectrodes were fabricated in the laboratory as described in previous literature.[21] Prior to use, electrodes were polished to 45° on a diamond polishing wheel (Sutter Instruments) and stored in isopropyl alcohol until use. The electrodes were backfilled with electrolyte solution prior to being mounted on a platinum-coated silver wire (Squires Electronics) situated on the potentiostat's headstage.

2.3.5 CFMA Measurements

The headstage with the mounted electrode was connected to an Axon Instruments Axopatch 200B Potentiostat (Molecular Devices Inc.) to control the applied voltage vs a silver/silver chloride (Ag/AgCl) reference electrode (BASi). A pulled glass capillary micropipet, loaded with 5 U/mL of thrombin and connected to a Picospritzer III (Parker Hannifin) for control, delivered the stimulating solution to the cells. Both the headstage of the mounted electrodes and the micopipet were mounted on Burleigh PCS-5000 piezoelectric micromanipulators (Olympus America Inc.) to achieve optimal placement

relative to the individual platelets. The potential of the carbon-fiber microelectrode was set at +700 mV vs the Ag/AgCl reference electrode following placement of the carbon microelectrode in solution. The electrode was positioned over a single platelet using piezoelectric micromanipulators with the stimulating pipet a few micrometers away. Upon the start of a measurement, the stimulating micropipet delivered a 3 s dose of the stimulant, inducing platelet degranulation. Data were acquired for 90 s following stimulation with a collection rate of 20 kHz. Oxidation of serotonin from each dense granule appeared as discrete current spikes and were detected as a function of time.

2.3.6 CFMA Data Analysis and Statistics

Collected amperometric traces were processed using Tar Heel CV software (courtesy of Dr. Michael Heien), processed at 200 Hz with a Bessel low-pass filter, and analyzed using Minianalysis software (Synaptosoft, Inc.) with signal-to-noise ratio set at 2. From measurements, each spike reveals an individual granular release event from an individual platelet, and each spike was analyzed for several parameters, including (Q) and full-width half-maximum ($T_{1/2}$). Upon analyzing all spikes from an individual cell trace, including summation of the number of secretion events per platelet (N), and performing statistical analysis from all the cells in each condition, outlier analysis was performed. If a cell trace included an outlier in one or more parameter, the cell characteristics were removed from the data set. Outliers in each parameter were classified as having a value greater than two standard deviations from the average of the log-transformed data set. Following outlier removal, 95% confidence intervals were calculated for each parameter, and significant differences among treatment groups were determined using a one-way ANOVA at a 95% confidence level. Data sets from the two control groups were combined as no significant differences were observed for the control conditions among a majority of the mentioned parameters by a one-way ANOVA test.

2.3.7 Transmission Electron Microscopy Preparation

Purified platelets were prepared according to a previously established protocol.[22] Platelets were fixed by incubating pelleted platelets in 0.1% glutaraldehyde at 37 °C for 15 min, 3% glutaraldehyde at 4 °C for 30 min, followed by in 1% osmic acid (w/v) at 4 °C for 1 h. All fixation solutions were prepared in White's saline. Following fixation, platelets were pelleted at 800g, 5 min, washed with White's saline, dehydrated in a graded series of ethanol (30, 50, 70, 80, 95, and 100%, respectively), and embedded in resin. Thin

sections were cut to ~70 nm in thickness on a LEICA EM UC6 ultramicrotome and were examined after staining with uranyl acetate and lead citrate to enhance contrast on carbon-stabilized grids on a Tecnai 12 electron microscope at an accelerating voltage of 120 keV.

2.3.8 TEM Data Analysis and Statistics

Images of platelets obtained from TEM were visually analyzed based on their appearance and categorized as non-activated, slightly activated, or totally activated. Non-activated platelets are discoid in shape with intact intracellular granules, slightly activated platelets have started to lose the discoid shape and display short filopodial extension from the cell body due to rearrangement of the internal actin cytoskeleton, and totally activated platelets no longer retain the discoid shape and display full filopodial extension (**Figure 2.3**).
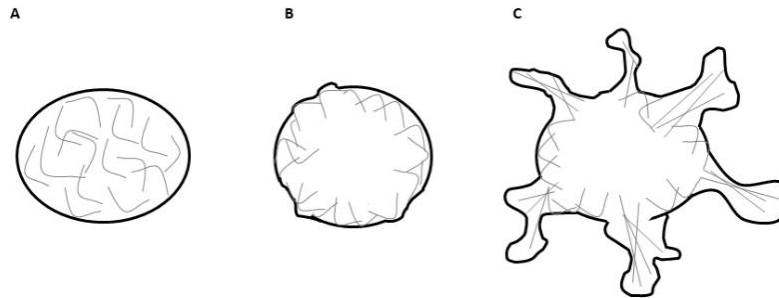
Figure 2.3. Classification of platelets based on shapes. (A) non-activated platelet with discoid shape, (B) partially activated platelet with slight filopodial extension, and (C) fully activated platelet with full filopodial extension due to re-arrangement of the cytoskeleton.

2.4 Results and Discussion
2.4.1 *Plasmodium chabaudi* Infection

Mice injected with blood infected with malarial parasites were monitored daily by thin blood smears stained with giesma (**Figure 2.4**) to either ascending or descending parasitemia stages (**Figure 2.5**). Parasites were apparent in red blood cells at ~5-7 days post-infection, peaked at ~12 days, and declined afterward, similar to precedent literature.[20]
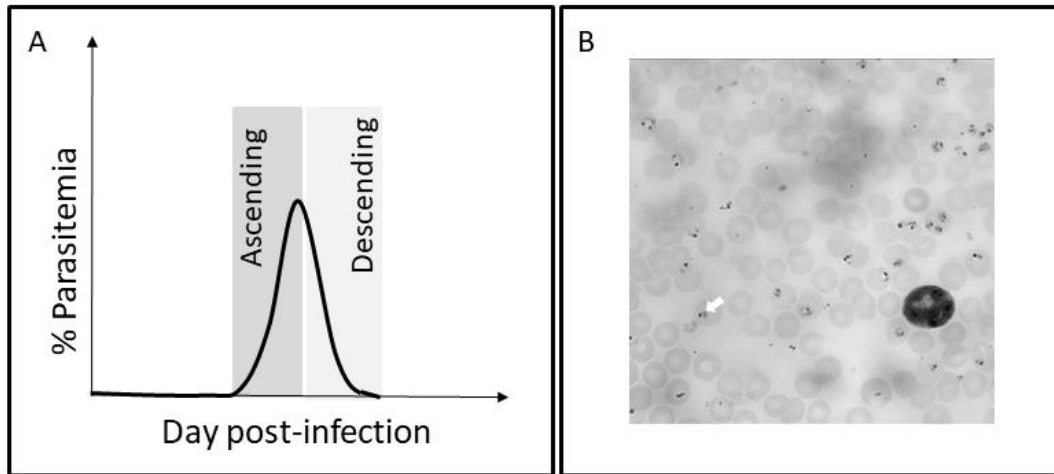
Figure 2.4. Daily tracking of *P. chabaudi* in RBC day post-infection. (A) Parasites were tracked to either ascending or descending parasitemia stages through (B) bright-field microscopy visualization of 10% giesma-stained thin blood smears using a 100X oil immersion lens. Arrows on the bright field image indicate one of several parasites growing within an iRBC.

	Parasitemia stage	
	Ascending	Descending
Replicate 1	13.5%, day 11	7.6%, day 17
Replicate 2	20.5%, day 11	0.0%, day 20
Replicate 3	31.0%, day 9	2.0%, day 17
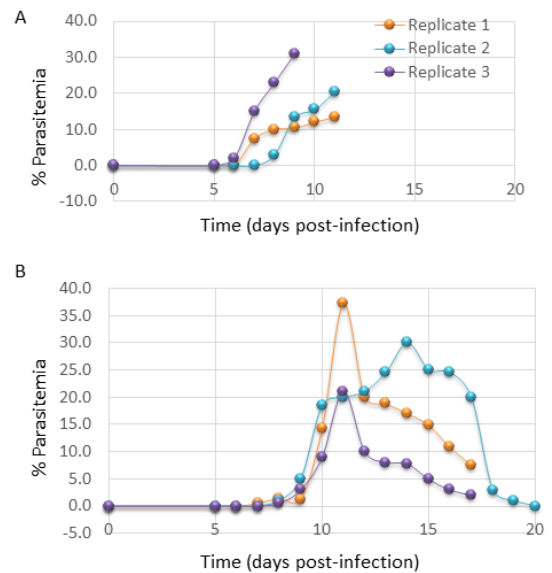
Figure 2.5. Tracking of parasitemia changes daily. (A) mice used for ascending parasitemia and (B) mice used for descending parasitemia. All mice were sacrificed for platelets studies at parasitemia percentage and day as indicated on table.

2.4.2 CFMA for Single Platelet Measurements

The ability of CFMA to provide sub-millisecond time resolution facilitates acquisition of detailed information about the biophysical mechanism of thrombin-induced platelet degranulation during various infection stages. Thrombin was chosen to enable

comparison to the extensive literature on platelet secretion studies. A 3 s delivery of 5 U/mL thrombin was used to stimulate platelet degranulation within the different experimental groups, and CFMA was used to oxidize and detect 5-HT released from individual dense granules from individual platelets. In addition to 5-HT, dense granules contain calcium ions, magnesium ions, pyrophosphate, ATP, and ADP, which are released along with 5-HT.[23] While, to the best of our knowledge, 5-HT is not directly related to malaria, monitoring 5-HT provides information on platelet exocytosis as malaria infection progresses. Platelet degranulation was characterized by closely analyzing each single platelet trace for five parameters: spike area (Q), number of spikes per cell (N), spike full-width at half-maximum ($T_{1/2}$), spike rise time (T_{rise}), and spike decay time (T_{decay}). Both Q and N provide quantitative information about 5-HT storage and secretion, whereas $T_{1/2}$, T_{rise}, and T_{decay} collectively provide insight on the kinetics of the exocytotic machinery.

Detailed analysis of Q, the integrated area under each current spike, provides information regarding total charge measured per granule as the 5-HT is oxidized. Because oxidation of 5-HT is a 2-electron process, Faraday's law can be used to convert the charge information to the number of 5-HT molecules detected per granule, which can then be multiplied by N to obtain the total number of 5-HT molecules detected per platelet. N, taken as the total number of exocytotic events or spikes observed per platelet measurement, is also a measurement of the exocytosis efficiency as it involves overall granule transport, docking, and fusion mechanisms. To account for full platelet response, all platelet conditions need to be multiplied by 2, since the electrode only covers ~50% of the platelet surface (the top half). However, since all conditions were treated similarly, multiplying by 2 to account for full response is not necessary in our case. Results reveal that platelets from ascending and descending parasitemia stages released 48.7% and 43.9% fewer 5-HT molecules per platelet, respectively, compared to the malaria-free control condition (**Figure 2.6A**). While both malaria infection conditions are statistically distinguishable from the malaria-free control, they are not statistically distinguishable from one another. Individual analysis of Q and N reveal that the decrease in 5-HT molecules released per cell during ascending parasitemia is primarily due to fewer exocytotic events (N), whereas during descending parasitemia, fewer molecules were released per exocytosis event (Q) (**Figure 2.6B,C**).

Information regarding pore fusion, opening, and closing during platelet exocytosis is obtained by analyzing T_{rise}, $T_{1/2}$, and T_{decay}, respectively. T_{rise} is the time from 10 to 90% of each spike rise and gives information regarding the fast secretion of 5-HT unassociated

with intragranular polyphosphate matrix immediately following fusion pore formation. $T_{1/2}$ is the time at full-width half-maximum and gives information on the rate at which the inorganic polyphosphate matrix expands to secrete granular-bound 5-HT.[24] T_{decay} is the time from 90 to 10% of the spike maximum decaying phase and gives information about the rate of fusion pore reclosing as chemical messenger secretion slows and then stops. Results reveal that fusion pore formation (T_{rise}) in ascending and descending parasitemia is significantly delayed 35.0 and 36.3%, respectively (**Figure 2.6E**) compared to the malaria-free control. However, only pore opening ($T_{1/2}$) in ascending parasitemia is delayed significantly, 26.8% slower vs control and 19.8% slower vs the descending stage (**Figure 2.6D**). Furthermore, pore closing (T_{decay}) is significantly delayed in the ascending stage vs the descending stage with an 18.3% increase in time (**Figure 2.6F**).
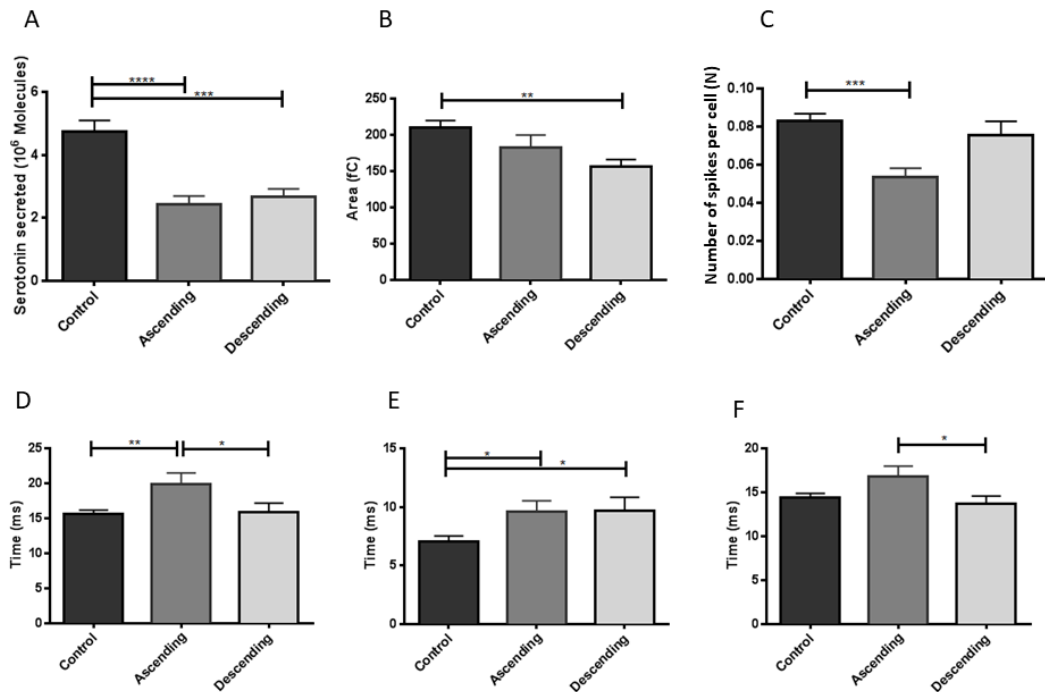
Figure 2.6. Effect of *P. chabaudi* on platelet function measured using CFMA. (A) Total serotonin released/oxidized following consideration of (B) area under each current spike and (C) number of granule secretion events per platelet. Kinetic analysis of current spikes to yield information regarding (D) $T_{1/2}$, (E) T_{rise}, and (F) T_{decay} to give information regarding machinery involved in pore opening, dilation, and closing. Results shown in plots are the mean ± SEM. Number of platelets: control (n = 158), ascending (n = 74), and descending (n = 64). *P ≤ 0.05, **P ≤ 0.01, ***P ≤ 0.001, and ****P ≤ 0.0001.

Earlier attempts with data analysis has looked at correlating specific parasitemia percentage with the CFMA data; however, there was no correlation between similar

parasitemia percentage and the CFMA data. Therefore, two stages of infection were selected for the study. Overall, kinetic results suggest that exocytotic machinery involved in pore fusion is affected during both infection stages; however, the earlier ascending infection stage is not the same as later infection stages. Furthermore, exocytosis foot features have been shown to reveal important controlling factors of the fusion pore in cholesterol-treated platelets; therefore, a full analysis of prespike or postspike feet, foot events as well as nontraditional events was completed with no statistical differences in the frequency of prespike and postspike, suggesting that the determining factor in pore fusion is not due to initial pore formation, dilation, or closure during *P. chabaudi* infection (**Figure 2.7**). It is possible that differences in innate and adaptive immune responses during various malarial stages contributed to differences in trends for $T_{1/2}$ and T_{decay} of descending vs ascending stages.[25-26] For instance, during early infection, it is likely that the innate immune response (inflammatory responses from inflammatory cytokines) is involved more than the adaptive immune responses (T-cells), which is important at later infection stages and may possibly explain the observable differences in platelet dynamics.
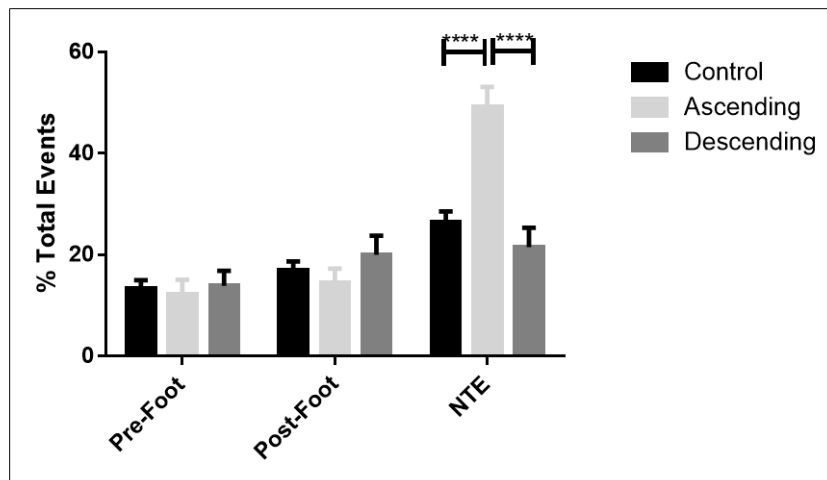
Figure 2.7. Frequency of pre-spike, post-spike, and non-traditional events (NTEs) in the three platelet conditions. Results are plotted as mean ± SEM, and the number of platelets analyzed: control (n = 158),

Because there are quantitative differences observed in malaria infection vs control conditions, transmission electron microscopy (TEM) was carried out following fixation of platelets to preserve their fine structures as well as any physical changes that may have

resulted from exposure to *P. chabaudi* compared to the control. These TEM images were compared to the CFMA-measured number of granular secretion events per platelet (N) to gain a possible explanation for the reduced degranulation observed in the malarial conditions compared to the control condition (**Figure 2.8A, B**).
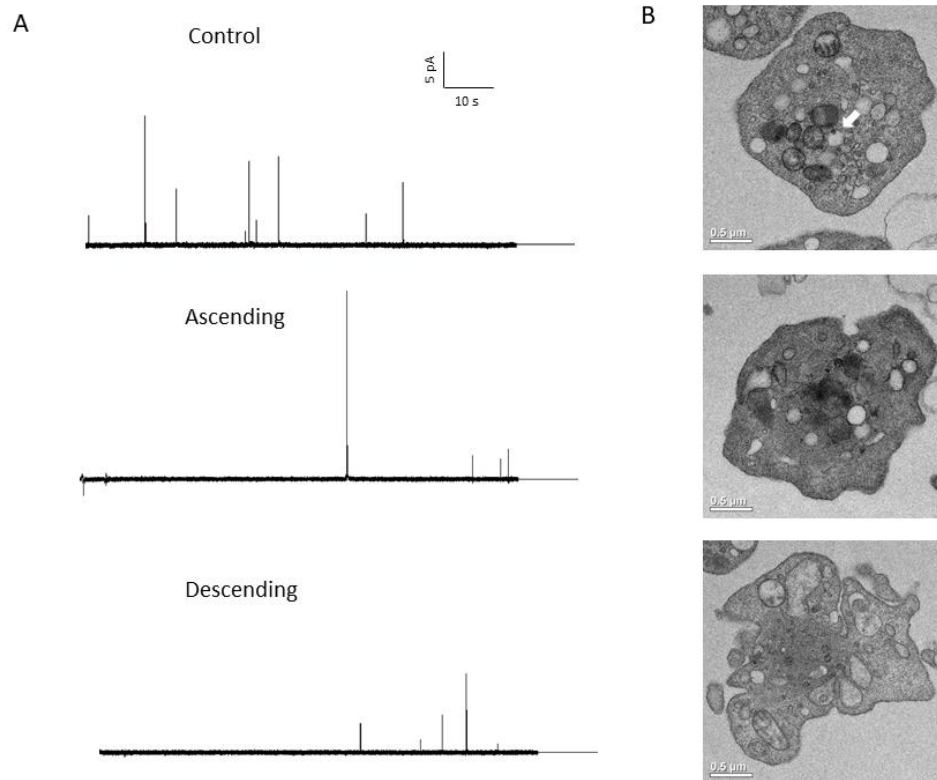
Figure 2.8. Visual correlation of CFMA on platelets and TEM. (A) CFMA traces from the various conditions, showing fewer exocytotic events in malarial conditions compared to malaria-free controls. (B) TEM images showing fixed platelets structures of nonactivated (discoid shape), slightly activated, and totally activated platelets (top to bottom). Representative dense granule indicated by a white arrow in the top TEM image. Scale bar shown is 0.5 µm. Number of platelets imaged: control (n = 27), ascending (n = 28), and descending (n = 16).

Comparison of TEM images from malarial and control conditions reveal that platelets experiencing malarial conditions contained fewer dense-core granules and appeared more activated and distorted overall (**Figure 2.3**). From visual inspection of platelets (n = 16−28) in TEM images, platelets from control mice consisted of 74% non-activated, 26% slightly activated, and 0% totally activated platelets; platelets from the ascending malaria condition consisted of 0% no-nactivated, 6% slightly activated, and 94% totally activated platelets, and platelets from the descending malaria condition consisted of 11% non-activated, 21% slightly activated, and 68% totally activated platelets (no statistical analysis

was performed because sampling within TEM is not appropriate for statistical analysis). Overall, platelets from both malarial conditions appeared more distorted, characteristic of activation, which may explain the decrease in secreted serotonin molecules during induced activation with thrombin.

2.5 Conclusions

The work in this chapter makes use of CFMA to explore how platelet secretion is impacted in malarial infection stages. CFMA analysis on platelets from blood infected with *P. chabaudi* (both ascending and descending stages) revealed that malaria infection reduced the total amount of serotonin molecules released per granule and delayed the machinery involved in platelet pore fusion. Additionally, platelets from ascending parasitemia are further delayed in pore opening ($T_{1/2}$) and in pore closing (T_{decay}) compared to the descending stage, demonstrating the ability of CFMA to reveal biophysical differences among the different parasitemia stages. Although the work herein focused on *P. chabaudi*, a noncerebral malaria inducing strain, the results could possibly be generalized to cerebral malaria-inducing strains such as *P. berghei*, which display a similar thrombocytopenia profile. Based on previous findings regarding *P. chabaudi* and *P. berghei* growth profiles, *P. chabaudi* parasitemia ascends, peaks, and declines, while *P. berghei* ascends and peaks with no apparent decline. However, their thrombocytopenia profile is reported to be similar (thrombocytopenia starting with appearance of parasitemia, reaching a low point, and starting to climb again without going back to pre-parasitemia level). Percent parasitemia and thrombocytopenia is likely part of the reason that there are conflicting conclusions about protective/pathologic effects of platelets in malaria.

Future work will aim to illuminate this complex relationship between percent parasitemia, thrombocytopenia, and platelet function. Furthermore, although the study herein is unable to address whether platelets directly or indirectly interact with *P. chabaudi* in mice, it reveals the ability of CFMA to provide both quantitative and qualitative information on the effect of malaria on platelets, strengthening the argument that the stages of parasitemia infection are an important consideration for future malaria and platelet studies and that 5-HT can be used as a proxy for other dense granule molecules and implications for immune response.

Chapter 3

Plasmodium chabaudi Affects Mast Cell Degranulation as Measured by Carbon-Fiber Microelectrode Amperometry
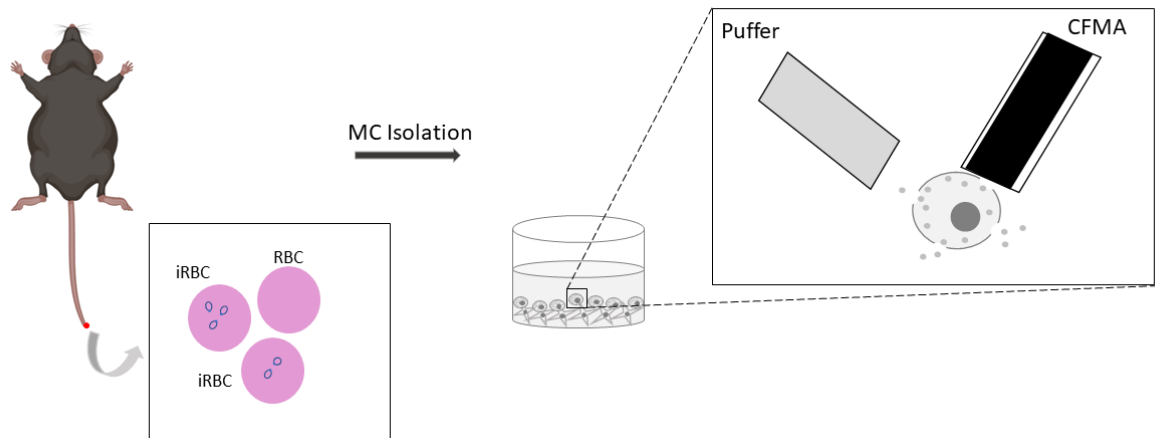
Adapted from: Xiong-Hang, K. and Haynes C.L. *Plasmodium chabaudi* Affects Mast Cell Degranulation as Measured by Carbon Fiber Microelectrode Amperometry. *In preparation.*

3.1 Overview

This chapter uses the single cell technique, carbon-fiber microelectrode amperometry (CFMA) discussed in Chapter 2 to investigate how the fundamental function of mast cells (MCs) are affected during malarial infection. MCs are effector cells of the immune system commonly known for their roles in asthma and allergy. They are present throughout the biological system in various tissues, serving as an interface between the biological system and environment. Previous work characterizing the impact of malaria on MCs revealed contradictory results, showing minimal to strong correlation between MC degranulation and disease progression. This work seeks to reveal how MC degranulation is impacted in the presence of malaria, induced by *Plasmodium chabaudi*, using a mouse model and a single cell measurement technique that reveals exquisite biophysical detail about any impacts to the degranulation process. It was hypothesized that the malarial parasites would impact MC degranulation response during live infection and that these differences would be revealed via CFMA. In fact, the data collected show that different stages of malarial infection affect MC degranulation differently, affirming the importance of different infection stages in future studies of malarial immune response. Furthermore, a comparison of MC degranulation response to that measured from platelets in similar circumstances show similar trends in quantitative degranulation, suggesting that MC and platelets are affected similarly despite their distinct biological roles. Overall, the work herein reveals important details about the role of MCs in malaria progression, relevant during treatment decisions, as well as a potentially generalizable impact on chemical messenger secretion from cells during malarial progression.

3.2 Introduction

Malaria is a bloodborne disease caused by malarial parasites transmitted through infected mosquitos. Symptoms of the disease depend largely on the infected parasite strain and range from mild to severe, including death; the most severe strains in human are *Plasmodium falciparum* and *Plasmodium vivax*.[1] Based on worldwide data from the World Health Organization (WHO), there were an estimated 228 million cases of malaria and an estimated 405,000 deaths, in 2018.[1] In these cases, the disease was predominantly observed in children under the age of five in developing countries, largely from the sub-Saharan Africa, with some reported cases in regions of South-East Asia, Eastern Mediterranean, Western Pacific, and the Americas.[1] The continuing impact of malaria worldwide has inspired ongoing malaria research aiming to mitigate the damage

caused by the disease. In the laboratory, animal models have been established as a foremost way to better understand human malaria.[2] Here, work involved the use of *Plasmodium chabaudi,* a non-complicated malaria strain, in a mouse model to study the effect of malaria on mast cell (MC) secretion. Non-complicated malaria would be expected to lead to low-level chronic immune system impact in a wild-type animal model,[3] and thus, it is relevant to consider the sentinel cells of the immune system.

MCs are present throughout the body and within tissues, making them a major interface between the body and the environment as part of the first line of defense against infection.[4] An overview of precedent work on MCs and malaria showed a range of results, from no correlation to significant correlation between MC degranulation and disease progression.[5] However, none of the precedent studies, to the best of our knowledge, used a real-time measurement approach to characterize how MC degranulation and secretion of chemical messengers are impacted during malaria. Therefore, the goal herein was to use a real-time measurement technique to investigate the effect of *P. chabaudi*-infected red blood cells on MC behavior. It was hypothesized that the malaria parasites cause MC degranulation as infection proceeds within the animal.

The MC degranulation response was measured using carbon-fiber microelectrode amperometry (CFMA), a single cell technique that has been shown to successfully measure secretion of electroactive species by MCs with rich quantitative and kinetic details.[6-9] CFMA works by using electrochemistry to detect the pre-packaged molecules, 5-hydroxytryptamine (5-HT, also known as serotonin), as they are release from MC dense granules.[10] In CFMA, a fixed potential of +700 mV vs. Ag/AgCl reference electrode is applied to the tip of a carbon fiber microelectrode to oxidize any secreted 5-HT from the individual MCs underneath the microelectrode, following a 3s stimulant exposure from a nearby pre-loaded pipette. Although there are no studies showing a specific biological link between 5-HT and malaria, as with platelets in Chapter 2, 5-HT was used as a measurable proxy to understand MC secretion of a variety of small molecule and protein messengers.[11]

Quantitative results from this study indicate that MCs from ascending and descending parasitemia conditions were impacted in distinct ways. All MC granule fusion pore actions (opening, duration, and closing) from the ascending parasitemia stage were faster than parasite-free controls, while only pore opening was affected in the descending parasitemia stage. Since 5-HT is not directly implicated in malaria, this work includes correlated measurements of platelet factor 4 (PF4), a 7.8 kDa, 70-amino acid protein present in abundance within the alpha granules of platelets.[12] These data aimed to

characterize similarities between secretion of 5-HT from dense granules and PF4 from alpha granules as well as reveal a biological connection between the MCs studied here and blood platelets during malarial infection. Since PF4 is a large protein and cannot be measured with the CFMA technique, a commercial PF4 ELISA kit was used for its quantitative detection. From the comparison, both MCs and platelets during descending parasitemia showed significantly more 5-HT or PF4 released compared to malaria parasite-free controls, indicating that both cells may be impacted in a similar way. Overall, this study affirms that the stage of malarial infection is an important consideration for future malaria studies and that CFMA can be used to obtain biologically relevant information on MC degranulation in the context of malaria.

3.3 Materials and Methods

3.3.1 Materials

10X Phosphate buffered saline (PBS) was diluted to 1X and pH to 7.2-7.4. Methanol and isopropanol were used as received. Giesma stain was diluted to 10% using 1X PBS. Acid citrate dextrose solution (ACD) was prepared by combining 41.64 mM citric acid ($C_4H_8O_7$), 76.16 mM sodium citrate ($Na_3C_6H_5O_7$), 11.10 mM dextrose ($C_6H_{14}O7$), and deionized water and pH to 5.1. Tyrode's buffer was prepared by combining 117 mM sodium chloride (NaCl), 2.62 mM potassium chloride (KCl), 0.52 mM magnesium chloride hexahydrate ($MgCl \cdot 6H_2O$), 5.55 mM D-glucose ($C_4H_{12}O_6$), 5 mM 4-(2-hydroxyethyl)-1-piperazineethanesulfonic acid (HEPES), 12.14 mM sodium bicarbonate ($NaHCO_3$), and deionized water and pH to 7.2-7.4. Tris buffer was prepared by combining 16.26 mM trishydroxymethalamine, 150 mM NaCl, 420 mM KCl, 5.60 mM glucose, 2 mM calcium chloride ($CaCl_2$), 3 mM $MgCl_2$*$6H_2O$, and deionized water and pH to 7.2 – 7.4. Dulbecco's Modified Eagle Media (DMEM) purchased from HyClone was formulated with 4.5 mM L-glutamine ($C_5H_9NO_4$) , 4.5 mg/mL L-glucose, 110 µg/mL sodium pyruvate (CH_3NaO_3) and supplemented with 10% bovine calf serum, 10 U/mL penicillin and 10 µg/mL streptomycin (Gibco, Carlsbad, CA). Calcium Ionophore A23187 was prepared to 20 µM with Tris buffer. Electrolyte solution was prepared using 3.0 M potassium acetate ($C_2H_3KO_2$) and 30.0 mM KCl. pH adjustment was done using sodium hydroxide (NaOH) and hydrochloric acid (HCl). All materials were purchased from Sigma-Aldrich unless specified. Deionized water (18.2 MΩ·cm) was purified using a Milli-Q Millipore water purification system (Billerica, MA).

The mouse PF4 ELISA kit was purchased from Millipore Sigma (Burlington, MA). The Pierce BCA Protein Assay kit was purchased from ThermoFisher Scientific (Waltham, MA). Male C57BL/6J mice was purchased from Jackson Laboratories. *Plasmodium chabaudi* AS MRa-741 was purchased from BEI Resources (Manassas, VA).

3.3.2 *Plasmodium chabaudi* Infection and Growth Tracking

Malaria infection and tracking in mice were approved by the University of Minnesota Institutional Animal Care and Use Committee (IACUC) according to protocol #2001-37768A. Male mice purchased at 5-6 weeks from Jackson Laboratories were injected with *Plasmodium chabaudi* AS MRA-741 via intraperitoneal (IP) route to obtain the live malaria strain. For mice used in experiments, infection of naive mice was accomplished using $10^5 - 10^6$ infected red blood cells (iRBCs) from an infected mouse vs. 1X PBS (control). Five days post-infection, parasite growth was tracked daily using thin blood smears collected from the tail vein of mice and stained with 10% giesma stain in 1X PBS according to established protocol.[13] Ascending parasitemia is defined as before any decline of parasitemia is seen while descending parasitemia is defined as the stage when the parasite count is in decline. Each mouse experiencing ascending and descending infection is independent from one another with tracking of parasites daily starting on day 5 post-infection (**Error! Reference source not found.**).

	Parasitemia stage	
	Ascending	**Descending**
Replicate 1	7.33%, day 9	2.0%, day 21
Replicate 2	48.73%, day 10	0.0%, day 21
Replicate 3	8.04%, day 9	5.10%, day 14
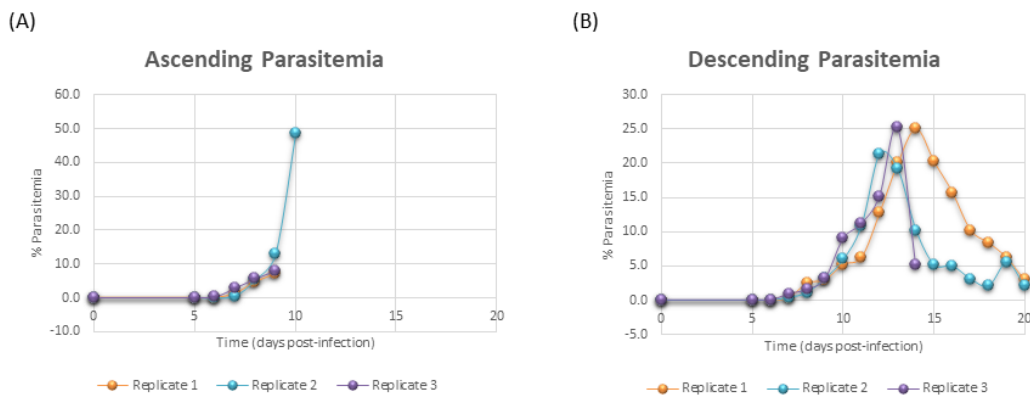
Figure 3.1. Daily tracking of *P. chabaudi* in RBC day post-infection. (A) mice used for ascending parasitemia data points and (B) mice used for descending parasitemia data points. All

mice were sacrificed for MC studies at specified parasitemia percentage and day as indicated on the table.

3.3.3 MCs Collection and Co-Culture with 3t3 Fibroblast Cells

Mice in ascending parasitemia, descending parasitemia, and malaria-free controls were euthanized according to IACUC protocol #2001-37768A. MCs were collected from the peritoneal cavity of the mouse with slight modifications to a previously established protocol.[6] Following whole blood collection for parallel platelet studies, 8 mL of cold prepared DMEM were injected into the peritoneal cavity of a mouse followed by 30 s massage to initiate release of MCs from the surrounding connective tissues. Then, the injected media was collected using a fine tip plastic transfer pipet. The collected media with cells was centrifuged to collect MCs as a pellet at 450xg for 10 min. Pelleted MCs were re-suspended in warm media and plated on top of prepared and confluent 3t3 fibroblast cells cultured based on previously established protocol in small petri-dishes.[6] MCs on 3t3 cells were incubated overnight in 5% CO_2 at 37°C in an incubator prior to CFMA measurements.

3.3.4 Carbon-Fiber Microelectrode Fabrication

Carbon-fiber microelectrodes were fabricated in the laboratory according to previous literature.[14] First, a single strand of carbon fiber was pulled using vacuum into a glass capillary tube. Second, the tube containing the carbon fiber was heated and pulled to obtain two electrodes. Third, the carbon fiber was cut to the tip of the glass under a light microscope using a scalpel. Then, cut electrodes were epoxied and cured overnight at room temperature.

Prior to use, electrodes were polished at 45° on a diamond polishing wheel (Sutter Instruments), backfilled with electrolyte solution, and stored in isopropyl alcohol to clean the polished tips prior to being mounted on a platinum-coated silver wire (Squires Electronics) situated on the potentiostat's headstage.

3.3.5 CFMA MC Measurements

On the day of measurements, MCs on 3t3 fibroblasts were washed three times with warm Tris buffer at pH 7.4 to remove cell media. Then, the plate was filled with 1-2 mL of warm Tris buffer for measurement.

The headstage with the mounted electrode was connected to an Axon Instruments Axopatch 200B Potentiostat (Molecular Devices Inc.) to control the applied voltage vs. a silver/silver chloride (Ag/AgCl) reference electrode (BASi). A pulled glass capillary micropipet, loaded with 20 µM calcium ionophore A23187 in Tris buffer and connected to a Picospritzer III (Parker Hannifin) for controlled delivery of the stimulating solution to individual cells visualized under the microscope. Both the headstage of the mounted electrodes and the micopipet were mounted on Burleigh PCS-5000 piezoelectric micromanipulators (Olympus America Inc.) to achieve optimal placement relative to the individual MCs. The potential of the carbon-fiber microelectrode was set at +700 mV vs. the Ag/AgCl reference electrode following placement of the carbon microelectrode in solution. The electrode was positioned over a single MCs using piezoelectric micromanipulators, with the stimulating pipet a few micrometers away. Upon the start of a measurement, the stimulating micropipet delivered a 3 s dose of the stimulant, inducing MC degranulation. Data were acquired for 90 s following stimulation with a collection rate of 20 kHz. Oxidation of 5-HT from each dense granule appeared as a discrete current spike and were detected as a function of time. Since the electrode covers only 10% of a mast cell surface area, the data obtained is assumed to represent 10% of the mast cell's total secretion. To minimize the effects of serotonin fouling of the electrode surface, the electrode was cycled in 0.1 M sodium hydroxide between measurements as previously described[15] and used for a maximum of six measurements. A combined total of 80 MCs from control (6 mice), 50 MCs from ascending parasitemia stage (3 mice), and 38 MCs from descending parasitemia stage (3 mice) were used for quantitative analysis.

3.3.6 CFMA Data Analysis and Statistics

Collected amperometric traces were processed using Tar Heel CV software (courtesy of Dr. Michael Heien), processed at 200 Hz with a Bessel low-pass filter, and analyzed using Minianalysis software (Synaptosoft, Inc.) with the signal-to-noise ratio set at 5. From measurements, each spike reveals an individual granular released event from an individual MC, and each spike was analyzed for several parameters, including charge (Q), number of spikes per cell, full-width-half-maximum ($T_{1/2}$), pore opening (T_{rise}), and pore closing (T_{decay}). Upon analyzing all spikes from an individual cell trace and performing statistical analysis from all the cells in each condition, outlier analysis was performed. If a cell trace included an outlier in one or more parameter, all cell characteristics were removed from the dataset. Outliers in each parameter were classified as having a value

greater than two standard deviations from the average of the log-transformed dataset. Following outlier removal, 95% confidence intervals were calculated for each parameter, and significant differences among treatment groups were determined using a one-way ANOVA test set at a 95% confidence level. From the outlier test, 17 MCs from control, 7 MCs from ascending parasitemia stage, and 6 MCs from descending parasitemia stage were removed. Datasets from the two control groups were combined as no significant differences were observed for the control conditions among most of the mentioned parameters by one-way ANOVA test. Histogram plots of all analyzed parameters were constructed to view the distribution of the parasitemia stages vs. control (**Figure 3.2** and **Figure 3.3**). Each data point within the quantitative and kinetic plots is representative of a MC measurement.
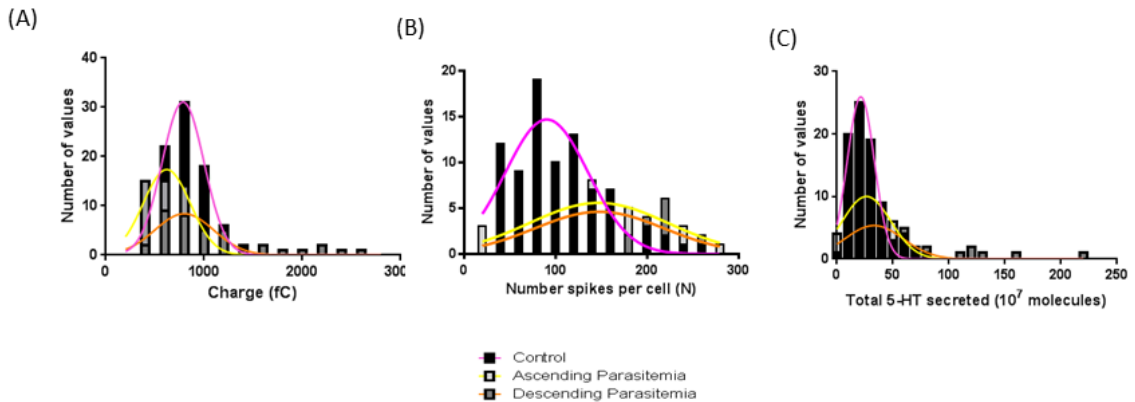
Figure 3.2. Histogram plots of quantal CFMA parameters. (A) Area under each current spike, (B) Number of secretion events per cell, and (C) total 5-HT secreted. Colors: control (pink), ascending parasitemia (yellow), and descending parasitemia (orange). These distributions show how individual cells contribute to the average parameters presented

76
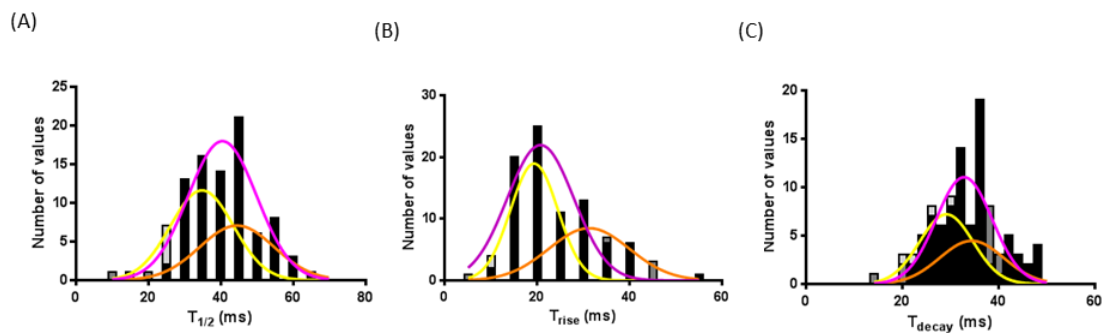
Figure 3.3. Histogram plots of kinetic CFMA parameters. (A) Time at full-width-half-maximum ($T_{1/2}$), T_{rise}, and T_{decay}. Colors: control (pink), ascending parasitemia (yellow), and descending parasitemia (orange). These distributions show how individual cells contribute to the average parameters presented.

3.3.7 Platelet Collection

Mice in ascending parasitemia, descending parasitemia, and malaria-free controls were euthanized according to IACUC protocol #2001-37768A. Whole blood collected via cardiac puncture was collected in 200 μL ACD. Purified platelets were obtained by separating whole blood at 130 xg for 10 min to obtain the platelet rich plasma (PRP) layer containing the extracellular PF4 fraction, followed by pelleting down platelets from the PRP layer. Pelleted platelets were then resuspended in 1 mL of Tyrode's buffer to obtain intracellular PF4 fractions. Platelets were stored at -20°C until ready for BCA and PF4 assays.

3.3.8 PF4 and BCA Measurements

PF4 was analyzed using the mouse PF4 ELISA kit. The kit comes with an antibody-coated 96-well plate that is specific for mouse PF4. PF4 from samples get immobilized within the well and biotinylated anti-mouse PF4 antibody is then added. HRP-conjugated streptavidin is added, followed by addition of a TMB substrate solution. A "stop solution" was added to change the color from blue to yellow, and the intensity was measured at 450 nm. Color intensity is proportional to the concentration of PF4 within the sample and can be obtained from the standard calibration curve of absorbance intensity vs. concentration; the calibration curve was constructed with the following known PF4 concentrations: 0 pg/mL, 4.12 pg/mL, 12.35 pg/mL, 37.04 pg/mL, 111.1 pg/mL, 333.3 pg/mL, 1000 pg/mL, and 3000 pg/mL (**Figure 3.4**).
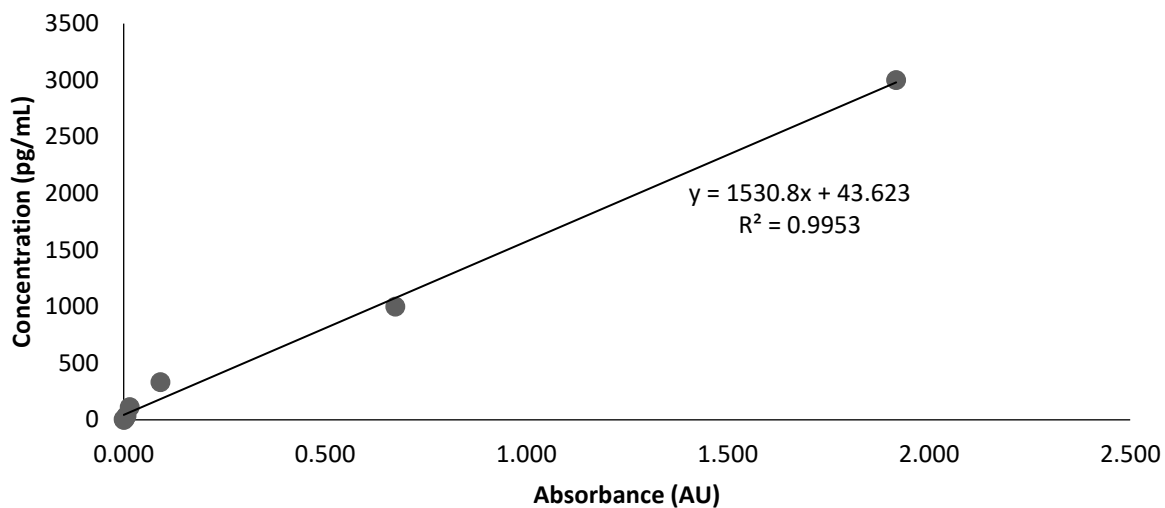
Figure 3.4. PF4 protein standard calibration curve. Curve constructed from known PF4 concentrations 0-3000 pg/mL.

All PF4 data were normalized to the protein concentration obtained using a Pierce BCA Protein Assay kit. Samples were diluted 1:10 with 25 µL of diluted sample or standard placed into individual wells. Working reagents were prepared in parts 20 A: 1 B, and 200 µL was added to each well. The plate was then incubated at 37°C for 30 min and read at 562 nm. Protein intensity within each well was obtained by using the standard calibration curve of known PF4 concentrations: 0, 25, 125, 250, 500, 750, 1000, and 1500 µg/mL (**Figure 3.5**).
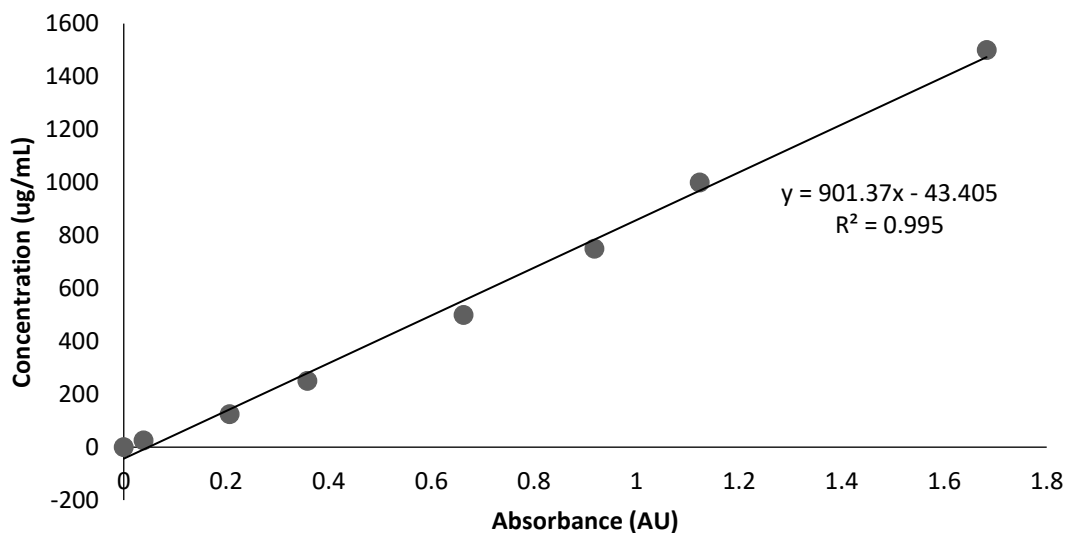
Figure 3.5. BSA protein standard calibration curve. Calibration curve constructed from known BCA concentrations 0 – 1500 µg/mL.

3.3.9 PF4 Data Analysis and Statistics

Calculated PF4 data were analyzed for outliers similarly to the CFMA outlier test. The number of mice used were 6 from control, 3 from ascending parasitemia, and 3 from descending parasitemia. Data from two control mice were eliminated due to the interior or exterior PF4 failing the outlier test. One biological replicate here consists of three technical replicates. A one-way ANOVA test was completed to determine the statistical differences between the conditions.

3.4 Results and Discussion
3.4.1 MC Secretion at the Single Cell Level

Studying MC secretion at the single cell level allows both quantitative and dynamic temporal information about degranulation to be obtained. Since significant findings were observed for platelets in Chapter 2 with *P. chabaudi* at ascending and descending parasitemia stages,[16] the work herein proceeded with the use of CFMA to obtain information on MCs collected from the same malaria stages vs. control (**Figure 3.6**). The amperometric traces shown here show individual dense granule secretions (each spike) from individual mast cells. Spike-by-spike analysis yields significant biophysical insight into the chemical messenger secretion process in the disease conditions.
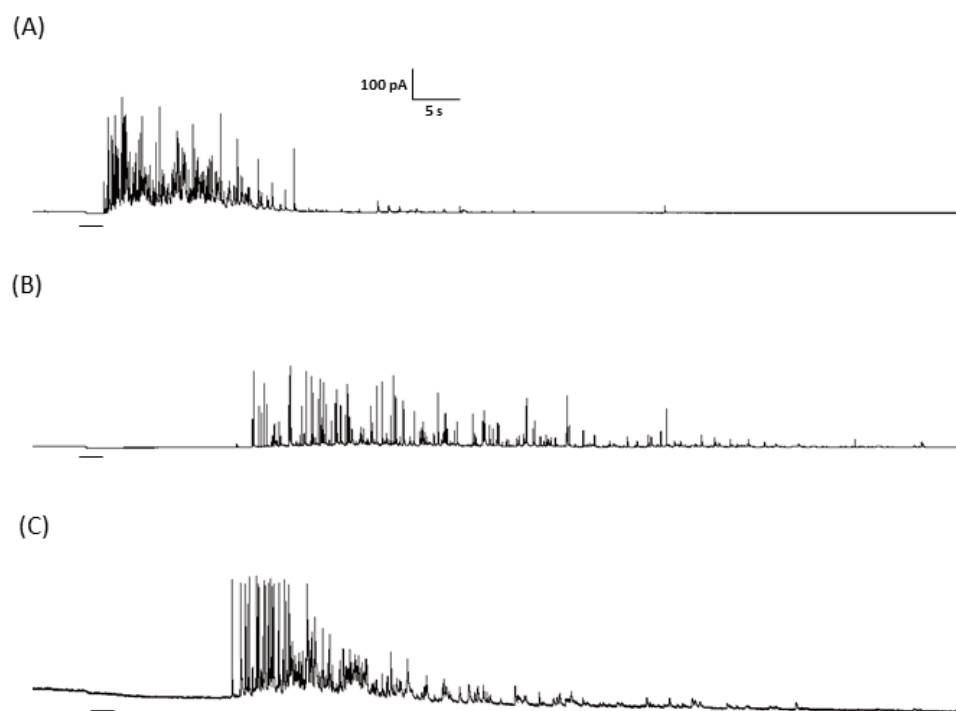
Figure 3.6. Representative traces of MCs. (A) Control, (B) ascending parasitemia, and (C) descending parasitemia. The scale bar shown in panel (A) applies to all panels. The small bar under each trace represents the of application of the calcium ionophore A23187.

A comparison of MC to platelet traces in Chapter 2 indicates more 5-HT released from MC vs. platelet as shown by the scale bars of their representative traces. Furthermore, MC released have more spikes overlap indicating closer granules released vs. platelet released. Thus, MC peaks analyses were more time-consuming with more analyses conducted by hands. From the quantitative dataset, during the ascending stage, mast cells release fewer 5-HT molecules from each granule (19% smaller charge (Q) vs. the negative control), whereas, during the descending stage, mast cells release more 5-HT molecules with each secretion event (37% higher Q vs. negative control) (**Figure 3.7A**). This difference suggests that malarial stage significantly impacts MC performance, with more inflammatory mediators being released when the red blood cell-contained parasite has been present for a longer time period. By examining the number of amperometric spikes per cell, revealing the number of exocytosis events per cell following stimulus, the MCs from both malaria conditions have more degranulation events than the malaria-free control, 42% more in ascending parasitemia and 47% more in descending parasitemia (**Figure 3.7B**). To effectively get a sense of the average total

5-HT released per MC, the charge was converted to molecules of 5-HT per spike using Faraday's law, noting the two electrons involved in oxidation, and multiplying by the average number of spikes per cell. From the dataset, the descending parasitemia condition showed 110% more 5-HT released per cell vs. the negative control, whereas there was no statistical difference between the ascending parasitemia vs. negative control (**Figure 3.7C**). The main factor contributing to this difference is in the high biological heterogeneity of the number of 5-HT molecules released from each granule during descending parasitemia condition. Taken together, MCs in both malaria conditions undergo more secretion events vs. the negative control; however, only the MCs in the descending parasitemia condition release more 5-HT per cell.
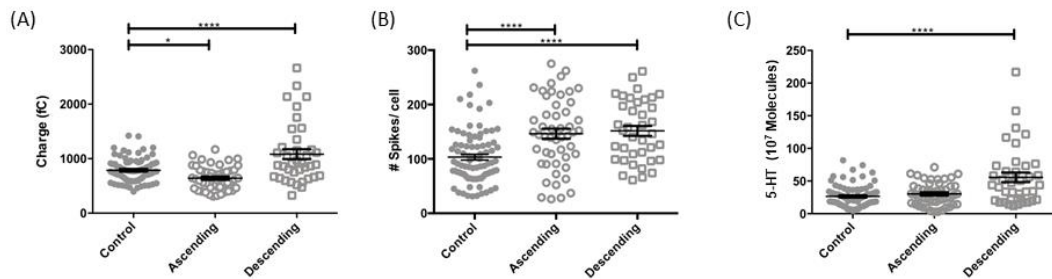
Figure 3.7. CFMA quantitative parameters. (A) Charge (Q), (B) number of spikes per cell, and (C) total 5-HT molecules secreted. Results shown in plots are the mean ± SEM. Each symbol within the figures is representative of one MC. Number of MCs: control ($n = 60$), ascending ($n = 50$), and descending ($n = 38$). *$P \leq 0.05$ and ****$P \leq 0.0001$.

By analyzing each individual amperometric peak that represents an individual granule fusion event within an individual MC, information on temporal dynamics can be obtained to reveal parasite-induced impacts on fusion pore opening duration (time at full-width-half-maximum or $T_{1/2}$), fusion pore opening mechanism (T_{rise}), and the fusion pore closing mechanism (T_{decay}), all of which impact the dynamics of chemical messenger delivery from MCs. $T_{1/2}$ gives information on the rate at which the matrix expands to secrete granular-bound 5-HT. T_{rise} is the time from 10% to 90% of spike maximum rising phase and gives information regarding the fast secretion of 5-HT unassociated with the intragranular matrix following fusion pore formation. T_{decay} is the time from 90% to 10% of spike maximum decaying phase and gives information on the rate of fusion pore reclosing as chemical messenger secretion slows and stops. From the dataset, $T_{1/2}$ was 14% shorter in ascending parasitemia vs. negative control, whereas no difference was observed

between descending parasitemia vs. control (**Figure 3.8A**). T_{rise} in the ascending parasitemia stage was 15% shorter pore vs. control, and in the descending parasitemia was 26% longer vs. control (**Figure 3.8B**). Furthermore, T_{decay} was 12% shorter in the ascending vs. control, but was not affected in the descending parasitemia (**Figure 3.8C**). Based on the dataset, the shorter pore opening duration, faster pore opening, and faster pore closing contributed to the smaller charge (fewer 5-HT molecules) per event for the ascending parasitemia stage. Thus, this suggests that the dynamics of MC degranulation during the ascending parasitemia stages have been affected at this fundamental level of the degranulation process. From the descending parasitemia stage, only the fusion pore opening time is longer vs. negative control, suggesting that there were more 5-HT molecules within the intragranular polyphosphate matrix of the MCs during descending parasitemia vs. negative control. Clearly, MCs from different parasitemia stages are affected in nuanced ways.
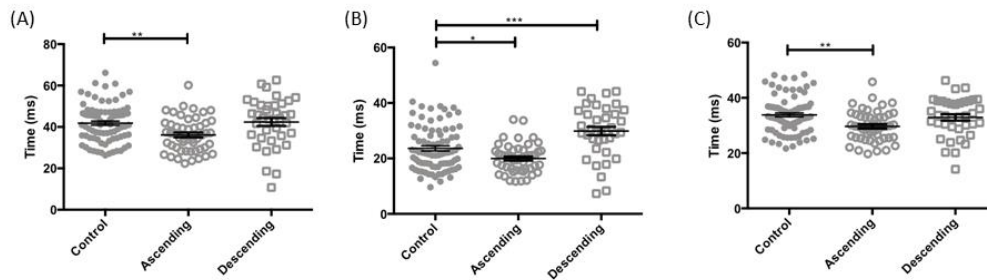
Figure 3.8. CFMA kinetic parameters. (A) Time at full-width-half-maximum ($T_{1/2}$), (B) Time from 10-90% of peak rising (T_{rise}), (C) and time of 90-10% of peak decaying (T_{decay}). Results shown in plots are the mean ± SEM. Number of MCs: control ($n = 60$), ascending ($n = 50$), and descending ($n = 38$). *$P \le 0.05$, **$P \le 0.01$, and ***$P \le 0.001$.

Other key information about the characteristics of secretion during MC degranulation can be obtained by analyzing the profile of each individual exocytosis event. Typical or traditional secretion events are indicated with a fast rise in current followed by a slow exponential decay, with any peak deviating from this description being categorized as a non-traditional event (NTE) (**Figure 3.9A**). The presence of NTE events has been shown to reveal information on the different modes of exocytosis.[17] Both traditional and non-traditional events can be accompanied by pre- and/or post-foot features with these "foot" features revealing information on the styles of fusion pore opening and closing as the granule interacts with the inner cell membrane.[17] By visually analyzing each magnified

peak and accounting for the pre- and post-foot and NTE events (**Figure 3.10**), neither ascending nor descending parasitemia conditions exhibit any statistical difference in pre- or post- spike foot appearance (**Figure 3.9B**).
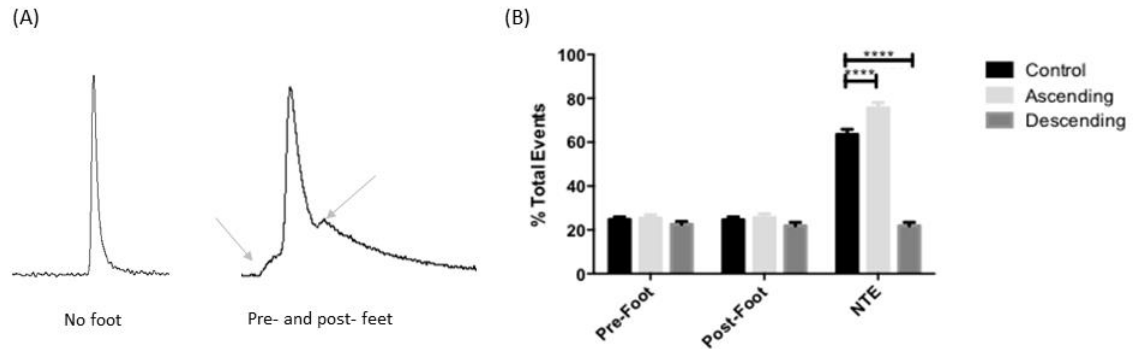
Figure 3.9. Foot features. (A) A traditional event with fast rise and slow decay without (left) and with (right) pre- and post-foot features. A non-traditional event (NTE) is classified as any event without the typical fast rise and slow decay features found in traditional events. (B) A comparison of pre- and post-spike foot and non-traditional event counts in control vs. malaria conditions (ascending and descending parasitemia). Number of MCs: control *(n = 60),* ascending *(n = 50),* and descending *(n = 38).* ***P ≤ 0.0001.
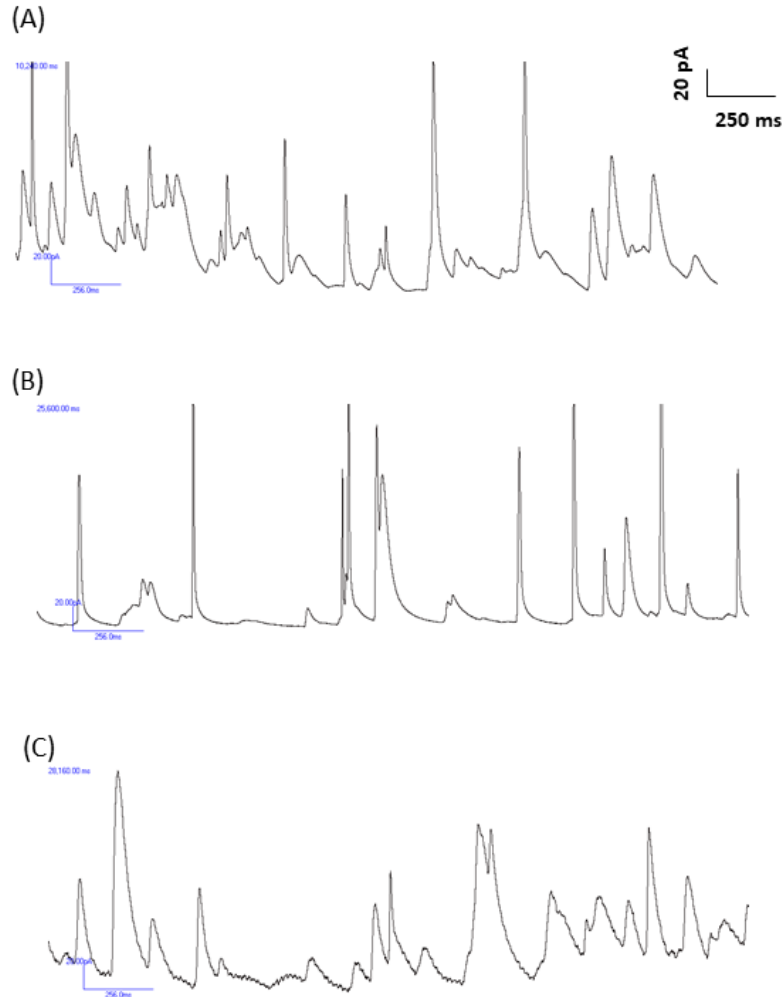
Figure 3.10. Magnified version of representative spike features. (A) Control, (B) ascending parasitemia, and (C) descending parasitemia. Features accounted for were traditional vs. non-traditional spikes and the presence of pre- and/or post- foot. The scale bar in panel (A) applies to all panels.

However, there were 19% more NTE in the ascending parasitemia condition vs. negative control and 66% fewer NTE in the descending parasitemia condition vs. negative control (**Figure 3.9B**). Since pore opening duration ($T_{1/2}$) did show significant differences among the malaria vs. control conditions, this suggests that pore sustainability is affected during malarial infection and is a major player in the NTE observed. Previous work has suggested that pre- and post-spike foot features could reveal information on the styles of pore opening and closing, linking to the two dynamic features, T_{rise} and T_{decay}; however, by doing the comparison with the MC data collected here, no correlation was obtained. Thus, further analysis to categorize the different type of pre- and post-foot features were not completed.

3.4.2 A Comparison of Chemical Messenger Secretion from MCs to Platelets

Based on precedent work in Chapter 2 that examined the impact of ascending and descending parasitemia on chemical messenger secretion from blood platelets, this work aimed to correlate platelet secretion measurements with the MC secretion measurements. While 5-HT from mast cells can be detected using electrochemistry, the chemical messenger of interest here from platelets, PF4, is not electroactive. As such, experiments were performed to compare the quantitative information (5-HT molecules) from the CFMA on MCs dataset to platelet PF4 measured from the same mice, using ELISA to examine correlation between the two cell types. The ELISA results indicate that there was 131% more intracellular PF4 in the descending parasitemia vs. negative control conditions (**Figure 3.11A**). The PF4 trend is comparable to that measured for 5-HT in MC, suggesting that the effect of *P. chabaudi* on MCs and platelets is similar. Unfortunately, ELISA does not allow for the same kind of dynamic measurement that can be accomplished with CFMA, so a comparison of secretion dynamics cannot be done here. However, a comparison of the current CFMA on MCs to previously published data on CFMA with platelets[16] show similar trends for platelets and MCs in the descending parasitemia stage; however, there are quite distinct dynamics for the two different cell types in the ascending parasitemia stage. For instance, platelets from the ascending parasitemia stage showed a longer time trend in $T_{1/2}$ (27%) and T_{rise} (35%), and no effect on T_{decay} vs. negative control platelets, whereas, MCs from the ascending parasitemia stage showed shorter time trend in all three parameters. Comparing the exocytosis machinery of platelet and MC, similar SNARE proteins[18-19] were involved in the exocytosis process. However, the intragranular matrix composition within MC and platelet are different[20-21] and may account for part of the difference in dynamics. Furthermore, a comparison of NTE count in MCs and platelets of malaria vs. negative control shows more NTE for both cell type. This suggests that the malaria parasites affect the exocytosis process of MCs and platelets. However, further work still needs to be completed to determine the different modes of NTE and whether MCs and platelets would have similar NTE modes.

Since PF4 has been shown to be associated with malaria infection,[22-26] analysis of the PF4 in the extracellular fraction was also measured. From the data, both platelets collected during ascending and descending parasitemia stages contained 72% and 63% lower amounts, respectively, of PF4 extracellularly vs. negative control conditions (**Figure 3.11B**). This is different than what was expected since the presence of the malaria parasite

in a live mouse model was thought to contribute to platelet activation and release of PF4 into the extracellular space. However, it is possible that the low amount of detected PF4 in the extracellular space is not representative of the secreted PF4 as secreted PF4 is known to bind to activated platelets and other cell types during malarial infection,[25] and bound PF4 would not be detected here.
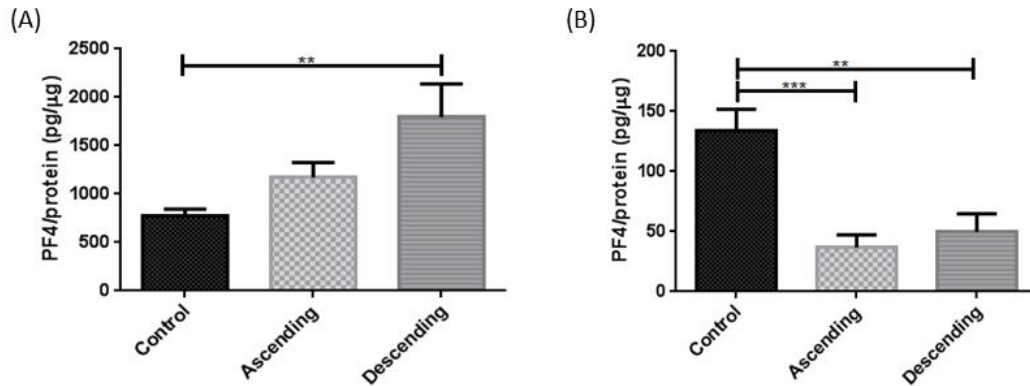
Figure 3.11. Platelet factor 4 (PF4) collected from platelet. (A) intracellular and (B) extracellular compartments and measured using ELISA. Number of biological replicates: control ($n = 4$), ascending ($n = 3$), and descending ($n = 3$). **P ≤ 0.01 and ***P ≤ 0.001.

3.5 Conclusions

CFMA was used to measure quantitative and dynamic MC degranulation from both malaria and healthy control conditions. The results show that different stages of malarial infection have differential impacts on the mast cell degranulation mechanism and suggest that more inflammatory mediators were released from MCs when the red blood cell-contained parasite has been present for a longer time period Thus, this may help to explain the variation of MC degranulation and malaria disease progression. A comparison of MC secretion to platelet PF4 levels showed similar trends in quantitative release during the descending parasitemia stage of malaria. However, comparison with previously published platelet results on 5-HT secretion show distinct secretion trends behavior between the two cell types in the ascending parasitemia stage. The differences could be associated with the location of collected platelets (blood stream) and MCs (peritoneal cavity) and potential time at which they encounter the malaria parasites. Although, no work has been conducted to determine whether MCs from different sites within the biological system would be comparable to one another. Overall, this work affirms the importance of consideration of

infection stage in future malaria studies and treatments and shows that inflammatory response by MCs may play a critical role in disease implications.

Chapter 4

Antimalarial Drugs Impact Chemical Messenger Secretion by Blood Platelets
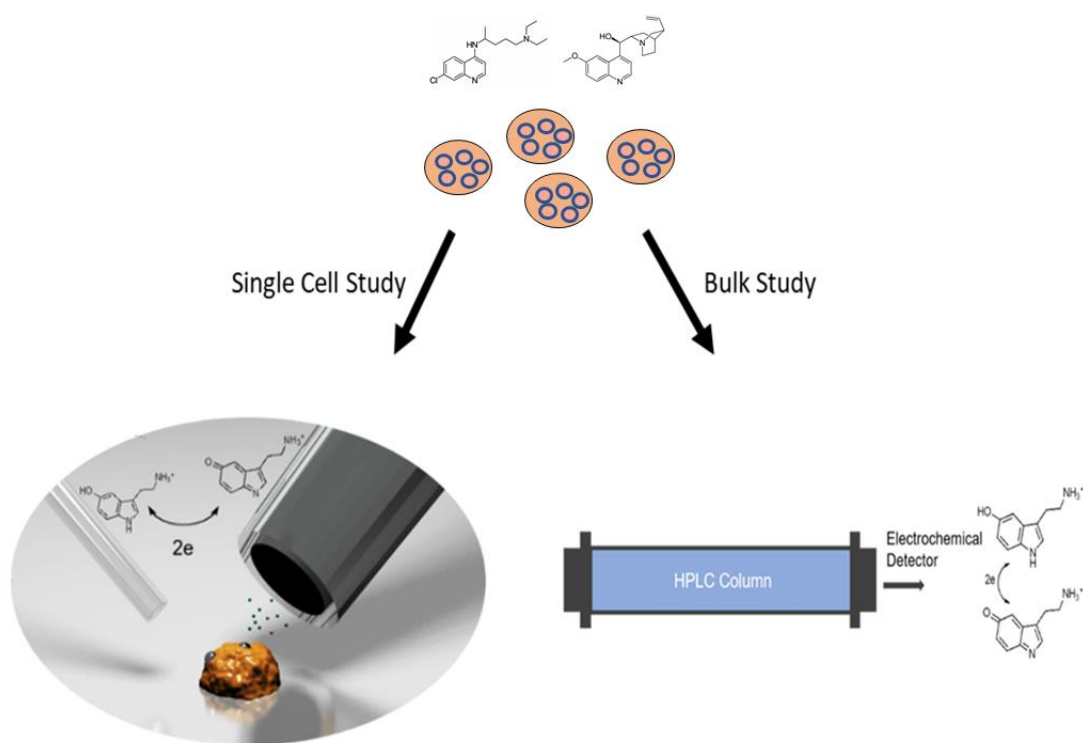
4.1 Overview

In this chapter, the effects of antimalarial drugs on platelets were explored at both the bulk and the single cell levels. Advances in antimalarial drug development are important for combating malaria. Among the currently identified antimalarial drugs, it is suggested that some interact directly with the malarial parasites while others interact indirectly with the parasites. While this approach leads to parasite elimination, little is known about how these antimalarial drugs impact immune cells that are also critical in malarial response. Herein, the effects of two common antimalarial drugs, chloroquine and quinine, on platelets were explored at both the bulk level, using high performance liquid chromatography (HPLC), and the single cell level, using carbon-fiber microelectrode amperometry (CFMA), to characterize any changes in chemical messenger secretion. The data reveal that both drugs cause platelet activation and reduce the number of platelet exocytosis events as well as delay fusion pore opening and closing. This work demonstrates how chloroquine and quinine quantitatively and qualitatively impact in vitro platelet function.

4.2 Introduction

Malaria is an infectious disease caused by the Plasmodium parasites that are transmitted through the bites of infected female Anopheles mosquitos.[1] Five known Plasmodium species cause malaria in humans, with the most prevalent and dangerous being *Plasmodium falciparum* (mostly found in sub-Saharan Africa) and *Plasmodium vivax* (mostly found in South America, Asia, and Oceania).[1] Overall, there were an estimated 219 million cases of malaria in 90 countries and 435,000 deaths in 2017, with high *Plasmodium falciparium* infection incidence rate being in regions of Africa, South-East Asia, the Eastern Mediterranean, and the Western Pacific regions, and high *Plasmodium vivax* being in region of the Americas.[1] Though there has been recent progress toward a vaccine, current treatments for malaria rely on antimalarial drugs, with the primary aim being elimination of the malarial parasites.[2]

Although much of the action regarding antimalarial drugs and malarial parasite elimination have been well-characterized, few studies have been done on the effects of antimalarial drugs on critical immune cells. Of interest here are platelets, anuclear cell bodies circulating in large numbers within the bloodstream, which are known for their roles in multiple defense mechanisms and wound healing.[3] The role of platelets in immune response involves the release of chemical messengers from their alpha, dense, and

lysosomal granules to activate other immune cells, such as leukocytes, and amplify the immune response toward malarial parasite destruction and clearance.[4] Thus, it is hypothesized that antimalarial drugs may also have an off-target effect on platelets, a key component in the immune response, and will influence their critical delivery of chemical messengers.

The work in this chapter utilized both bulk platelets and single platelet measurements to gain deep biophysical understanding about how platelets, from two model species, are affected by two different antimalarial drugs: chloroquine (CQ) and quinine (QN). The mouse model is widely used in malaria studies and is, thus, a reasonable model to study the effect of antimalarial drugs on platelets. Previous work exploring the role of platelets in malaria have used the mouse model.[4-8] Furthermore, although platelets are known to share common features, functional responses are known to be different among different species.[9] As such, both mouse and rabbit platelets were studied herein to investigate the generality of any impacts the antimalarial drugs may have on platelets.

The two analysis methods used are high performance liquid chromatography (HPLC) coupled to an electrochemical detector, which focuses at the bulk cell level to quantitatively understand general platelet population information, and carbon-fiber microelectrode amperometry (CFMA) at the single cell level to quantitatively and qualitatively understand biophysical heterogeneity within the platelet population. Both methods take advantage of the redox activity of the serotonin, or 5-hydroxytryptamine (5-HT), that is found in dense granules.[10-12] HPLC coupled to an electrochemical detector was used to probe for bulk platelet exocytosis following drug treatment of naïve platelets to give information regarding how the drugs influence cell-cell interactions that are critical during immune response. Results suggest that the tested drugs did not inhibit platelet activation as indicated in the literature,[13-14] but rather enhanced it. In CFMA, the small size of the microelectrode and fast time resolution (sub-millisecond)[15-16] enables study of real-time chemical messenger release from individual granules from single platelets,[11] neuroendocrine cells,[17] or mast cells.[18]

Herein, CFMA was used to explore how common antimalarial drugs influenced platelet secretory machinery. Results indicate that both drugs reduce the number of granule fusion events and delay fusion pore opening and closing based on measured 5-HT release. Quantitative information from the bulk platelet measurements was shown to agree well with averaged information from a population of single cell measurements,[10, 19]

suggesting that the antimalarial drugs QN and CQ do not selectively act on different subpopulations of platelets or platelet granules.

4.3 Materials and Methods

4.3.1 Materials

Acid citrate dextrose solution (ACD) was prepared by combining 41.64 mM citric acid ($C_4H_8O_7$), 76.16 mM sodium citrate ($Na_3C_6H_5O_7$), 11.10 mM dextrose ($C_6H_{14}O7$), and deionized water and pH to 5.1. Tyrode's buffer was prepared by combining 117 mM sodium chloride (NaCl), 2.62 mM potassium chloride (KCl), 0.52 mM magnesium chloride hexahydrate ($MgCl·6H_2O$), 5.55 mM D-glucose ($C_4H_{12}O_6$), 5 mM 4-(2-hydroxyethyl)-1-piperazineethanesulfonic acid (HEPES), 12.14 mM sodium bicarbonate ($NaHCO_3$), and deionized water and pH to 7.2-7.4. Perchloric acid was prepared to final concentration of ? from stock. 5-HT and dopamine standards were prepared to specified concentration using prepared perchloric acid. HPLC mobile phase was prepared by combining 11.6 mg/L sodium octyl sulfate, 170 µL/L dibutylamine, 55.8 mg/L Na2EDTA, 10% methanol, 203 mg/L anhydrous sodium acetate, 0.1 M citric acid, 120 mg/L sodium chloride, and water. Electrolyte solution was prepared using 3.0 M potassium acetate ($C_2H_3KO_2$) and 30.0 mM potassium chloride (KCl). Thrombin was stock prepared to 500 U/mL using Tyrode's buffer and diluted per experiment. pH adjustment was done using sodium hydroxide and hydrochloric acid. All materials were purchased from Sigma-Aldrich and used as received or prepared into specific solution. Deionized water (18.2 MΩ·cm) was purified using a Milli-Q Millipore water purification system (Billerica, MA).

Chloroquine diphosphate was purchased from Fisher Scientific (Waltham, MA) and quinine dihydrochloride was purchased from VWR International (Radnor, PA). C57BL/6J mice and New Zealand white rabbits were purchased from Jackson Laboratories through Research Animal Resources (UMN, Twin Cities).

4.3.2 Platelet and Drug Preparation

Blood from three mice and two rabbits were collected according to IACUC protocol #1702-34571A and protocol #1610-34243A, respectively. The number of biological replicates for the rabbits was based on limitations in approved IACUC protocols, though control results from the rabbit platelets are in good agreement with previous work when the rabbits used were, in fact, distinct biological replicates. Mouse blood was collected via cardiac puncture into pre-filled syringes with acid citrate dextrose solution, whereas rabbit

blood was collected from the mid-ear artery of a rabbit after sedation into ethylenediaminetetraacetic acid (EDTA) containing tubes. Blood from both species were diluted in Tyrode's buffer, separated, and purified according to previously published protocols to obtain platelets in the platelet-rich plasma (PRP) layer.[9] All experiments were conducted on the same day as blood collection.

Purified platelets were combined and diluted to $10^7 – 10^8$ cells/mL, then aliquoted into three portions (three technical replicates) prior to incubating in drugs for both bulk and single cell studies. Chloroquine diphosphate and quinine dihydrochloride were prepared to final concentrations of 0, 0.1, 10, and 1000 µM in Tyrode's buffer for HPLC bulk cell studies and to 1000 µM for CFMA single cell studies. 0 - 10 µM concentrations were chosen based on a biologically relevant range[20-21] with the 1000 µM concentration chosen to see what effects can be observed at high, non-physiological concentrations. The highest concentration was chosen for single cell studies based on the effects observed in bulk cell studies. All drug concentrations were compared to the 5 U/mL thrombin (positive control).

4.3.3 Bulk Cell HPLC Experiments

HPLC analysis of prepared standards and samples were run according to a previously established protocol.[22] A series of 5-HT standards were prepared in 0.5 M perchloric acid to final concentrations of 0.0625, 0.125, 0.250, 0.500, and 1.00 µM with 5.00 µM dopamine added as an internal standard. A total of 125 µL of prepared platelet samples were combined with 125 µL of drug (diluted in Tyrode's buffer) or a negative control (Tyrode's buffer) and incubated for 1.5 h at 37 °C. Following incubation, samples were centrifuged at 800×g, and the supernatant was saved for further analysis. Pelleted platelets were re-suspended in Tyrode's buffer to 125 µL and incubated with 5 U/mL of thrombin (Sigma-Aldrich) for 1 h at 37 °C. Then, all samples including the lysis products were filtered using a Millipore 96 well Multi Screen HTS filter plate with a 0.45 µm pore and centrifuged at 3000×g for 5 min. All filtered samples were run on an Agilent 1200 HPLC with an auto sampler containing a 5 µm, 4.6 × 150 mm C18 column (Eclipse XDB-C18) attached to a Waters 2465 electrochemical detector with a glassy carbon-based electrode. The working potential was set at +700 mV vs. an in situ Ag/AgCl reference electrode with a current range up to 50 nA. Samples were separated in the HPLC column at a flow rate of 2 mL/min in an aqueous mobile phase mixture. The chromatographic technique works using a C18 column to separate different platelet

exocytosis products based on their interaction strength with the stationary phase; then, the redox-active chemicals can be detected electrochemically (**Figure 4.1A**). Based on calibration with a series of 5-HT standards, the integrated peak area at ~2 min can be used to quantify the released 5-HT from platelets under various conditions (**Figure 4.1B**). Neither CQ nor QN interfere with detection of 5-HTat +700 mV vs. Ag/ AgCl.
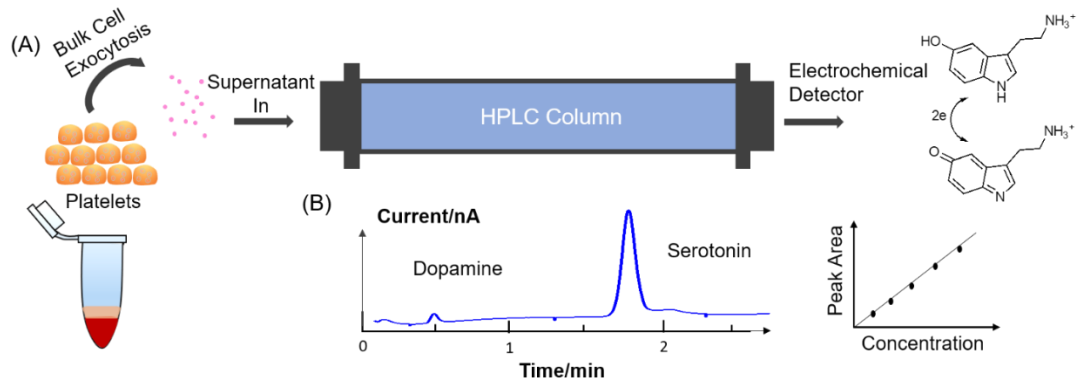
Figure 4.1. Schematic diagram of HPLC set up for bulk platelets' chemical messenger detection. (A) The bulk platelet exocytosis products were injected and separated on the C18 HPLC column and then detected electrochemically at +0.7 V vs. Ag/AgCl. (B) The relationship between peak area and 5-HT concentration was characterized in advance to find the concentration of released serotonin after drug stimulation of bulk platelets.

4.3.4 Single Cell Experiments

Carbon-fiber microelectrodes were fabricated in the laboratory as described in previous literature.[23] Prior to usage, the electrodes were polished to 45° on a diamond polishing wheel (Sutter Instruments) and stored in isopropyl alcohol. The electrodes were backfilled with electrolyte solution (3.0 M potassium acetate and 30.0 mM potassium chloride) prior to being mounted on a platinum-coated silver wire (Squires Electronics) situated on a headstage mounted on an Axon Instruments Axopatch 200 B potentiostat (Molecular Devices Inc.) using low-pass Bessel filtering (5 kHz), a sampling rate of 20 kHz, and gain amplification of 20 mV/pA controlled by locally written LabVIEW software and National Instruments data acquisition boards. This potentiostat controlled the applied voltage at +700 mV vs. a silver/silver chloride (Ag/AgCl) reference electrode (BASi). A pulled glass capillary micropipette loaded with 5 U/mL of thrombin (Sigma-Aldrich) connected to a Picospritzer III (Parker Hannifin) was used to control delivery of the stimulating thrombin solution to the cells. Both the headstage of the mounted electrodes and micropipette were mounted on Burleigh PCS-5000 piezoelectric

micromanipulators (Olympus America Inc.) to control electrode and stimulant placement relative to individual platelets. A drop of platelet suspension was placed onto a poly-L-lysine-coated glass coverslip containing Tyrode's buffer. Individual platelets were visually monitored using an inverted microscope equipped with phase contrast optics (40× magnification) (Nikon Instruments, Melville, NY). Upon the start of a measurement, the stimulating micropipette delivered a 3 s dose of the stimulant, inducing platelet degranulation. The current was recorded with time resolution of milliseconds so that it was possible to compare the real-time secretion behavior after different drug treatments. The carbon-fiber microelectrode, which is large enough to cover the entire diameter of the platelet, was placed close to the platelet surface so that, after stimulation, the released 5-HT molecules were oxidized and detected by the electrode (**Figure 4.2**). Further analysis of current versus time traces for individual cells provides both quantitative and qualitative information to allow comparison of platelet exocytosis events.

Collected amperometric traces were processed using Tar Heel software (courtesy of Dr. Michael Heien), processed at 200 Hz with a lowpass Bessel filter, and analyzed using Minianalysis software (Synaptosoft, Inc.) with the signal-to-noise ratio set at 2. Individual current spikes within an amperometric trace represent individual granular release events. For each platelet trace, the area under each spike (Q), number of spikes per platelet (N), and time at full-width half maximum of each spike ($T_{1/2}$) were measured, averaged, and statistically analyzed for outliers. Additional analyzed parameters consisted of 1) the time from 10% to 90% of the peak current on the rising phase (T_{rise}), 2) the time from 90% to 10% of peak current on the decay phase (T_{decay}), and 3) the total 5-HT molecules released from an individual platelet. Since the oxidation of 5-HT involves a two electron transfer, the total 5-HT molecules released per platelet measurement was calculated using Faraday's Law after taking the product of Q and N. If a cell was a statistical outlier for any analyzed parameter, the trace was eliminated altogether. Statistical determination of outliers included taking the log of the individual average spike parameter, obtaining the average from the individual log parameter, determining the standard deviation from the log parameter, and discarding any amperometric traces whose log value fell outside two standard deviations of the average of the individual log parameter. Experimental condition averages were calculated for each spike parameter using one-way ANOVA with 95% confidence level as threshold for statistical significance
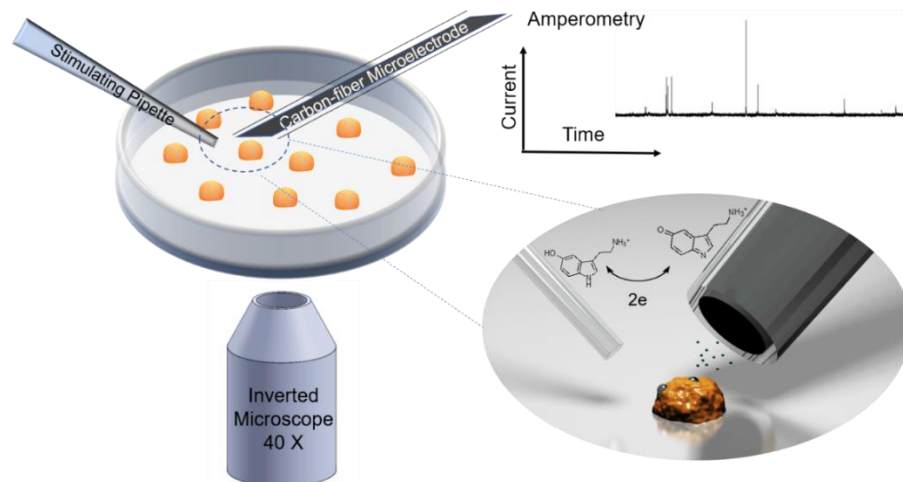
Figure 4.2. Schematic of carbon-fiber microelectrode amperometry (CFMA) setup. A polished carbon fiber microelectrode was placed close to the surface of a single platelet so that the secreted 5-HT molecules can be oxidized at the surface after stimulation, and the current vs. time amperometry trace is recorded for detailed biophysical analysis.

4.4 Results and Discussion

4.4.1 Effects of Chloroquine and Quinine on Bulk Platelets Secretion of 5-HT

Literature on the effects of CQ suggests that the drug inhibits platelet aggregation through the interaction between CQ and membrane glycoproteins and receptors as well as the binding between CQ and membrane phospholipids.[24] Likewise, QN has been shown to affect platelet structure by perturbing the membrane as well as function through aggregation.[25-26] To characterize the effects of CQ and QN on platelets beyond aggregation, HPLC was used to quantitatively determine secretion of 5-HT following varied treatment with CQ or QN; these data were used to choose the drug concentration to be used for the single cell studies. Furthermore, both drugs were explored for their abilities to either promote or prevent platelet activation via 5-HT secretion following thrombin stimulation. Although there is no known role for 5-HTsecretionin the presence of CQ and QN, in this work, 5-HT is a measurable species that is co-released with other granule chemical messengers during platelet activation. Thus, 5-HT secretion is used as a proxy for other platelet chemical messengers such as platelet factor 4 that have known roles in malaria and are co-localized and co-released with 5-HT to understand how platelet function is affected.[6, 27]

In the first set of experiments, the ability of each drug, at various concentrations, to directly activate platelets was explored. The data show that both drugs (at 1 mM) are able to induce 60–80 times greater platelet release of 5-HT for both mouse and rabbit

platelets when compared to the non-drug-treated negative control conditions; also, CQ induces nine times greater release of 5-HT from rabbit platelets at doses as low as 10 µM (**Figure 4.3A**). Although previous morphology studies on mouse and rabbit platelet aggregates showed no differences among platelets from the two species,[28] the species likely possess different receptors or functional responses, resulting in the observed sensitivity differences. In the second set of experiments, platelets incubated in drugs were monitored for their ability to promote or prevent further platelet activation via thrombin. Results confirmed that platelets from 1 mM CQ or QN conditions had indeed been activated previously, as indicated by significantly lower secreted 5-HT vs. control (pre-incubation only in Tyrode's buffer) (**Figure 4.3B**). In all cases but one, pre-exposure of platelets to CQ and QN appears to mitigate or not impact further activation by thrombin. The one outlier was in the case of rabbit platelets, where pre-exposure to 0.1 µM CQ led to a two-fold enhancement in released 5-HT vs. control (pre-exposure to buffer). Overall, the results suggest that the secretion efficiency of 5-HT from platelets and activation upon thrombin stimulation are enhanced rather than inhibited upon low concentration of pre-CQ exposure, whereas no effects are observed from low concentration of pre-QN exposure, and the low 5-HT release observed with the highest CQ and QN concentration is likely due to direct drug-induced platelet activation.
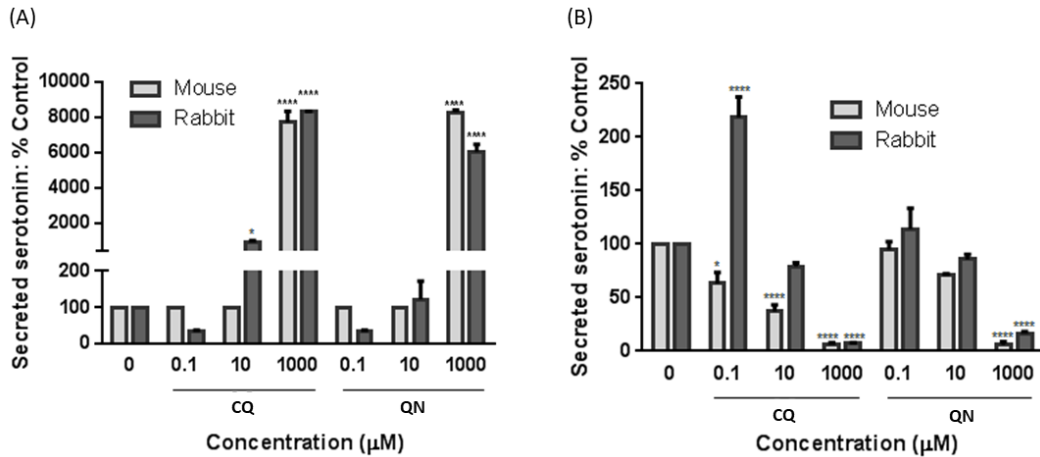
Figure 4.3. Comparison of mouse and rabbit bulk platelet secretion of 5-HT in response to drugs and thrombin. (A) Bulk cell secretion of 5-HT from mouse and rabbit platelets in response to chloroquine diphosphate (CQ) and quinine diphosphate (QN) at various concentrations. (B) Bulk cell 5-HT secretion from mouse and rabbit platelets from either buffer, CQ, or QN pre-incubation in response to 5 U/mL thrombin stimulation. Note the significantly different y-axis values in figures A and B. All drug-treated samples were compared to the control, set at 100%. Results are mean ± SEM. *$p \leq 0.05$, **$p \leq 0.01$ and ****$p \leq 0.0001$ t-test vs. control.

4.4.2 Effects of Drugs on Single Platelet Secretion of 5-HT

From bulk cell studies, it was clear that 1 mM CQ and QN were able to directly activate both mouse and rabbit platelets Herein, the effect of the 1 mM drug stimulation was explored at the single cell level using CFMA to provide quantitative, high time-resolution information to complement the HPLC data and qualitative understanding about the action of the secretion machinery during platelet exocytosis. Additionally, the high concentration of drugs were chosen for CFMA considering the short exposure time (3 sec) of platelets with the drugs into a large volume. These conditions were chosen to ensure that platelets undergo full exocytosis in the positive control. Because we hypothesized that the effects from the drug incubation on the platelets would occur ahead of thrombin stimulation, the intense single cell exocytosis measurements show the end result of those impacts. Here, no pre-drug incubation studies were completed as pre-treatment with drugs caused platelet activation before CFMA studies, and all drug-based stimulations were compared to stimulation by thrombin as the positive control. Concerns about potential apoptosis of platelets based on high drug concentrations[29] were allayed by the fact that the single cell platelet response rates to stimulation were not decreased compared to naïve controls.

Representative traces show the character of platelet secretion following drug-induced activation; in all cases, the drugs do induce secretion albeit showing a smaller response than that induced by thrombin (**Figure 4.4)** and a larger response than measured from unstimulated platelets or platelets stimulated only with buffer. Detailed analysis of all individual spikes from each single cell measurement indicated that platelets from both mouse and rabbit species responded similarly to stimulation by QN vs. control, with slight differences observed for CQ-based stimulation vs. control (**Table 4.1**).

From CQ stimulation on mouse platelets vs. control, there were 58% fewer exocytosis events, 78% fewer total 5-HT molecules released, and 55% longer pore opening time; whereas, CQ stimulation on rabbit platelets vs. control showed 99% higher average charge from each exocytosis event, 107% longer time at full width half max, and 109% longer pore closing time. From QN stimulation on mouse platelets vs. control, there were 38% fewer exocytosis events, 53% fewer 5HT molecules secreted, 49% longer time at full width half max, and 57% longer pore closing time; whereas from QN stimulation on rabbit platelets vs. control, there were, statistically significant, 61% fewer exocytosis events, 61% fewer 5-HT molecules secreted, 74% longer time at full width half max, and 76% longer pore closing time. Based on previous studies, mouse and rabbit platelets are known to present different concentrations of phospholipids, cholesterol, and SNARE proteins within

their cell membranes to assist with the exocytosis process;[9] it is likely these differences that account for the differences in pore stability observed between the two species.
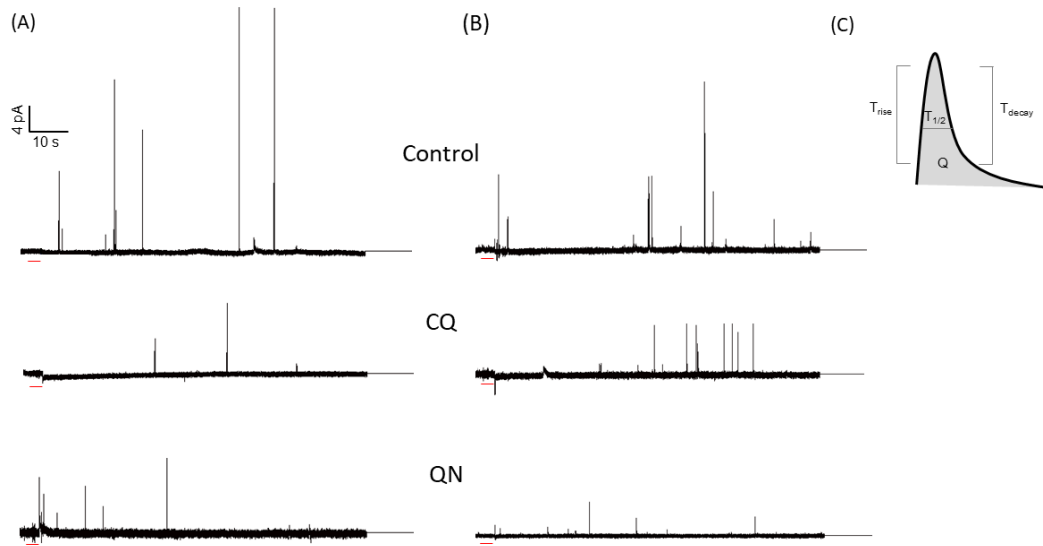
Figure 4.4. Representative amperometric traces recorded from individual mouse and rabbit platelets during single cell measurements. Panels showing (A) mouse platelet measurements from thrombin-stimulated (control), CQ-stimulated, and QN-stimulated and (B) rabbit platelet measurements from control, CQ, and QN. (C) Amperometric analysis of single spike with features labeled. Bars under each trace indicate the 3s of stimulant or drug delivery. The current and time scale is the same for all six amperometric traces and is indicated in the upper left corner of the figure.

Table 4.1. Single cell parameters from CFMA studies on mouse and rabbit platelets, where n is the total number of platelets analyzed in each condition. Results are mean ± SEM. $^*P \leq 0.05$, $^{**}P \leq 0.01$, $^{***}P \leq 0.001$, and $^{****}P \leq 0.0001$ t-test vs. thrombin (control) from the same species.

Parameter	Mouse			Rabbit		
	Thrombin	CQ	QN	Thrombin	CQ	QN
	(n = 23)	(n = 24)	(n = 26)	(n = 20)	(n = 24)	(n = 23)
Avg Q_{spike} (fC)	170.50±23.37	176.80±36.08	141.80±11.51	129.50±15.82	258.00±40.14*	134.00±28.45
Total spikes	232	102	162	297	216	134
Avg spikes	10.1±1.1	4.3±0.6***	6.2±0.6**	14.9±2.8	9.0±1.6	5.8±0.6**
Total 5-HT (10^6 molecules)	5.33±0.86	1.20±0.39***	2.53±0.22**	5.53±1.09	5.30±0.80	2.18±0.34*
Avg $T_{1/2}$ (ms)	14.03±1.17	21.75±2.57*	20.89±1.40*	11.42±0.84	23.59±2.36****	19.91±1.92**
Avg T_{rise} (ms)	6.63±0.64	9.12±1.37	9.43±1.14	6.06±0.52	8.94±1.13	6.95±0.75
Avg T_{decay} (ms)	13.37±1.17	18.46±2.22	20.41±1.22**	10.17±0.81	21.24±1.84****	17.64±1.45**

Overall, results from CQ and QN support that platelets are being activated by the drugs, although less intensely than that achieved with thrombin (5 U/mL, used as the positive control). The significant differences in $T_{1/2}$ and T_{decay} include contributions from the expansion/dissolution of the inorganic polyphosphate matrix[30] in the platelet dense granules as granule-bound 5-HT is secreted, as well as diffusion of oxidized 5-HT away from the working electrode and platelet pore closing. Additional analysis on the modes of platelet exocytosis were explored by examining "foot events", current shoulders that sometimes occur before or after full fusion current spikes. This analysis shows slight variation in pre- and post-foot features among the two different species (**Figure 4.5** and **Figure 4.6**); these data give insight into how long the platelet maintains a small diameter fusion pore before it dilates to allow maximal chemical messenger secretion.
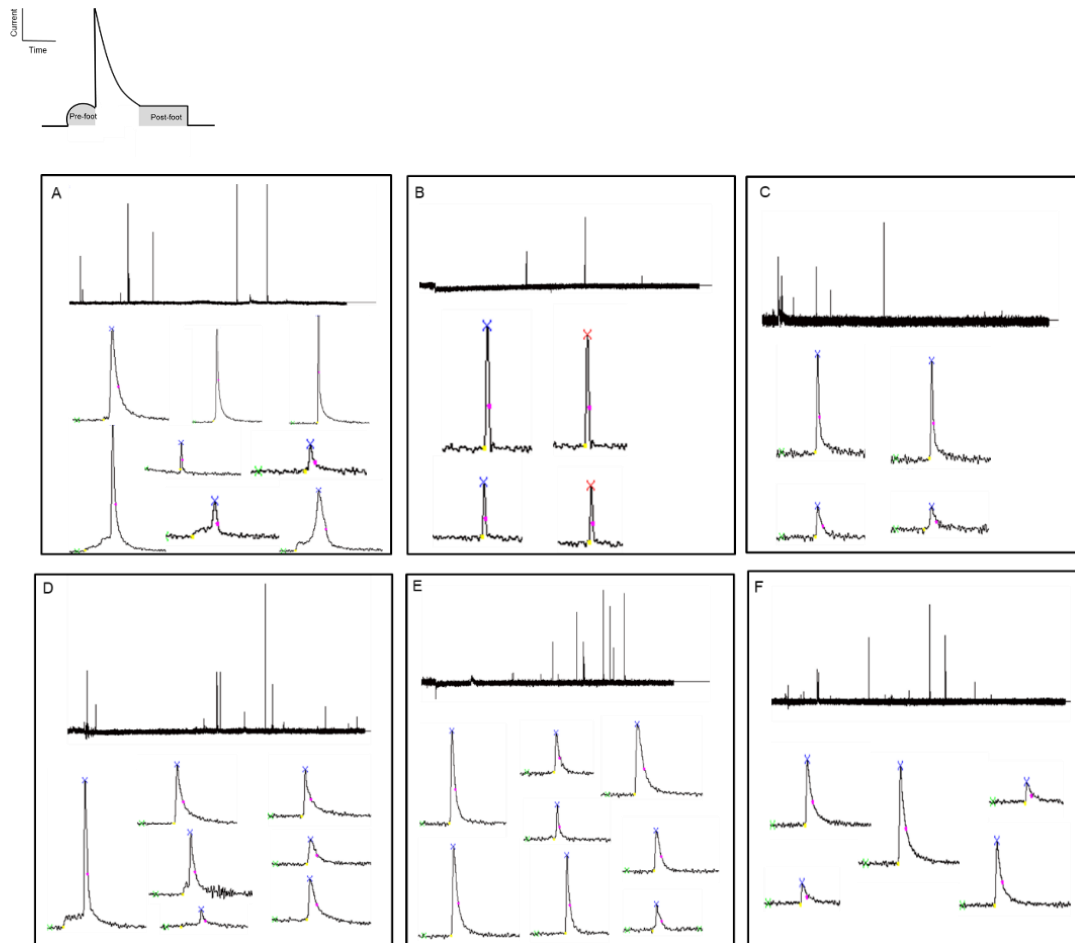
Figure 4.5. Schematic representation of and experimental examples of individual spike features. Pre-foot, post-foot, and non-traditional events for stimulation from (A) control (thrombin) for mouse platelets (B) CQ for mouse platelets (C) QN for mouse platelets (D) control (thrombin) for rabbit platelets (E) CQ for rabbit platelets, and (F) QN for rabbit platelets. Thrombin used was 5

U/mL and all CQ and QN conditions were 1 mM. Colored symbols within each peak represent the baseline, rise, peak, and decay.
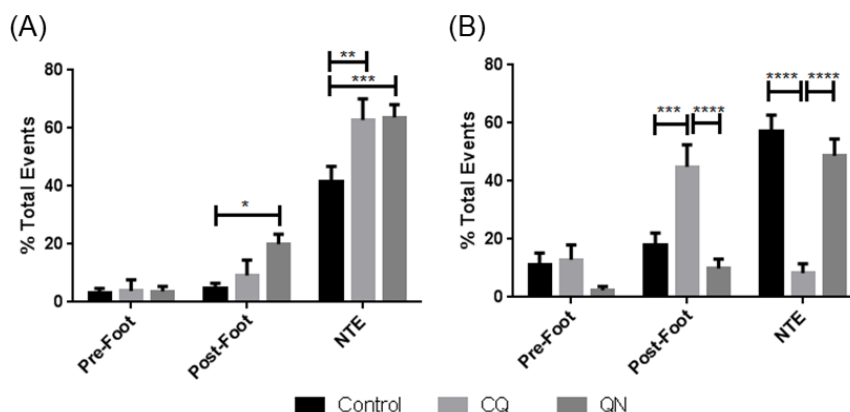
Figure 4.6. Platelet amperometric foot feature analysis. Pre-foot, post-foot, and non-traditional event (NTE) for control (thrombin), CQ, or QN-stimulation from (A) mouse and (B) rabbit platelets. NTEs are peaks not following the fast rise and slow decay expected from a typical current spike. Results are mean ± SEM. $^{*}P \leq 0.05$, $^{**}P \leq 0.01$, $^{***}P \leq 0.001$, and $^{****}P \leq 0.0001$ t-test vs. control.

The observable differences seen with CQ and QN-induced platelet activation for both mouse and rabbit platelets emphasized that, although both model species do share common features, there are subtle functional differences among them that are model specific. Although both CQ and QN drugs can cause platelet activation as indicated by both bulk and single cell studies at high drug concentrations, mouse and rabbit platelets respond differently to CQ at lower concentrations (0.1 and 10 μM). Additionally, this difference was also apparent when considering the functional responses obtained from the single cell studies with 1 mM CQ. Clearly, regardless of model species or antimalarial drug, the drug shows potential off-target impacts on platelets. These in vitro results do not necessarily reflect in vivo off-target effects but do suggest that they should be considered during future in vivo studies with antimalarial drugs.

4.5 Conclusions

Overall results within this chapter show that the tested antimalarial drugs, CQ and QN, impact naïve platelets and influence their critical delivery of chemical messengers, an important characteristic to keep in mind during malaria treatments. The nuance of the drug effects in these bulk studies shows the importance of using different species to study the

effects of antimalarial drugs. Furthermore, this work shows the importance of considering platelet behaviors beyond aggregation to understand the effects of antimalarial drugs on platelets for drug development as the findings here suggest that the drugs induce platelet activation.

Chapter 5

Concluding Remarks

5.1 Concluding Remarks

The field of malaria has made much progress toward prevention and control of the disease over the years, although disease elimination has not been possible. The work within this dissertation seeks to understand how cellular first responders, such as platelets and mast cells, are affected at the fundamental level during infection response. The single cell technique, carbon-fiber microelectrode amperometry (CFMA), was used to study both platelets and mast cells. Chapters 2-4 provide a compelling case for the use of CFMA in platelets and mast cells studies to reveal biological impacts of the disease and drugs used to treat the disease.

In Chapter 2, a mouse-malaria model and parasitemia stages were established in the lab. Then CFMA was used to study platelets from treated vs. control conditions with results indicating that the disease affected platelet function at early stages of infection and that the stages of infection are important considerations for future malaria work. In Chapter 3, mast cells were selected as the cell type for further study with malaria due to their presence throughout the biological system and their pivotal roles in immunity. The work in Chapter 3 demonstrated that mast cell degranulation was impacted similarly to platelets, although the mechanistic details were different. In Chapter 4, CFMA was used to study the impact of two selected antimalarial drugs on platelets. Results showed that the drugs impact platelet function and their critical delivery of chemical messengers. Future work should include how other common antimalarial drugs would impact mast cells using CFMA. This work has started with antimalarial drug, mefloquine; however, single cell measurements are still in progress. Furthermore, work should include how the malaria disease and antimalarial drugs together would affect platelet and mast cells degranulation. Ideally, all these in vitro measurements would be correlated with in vivo studies, both in the mouse model and with humans.

Although the work within this dissertation largely leveraged one single cell technique, there are many single cell techniques as discussed in Chapter 1 that could give further insight into cell response to malaria. Future studies of malaria should proceed using other single cell techniques to study relevant biomolecules secreted from platelets and mast cells. Structured illumination microscopy (SIM) can be used to image the exocytosis process. Then, a comparison of the images from the healthy vs. malaria conditions can be compared to the CFMA dataset. Mass spectrometry imaging (MSI) can be used to understand the impact of malaria on membrane components and provide a visual representation on the impact. MSI can also be used to understand how the

antimalarial drugs discussed in Chapter 4 impact platelets and mast cells by dye-tagging the drugs and monitoring for the distribution of the drugs within platelets and mast cells. Furthermore, the single cell capacity of microfluidics discussed in Chapter 1 can be used to explore platelet and mast cell secretion profile. Lastly, it would be exciting to use of field effect transistors (FETs) discussed in Chapter 1 to study the release of PF4 from platelets that is known for initiating response toward parasite-infected red blood cells and parasites elimination. Additionally, FET can also be modified to detect the release of Flt3L, a soluble cytokine, from mast cells that is known in initiating the immune system toward parasites eradication. A comparison of the platelet and mast cell degranulation using PF4 and Flt3L, respectively, to the dataset obtained in Chapters 2-3 would help to understand whether the secreted contents from platelets and mast cells were selective or non-selective, which is not fully understood to date.

Bibliography

Chapter 1

1. Galler, K.; Bräutigam, K.; Große, C.; Popp, J.; Neugebauer, U., Making a big thing of a small cell–recent advances in single cell analysis. *Analyst* **2014,** *139* (6), 1237-1273.
2. Trouillon, R.; Passarelli, M.; Wang, J.; Kurczy, M. E.; Ewing, A. G., Chemical Analysis of Single Cells. *Anal. Chem.* **2013,** *85*, 522-542.
3. Hwang, B.; Lee, J. H.; Bang, D., Single-cell RNA sequencing technologies and bioinformatics pipelines. *Exp. Mol. Med.* **2018,** *50* (8), 96.
4. Gawad, C.; Koh, W.; Quake, S. R., Single-cell genome sequencing: current state of the science. *Nat. Rev. Genet.* **2016,** *17* (3), 175.
5. Heath, J. R.; Ribas, A.; Mischel, P. S., Single-cell analysis tools for drug discovery and development. *Nat. Rev. Drug Discov.* **2016,** *15* (3), 204.
6. Lippincott-Schwartz, J., Profile of Eric Betzig, Stefan Hell, and WE Moerner, 2014 Nobel Laureates in Chemistry. *Proc. Natl. Acad. Sci.* **2015,** *112* (9), 2630-2632.
7. Schermelleh, L.; Heintzmann, R.; Leonhardt, H., A guide to super-resolution fluorescence microscopy. *J. Cell Biol.* **2010,** *190* (2), 165-175.
8. Guerra, J. M., Super-resolution through illumination by diffraction-born evanescent waves. *Appl. Phys. Lett.* **1995,** *66* (26), 3555-3557.
9. Hirano, Y.; Matsuda, A.; Hiraoka, Y., Recent advancements in structured-illumination microscopy toward live-cell imaging. *Microscopy* **2015,** *64* (4), 237-249.
10. Jost, A.; Heintzmann, R., Superresolution multidimensional imaging with structured illumination microscopy. *Annu. Rev. Mater. Res.* **2013,** *43*, 261-282.
11. Guo, Y.; Li, D.; Zhang, S.; Yang, Y.; Liu, J.-J.; Wang, X.; Liu, C.; Milkie, D. E.; Moore, R. P.; Tulu, U. S., Visualizing Intracellular Organelle and Cytoskeletal Interactions at Nanoscale Resolution on Millisecond Timescales. *Cell* **2018,** *175* (5), 1430-1442. e17.
12. Li, D.; Shao, L.; Chen, B.-C.; Zhang, X.; Zhang, M.; Moses, B.; Milkie, D. E.; Beach, J. R.; Hammer, J. A.; Pasham, M.; Kirchhausen, T.; Baird, M. A.; Davidson, M. W.; Xu, P.; Betzig, E., Extended-resolution structured illumination imaging of endocytic and cytoskeletal dynamics. *Science* **2015,** *349* (6251).
13. Heintzmann, R.; Huser, T., Super-resolution structured illumination microscopy. *Chem. Rev.* **2017,** *117* (23), 13890-13908.
14. Kraus, F.; Miron, E.; Demmerle, J.; Chitiashvili, T.; Budco, A.; Alle, Q.; Matsuda, A.; Leonhardt, H.; Schermelleh, L.; Markaki, Y., Quantitative 3D structured illumination microscopy of nuclear structures. *Nat. Protoc.* **2017,** *12* (5), 1011.
15. Banerjee, M.; Joshi, S.; Zhang, J.; Moncman, C. L.; Yadav, S.; Bouchard, B. A.; Storrie, B.; Whiteheart, S. W., Cellubrevin/Vesicle-Associated Membrane Protein-3 (VAMP-3)-mediated endocytosis and trafficking regulate platelet functions. **2017.**
16. Hell, S. W.; Wichmann, J., Breaking the diffraction resolution limit by stimulated emission: stimulated-emission-depletion fluorescence microscopy. *Opt. Lett.* **1994,** *19* (11), 780-782.
17. Kamper, M.; Ta, H.; Jensen, N. A.; Hell, S. W.; Jakobs, S., Near-infrared STED nanoscopy with an engineered bacterial phytochrome. *Nat. Commun.* **2018,** *9* (1), 4762.

18.	Honigmann, A.; Mueller, V.; Ta, H.; Schoenle, A.; Sezgin, E.; Hell, S. W.; Eggeling, C., Scanning STED-FCS reveals spatiotemporal heterogeneity of lipid interaction in the plasma membrane of living cells. *Nat Commun* **2014,** *5*.

19.	Betzig, E.; Patterson, G. H.; Sougrat, R.; Lindwasser, O. W.; Olenych, S.; Bonifacino, J. S.; Davidson, M. W.; Lippincott-Schwartz, J.; Hess, H. F., Imaging intracellular fluorescent proteins at nanometer resolution. *Science* **2006,** *313* (5793), 1642-1645.

20.	Rust, M. J.; Bates, M.; Zhuang, X., Sub-diffraction-limit imaging by stochastic optical reconstruction microscopy (STORM). *Nat. Methods* **2006,** *3* (10), 793.

21.	Hess, S. T.; Girirajan, T. P.; Mason, M. D., Ultra-high resolution imaging by fluorescence photoactivation localization microscopy. *Biophys. J.* **2006,** *91* (11), 4258-4272.

22.	Henriques, R.; Griffiths, C.; Hesper Rego, E.; Mhlanga, M. M., PALM and STORM: Unlocking live-cell super-resolution. *Biopolymers* **2011,** *95* (5), 322-331.

23.	Klein, T.; Proppert, S.; Sauer, M., Eight years of single-molecule localization microscopy. *Histochem. Cell Biol.* **2014,** *141* (6), 561-575.

24.	Puchner, E. M.; Walter, J. M.; Kasper, R.; Huang, B.; Lim, W. A., Counting molecules in single organelles with superresolution microscopy allows tracking of the endosome maturation trajectory. *Proc. Natl. Acad. Sci.* **2013,** *110* (40), 16015-16020.

25.	Xu, K.; Zhong, G.; Zhuang, X., Actin, spectrin, and associated proteins form a periodic cytoskeletal structure in axons. *Science* **2013,** *339* (6118), 452-456.

26.	Han, B.; Zhou, R.; Xia, C.; Zhuang, X., Structural organization of the actin-spectrin–based membrane skeleton in dendrites and soma of neurons. *Proc. Natl. Acad. Sci.* **2017,** *114* (32), E6678-E6685.

27.	Sigal, Y. M.; Speer, C. M.; Babcock, H. P.; Zhuang, X., Mapping synaptic input fields of neurons with super-resolution imaging. *Cell* **2015,** *163* (2), 493-505.

28.	Spahn, C.; Cella-Zannacchi, F.; Endesfelder, U.; Heilemann, M., Correlative super-resolution imaging of RNA polymerase distribution and dynamics, bacterial membrane and chromosomal structure in Escherichia coli. *Methods Appl. Fluoresc.* **2015,** *3* (1), 014005.

29.	Maker, P.; Terhune, R., Study of optical effects due to an induced polarization third order in the electric field strength. *Physical Review* **1965,** *137* (3A), A801.

30.	Begley, R.; Harvey, A.; Byer, R. L., Coherent anti-Stokes Raman spectroscopy. *Appl. Phys. Lett.* **1974,** *25* (7), 387-390.

31.	Tolles, W. M.; Nibler, J. W.; McDonald, J. R.; Harvey, A. B., A Review of the Theory and Application of Coherent Anti-Stokes Raman Spectroscopy (CARS). *Appl. Spectrosc.* **1977,** *31* (4), 253-271.

32.	Zumbusch, A.; Holtom, G. R.; Xie, X. S., Three-dimensional vibrational imaging by coherent anti-Stokes Raman scattering. *Phys. Rev. Lett.* **1999,** *82* (20), 4142.

33.	Potcoava, M. C.; Futia, G. L.; Aughenbaugh, J.; Schlaepfer, I. R.; Gibson, E. A., Raman and coherent anti-Stokes Raman scattering microscopy studies of changes in lipid content and composition in hormone-treated breast and prostate cancer cells. *J. Biomed. Opt.* **2014,** *19* (11), 111605-111605.

34.	Masia, F.; Pope, I.; Watson, P.; Langbein, W.; Borri, P., Bessel-beam hyperspectral CARS microscopy with sparse sampling: Enabling high-content high-throughput label-free quantitative chemical imaging. *Anal. Chem.* **2018,** *90* (6), 3775-3785.

35.	Karuna, A.; Masia, F.; Wiltshire, M.; Errington, R. J.; Borri, P.; Langbein, W., Label-free volumetric quantitative imaging of the human somatic cell division by hyperspectral coherent anti-Stokes Raman scattering. *Anal. Chem.* **2019**.

36. Eckhardt, G.; Hellwarth, R.; McClung, F.; Schwarz, S.; Weiner, D.; Woodbury, E., Stimulated Raman scattering from organic liquids. *Phys. Rev. Lett.* **1962,** *9* (11), 455.

37. Woodbury, E.; Ng, W., Ruby laser operation in near IR. *Proceedings of the Institute of Radio Engineers* **1962,** *50* (11), 2367-&.

38. Zhang, D.; Wang, P.; Slipchenko, M. N.; Cheng, J.-X., Fast Vibrational Imaging of Single Cells and Tissues by Stimulated Raman Scattering Microscopy. *Acc. Chem. Res.* **2014,** *47* (8), 2282-2290.

39. Fu, D.; Yang, W.; Xie, X. S., Label-free imaging of neurotransmitter acetylcholine at neuromuscular junctions with stimulated Raman scattering. *J. Am. Chem. Soc.* **2016,** *139* (2), 583-586.

40. Ji, M.; Arbel, M.; Zhang, L.; Freudiger, C. W.; Hou, S. S.; Lin, D.; Yang, X.; Bacskai, B. J.; Xie, X. S., Label-free imaging of amyloid plaques in Alzheimer's disease with stimulated Raman scattering microscopy. *Sci. Adv.* **2018,** *4* (11), eaat7715.

41. Orringer, D. A.; Pandian, B.; Niknafs, Y. S.; Hollon, T. C.; Boyle, J.; Lewis, S.; Garrard, M.; Hervey-Jumper, S. L.; Garton, H. J.; Maher, C. O., Rapid intraoperative histology of unprocessed surgical specimens via fibre-laser-based stimulated Raman scattering microscopy. *Nat. Biomed. Eng.* **2017,** *1* (2), 0027.

42. Actis, P.; Tokar, S.; Clausmeyer, J.; Babakinejad, B.; Mikhaleva, S.; Cornut, R.; Takahashi, Y.; López Córdoba, A.; Novak, P.; Shevchuck, A. I.; Dougan, J. A.; Kazarian, S. G.; Gorelkin, P. V.; Erofeev, A. S.; Yaminsky, I. V.; Unwin, P. R.; Schuhmann, W.; Klenerman, D.; Rusakov, D. A.; Sviderskaya, E. V.; Korchev, Y. E., Electrochemical Nanoprobes for Single-Cell Analysis. *ACS Nano* **2014,** *8* (1), 875-884.

43. Sean, E. A.; Haim, H. B., Carbon nanoelectrodes for single-cell probing. *Nanotechnology* **2015,** *26* (18), 185101.

44. Ying, Y.-L.; Ding, Z.; Zhan, D.; Long, Y.-T., Advanced electroanalytical chemistry at nanoelectrodes. *Chem. sci.* **2017,** *8* (5), 3338-3348.

45. Leszczyszyn, D. J.; Jankowski, J. A.; Viveros, O. H.; Diliberto, E. J.; Near, J. A.; Wightman, R. M., Nicotinic receptor-mediated catecholamine secretion from individual chromaffin cells. Chemical evidence for exocytosis. *J. Biol. Chem.* **1990,** *265* (25), 14736-14737.

46. Uchiyama, Y.; Maxson, M. M.; Sawada, T.; Nakano, A.; Ewing, A. G., Phospholipid mediated plasticity in exocytosis observed in PC12 cells. *Brain. Res.* **2007,** *1151*, 46-54.

47. Ge, S.; Woo, E.; White, J. G.; Haynes, C. L., Electrochemical measurement of endogenous serotonin release from human blood platelets. *Anal. Chem.* **2011,** *83* (7), 2598-2604.

48. Marquis, B. J.; Haynes, C. L., The effects of co-culture of fibroblasts on mast cell exocytotic release characteristics as evaluated by carbon-fiber microelectrode amperometry. *Biophys. Chem.* **2008,** *137* (1), 63-69.

49. Koseoglu, S.; Love, S. A.; Haynes, C. L., Cholesterol effects on vesicle pools in chromaffin cells revealed by carbon-fiber microelectrode amperometry. *Anal. Bioanal. Chem.* **2011,** *400* (9), 2963.

50. Roberts, J. G.; Toups, J. V.; Eyualem, E.; McCarty, G. S.; Sombers, L. A., In situ electrode calibration strategy for voltammetric measurements in vivo. *Anal. Chem.* **2013,** *85* (23), 11568-11575.

51. Ge, S.; Wittenberg, N. J.; Haynes, C. L., Quantitative and real-time detection of secretion of chemical messengers from individual platelets. *Biochemistry* **2008,** *47* (27), 7020-7024.

52. Chen, T. K.; Luo, G.; Ewing, A. G., Amperometric monitoring of stimulated catecholamine release from rat pheochromocytoma (PC12) cells at the zeptomole level. *Anal. Chem.* **1994,** *66* (19), 3031-3035.

53. Cookson, E. A.; Conte, I. L.; Dempster, J.; Hannah, M. J.; Carter, T., Characterisation of Weibel- Palade body fusion by amperometry in endothelial cells reveals fusion pore dynamics and the effect of cholesterol on exocytosis. *J. Cell Sci.* **2013,** *126* (23), 5490-5499.

54. Pyakurel, P.; Champaloux, E.; Venton, B., Fast-Scan Cyclic Voltammetry (FSCV) Detection of Endogenous Octopamine in Drosophila melanogaster Ventral Nerve Cord. *ACS Chem. Neurosci.* **2016,** *7* (8), 1112-1119.

55. Adamah-Biassi, E.; Almonte, A. G.; Blagovechtchenski, E.; Grinevich, V. P.; Weiner, J.; Bonin, K.; Budygin, E., Real time adenosine fluctuations detected with fast-scan cyclic voltammetry in the rat striatum and motor cortex. *J. Neurosci. Methods* **2015,** *256*, 56-62.

56. Chang, S.; Kim, I.; Marsh, M. P.; Jang, D.; Hwang, S. C.; Van Gompel, J.; Goerss, S. J.; Kimble, C. J.; Bennet, K.; Garris, P. A.; Blaha, C. D.; Lee, K., Wireless Fast-Scan Cyclic Voltammetry to Monitor Adenosine in Patients With Essential Tremor During Deep Brain Stimulation. *Mayo Clin. Proc.* **2012,** *87* (8), 760-765.

57. Finkenstaedt-Quinn, S. F.; Gruba, S. M.; Haynes, C. L., Variations in fusion pore formation in cholesterol-treated platelets: biophysical journal. *Biophys. J.* **2016,** *110* (4), 922-929.

58. Kim, D.; Koseoglu, S.; Manning, B. M.; Meyer, A. F.; Haynes, C. L., Electroanalytical eavesdropping on single cell communication. *ACS Anal Chem* **2011,** *83* (19), 7242-7249.

59. Li, X.; Majdi, S.; Dunevall, J.; Fathali, H.; Ewing, A. G., Quantitative Measurement of Transmitters in Individual Vesicles in the Cytoplasm of Single Cells with Nanotip Electrodes. *Angew. Chem. Int. Ed. Engl.* **2015,** *54* (41), 11978-82.

60. Omiatek, D. M.; Dong, Y.; Heien, M. L.; Ewing, A. G., Only a Fraction of Quantal Content is Released During Exocytosis as Revealed by Electrochemical Cytometry of Secretory Vesicles. *ACS Chem. Neurosci.* **2010,** *1* (3), 234-245.

61. Mellander, L. J.; Trouillon, R.; Svensson, M. I.; Ewing, A. G., Amperometric post spike feet reveal most exocytosis is via extended kiss-and-run fusion. *Sci. Rep.* **2012,** *2* (907).

62. van Kempen, G. T.; vanderLeest, H. T.; van den Berg, R. J.; Eilers, P.; Westerink, R. H., Three distinct modes of exocytosis revealed by amperometry in neuroendocrine cells. *Biophys. J.* **2011,** *100* (4), 968-77.

63. Amatore, C.; Arbault, S.; Bonifas, I.; Guille, M., Quantitative investigations of amperometric spike feet suggest different controlling factors of the fusion pore in exocytosis at chromaffin cells. *Biophys. Chem.* **2009,** *143* (3), 124–131.

64. Manning, B. M.; Meyer, A. F.; Gruba, S. M.; Haynes, C. L., Single-cell analysis of mast cell degranulation induced by airway smooth muscle-secreted chemokines. *Biochim. Biophys. Acta* **2015,** *1850* (9), 1862-8.

65. Manning, B. M.; Hebbel, R. P.; Gupta, K.; Haynes, C. L., Carbon-fiber microelectrode amperometry reveals sickle cell-induced inflammation and chronic morphine effects on single mast cells. *ACS Chem. Biol.* **2012,** *7* (3), 543-51.

.

66. Zhang, X. W.; Qiu, Q. F.; Jiang, H.; Zhang, F. L.; Liu, Y. L.; Amatore, C.; Huang, W. H., Real-Time Intracellular Measurements of ROS and RNS in Living Cells with Single Core–Shell Nanowire Electrodes. *Angew. Chem.* **2017,** *129* (42), 13177-13180.

67. Nascimento, R. A. S.; Özel, R. E.; Mak, W. H.; Mulato, M.; Singaram, B.; Pourmand, N., Single Cell "Glucose Nanosensor" Verifies Elevated Glucose Levels in Individual Cancer Cells. *Nano Lett.* **2016,** *16* (2), 1194-1200.

68. Li, X.; Dunevall, J.; Ewing, A. G., Quantitative Chemical Measurements of Vesicular Transmitters with Electrochemical Cytometry. *Acc. Chem. Res.* **2016,** *49* (10), 2347-2354.

69. Dunevall, J.; Majdi, S.; Larsson, A.; Ewing, A., Vesicle impact electrochemical cytometry compared to amperometric exocytosis measurements. *Curr. Opin. Electrochem.* **2017,** *5* (1), 85-91.

70. Ye, D.; Gu, C.; Ewing, A., Using Single-Cell Amperometry and Intracellular Vesicle Impact Electrochemical Cytometry To Shed Light on the Biphasic Effects of Lidocaine on Exocytosis. *ACS Chem. Neurosci.* **2018,** *9* (12), 2941-2947.

71. Pan, R.; Xu, M.; Burgess, J. D.; Jiang, D.; Chen, H.-Y., Direct electrochemical observation of glucosidase activity in isolated single lysosomes from a living cell. *Proc. Natl. Acad. Sci.* **2018,** *115* (16), 4087-4092.

72. Edgar, L. J., Method and apparatus for controlling electric currents. Google Patents: 1930.

73. Heil, O., Improvements in or relating to electrical amplifiers and other control arrangements and devices. *British Patent* **1935,** *439* (457), 10-14.

74. Arns, R. G., The other transistor: early history of the metal-oxide semiconductor field-effect transistor. *Engineering Science & Education Journal* **1998,** *7* (5), 233-240.

75. Wang, C.-W.; Pan, C.-Y.; Wu, H.-c.; Shih, P.-Y.; Tsai, C.-C.; Liao, K.-T.; Lu, L.-L.; Hsieh, W.-H.; Chen, C.-D.; Chen, Y.-t., In situ detection of chromogranin A released from living neurons with a single walled carbon nanotube field effect transistor. *Small* **2007,** *3* (8), 1350-1355.

76. Tsai, C. C.; Yang, C. C.; Shih, P. Y.; Wu, C. S.; Chen, C. D.; Pan, C. Y.; Chen, Y. T., Exocytosis of a single bovine adrenal chromaffin cell: the electrical and morphological studies. *J. Phys. Chem. B* **2008,** *112* (30), 9165-73.

77. Qiu, Q. F.; Zhang, F. L.; Tang, Y.; Zhang, X. W.; Jiang, H.; Liu, Y. L.; Huang, W. H., Real-time Monitoring of Exocytotic Glutamate Release from Single Neuron by Amperometry at an Enzymatic Biosensor. *Electroanalysis* **2018,** *30* (6), 1054-1059.

78. Susloparova, A.; Koppenhofer, D.; Vu, X. T.; Weil, M.; Ingebrandt, S., Impedance spectroscopy with field-effect transistor arrays for the analysis of anti-cancer drug action on individual cells. *Biosens. Bioelectron.* **2013,** *40* (1), 50-6.

79. Koppenhofer, D.; Susloparova, A.; Docter, D.; Stauber, R. H.; Ingebrandt, S., Monitoring nanoparticle induced cell death in H441 cells using field-effect transistors. *Biosens. Bioelectron.* **2013,** *40* (1), 89-95.

80. Susloparova, A.; Koppenhofer, D.; Law, J. K.; Vu, X. T.; Ingebrandt, S., Electrical cell-substrate impedance sensing with field-effect transistors is able to unravel cellular adhesion and detachment processes on a single cell level. *Lab Chip* **2015,** *15* (3), 668-79.

81. Zhang, Y.; Clausmeyer, J.; Babakinejad, B.; Lopez Cordoba, A.; Ali, T.; Shevchuk, A.; Takahashi, Y.; Novak, P.; Edwards, C.; Lab, M.; Gopal, S.; Chiappini, C.; Anand, U.; Magnani, L.; Coombes, R. C.; Gorelik, J.; Matsue, T.; Schuhmann, W.; Klenerman, D.; Sviderskaya, E. V.; Korchev, Y., Spearhead Nanometric Field-Effect Transistor Sensors for Single-Cell Analysis. *ACS Nano* **2016,** *10* (3), 3214-21.

82. Neher, E.; Sakmann, B., Single-channel currents recorded from membrane of denervated frog muscle fibres. *Nature* **1976,** *260* (5554), 799.

83. Rituper, B.; Gucek, A.; Jorgacevski, J.; Flasker, A.; Kreft, M.; Zorec, R., High-resolution membrane capacitance measurements for the study of exocytosis and endocytosis. *Nat. Protoc.* **2013,** *8*, 1169-1183.

84. Homann, U.; Tester, M., Patch-clamp measurements of capacitance to study exocytosis and endocytosis. *Trends Plant Sci.* **1998,** *3* (3), 110-114.

85. Dernick, G.; Toledo, G. A. D.; Lindau, M., The Patch Amperometry Technique: Design of a Method to Study Exocytosis of Single Vesicles. In *Electrochemical Methods for Neuroscience*, Michael, A. C.; Borland, L. M., Eds. CRC Press/Taylor & Francis: Boca Raton FL, 2007.

86. Pan, N.; Rao, W.; Kothapalli, N. R.; Liu, R.; Burgett, A. W.; Yang, Z., The single-probe: a miniaturized multifunctional device for single cell mass spectrometry analysis. *Anal. Chem.* **2014,** *86* (19), 9376-9380.

87. Ong, T.-H.; Kissick, D. J.; Jansson, E. T.; Comi, T. J.; Romanova, E. V.; Rubakhin, S. S.; Sweedler, J. V., Classification of large cellular populations and discovery of rare cells using single cell matrix-assisted laser desorption/ionization time-of-flight mass spectrometry. *Anal. Chem.* **2015,** *87* (14), 7036-7042.

88. Beske, P. H.; Bradford, A. B.; Grynovicki, J. O.; Glotfelty, E. J.; Hoffman, K. M.; Hubbard, K. S.; Tuznik, K. M.; McNutt, P. M., Botulinum and tetanus neurotoxin-induced blockade of synaptic transmission in networked cultures of human and rodent neurons. *Toxicol. Sci.* **2015,** *149* (2), 503-515.

89. Bard, A. J.; Fan, F. R. F.; Kwak, J.; Lev, O., Scanning electrochemical microscopy. Introduction and principles. *Anal. Chem.* **1989,** *61* (2), 132-138.

90. Lee, C.; Kwak, J.; Bard, A. J., Application of scanning electrochemical microscopy to biological samples. *Proc. Natl. Acad. Sci.* **1990,** *87* (5), 1740-1743.

91. Scott, E. R.; White, H. S.; Phipps, J. B., Iontophoretic transport through porous membranes using scanning electrochemical microscopy: application to in vitro studies of ion fluxes through skin. *Anal. Chem.* **1993,** *65* (11), 1537-1545.

92. Macpherson, J. V.; Beeston, M. A.; Unwin, P. R.; Hughes, N. P.; Littlewood, D., Imaging the action of fluid flow blocking agents on dentinal surfaces using a scanning electrochemical microscope. *Langmuir* **1995,** *11* (10), 3959-3963.

93. Berger, C. E.; Rathod, H.; Gillespie, J. I.; Horrocks, B. R.; Datta, H. K., Scanning electrochemical microscopy at the surface of bone-resorbing osteoclasts: Evidence for steady-state disposal and intracellular functional compartmentalization of calcium. *J. Bone Miner. Res.* **2001,** *16* (11), 2092-2102.

94. Holt, K. B.; Bard, A. J., Interaction of silver (I) ions with the respiratory chain of Escherichia coli: an electrochemical and scanning electrochemical microscopy study of the antimicrobial mechanism of micromolar Ag+. *Biochemistry* **2005,** *44* (39), 13214-13223.

95. Yasukawa, T.; Kaya, T.; Matsue, T., Characterization and imaging of single cells with scanning electrochemical microscopy. *Electroanalysis: An International Journal Devoted to Fundamental and Practical Aspects of Electroanalysis* **2000,** *12* (9), 653-659.

96. Hansma, P.; Drake, B.; Marti, O.; Gould, S.; Prater, C., The scanning ion-conductance microscope. *Science* **1989,** *243* (4891), 641-643.

97. Mann, S.; Hoffmann, G.; Hengstenberg, A.; Schuhmann, W.; Dietzel, I., Pulse-mode scanning ion conductance microscopy—a method to investigate cultured hippocampal cells. *J. Neurosci. Methods* **2002,** *116* (2), 113-117.

98. Novak, P.; Li, C.; Shevchuk, A. I.; Stepanyan, R.; Caldwell, M.; Hughes, S.; Smart, T. G.; Gorelik, J.; Ostanin, V. P.; Lab, M. J., Nanoscale live-cell imaging using hopping probe ion conductance microscopy. *Nat. Methods* **2009,** *6* (4), 279.

99. Takahashi, Y.; Murakami, Y.; Nagamine, K.; Shiku, H.; Aoyagi, S.; Yasukawa, T.; Kanzaki, M.; Matsue, T., Topographic imaging of convoluted surface of live cells by scanning ion conductance microscopy in a standing approach mode. *PCCP* **2010,** *12* (34), 10012-10017.

100. Korchev, Y. E.; Bashford, C. L.; Milovanovic, M.; Vodyanoy, I.; Lab, M. J., Scanning ion conductance microscopy of living cells. *Biophys. J.* **1997,** *73* (2), 653-658.

101. Shevchuk, A. I.; Gorelik, J.; Harding, S. E.; Lab, M. J.; Klenerman, D.; Korchev, Y. E., Simultaneous measurement of Ca2+ and cellular dynamics: combined scanning ion conductance and optical microscopy to study contracting cardiac myocytes. *Biophys. J.* **2001,** *81* (3), 1759-1764.

102. Polcari, D.; Hernández-Castro, J. A.; Li, K.; Geissler, M.; Mauzeroll, J., Determination of the Relationship between Expression and Functional Activity of Multidrug Resistance-Associated Protein 1 using Scanning Electrochemical Microscopy. *Anal. Chem.* **2017,** *89* (17), 8988-8994.

103. Santos, C. S.; Kowaltowski, A. J.; Bertotti, M., Single cell oxygen mapping (SCOM) by scanning electrochemical microscopy uncovers heterogeneous intracellular oxygen consumption. *Sci. Rep.* **2017,** *7* (1), 11428.

104. Şen, M.; Takahashi, Y.; Matsumae, Y.; Horiguchi, Y.; Kumatani, A.; Ino, K.; Shiku, H.; Matsue, T., Improving the Electrochemical Imaging Sensitivity of Scanning Electrochemical Microscopy-Scanning Ion Conductance Microscopy by Using Electrochemical Pt Deposition. *Anal. Chem.* **2015,** *87* (6), 3484-3489.

105. Page, A.; Kang, M.; Armitstead, A.; Perry, D.; Unwin, P. R., Quantitative Visualization of Molecular Delivery and Uptake at Living Cells with Self-Referencing Scanning Ion Conductance Microscopy-Scanning Electrochemical Microscopy. *Anal. Chem.* **2017,** *89* (5), 3021-3028.

106. Fenn, J. B.; Mann, M.; Meng, C. K.; Wong, S. F.; Whitehouse, C. M., Electrospray ionization for mass spectrometry of large biomolecules. *Science* **1989,** *246* (4926), 64-71.

107. Tanaka, K.; Waki, H.; Ido, Y.; Akita, S.; Yoshida, Y.; Yoshida, T.; Matsuo, T., Protein and polymer analyses up to m/z 100 000 by laser ionization time-of-flight mass spectrometry. *Rapid Commun. Mass Spectrom.* **1988,** *2* (8), 151-153.

108. Karas, M.; Bachmann, D.; Bahr, U.; Hillenkamp, F., Matrix-assisted ultraviolet laser desorption of non-volatile compounds. *Int. J. Mass Spectrom. Ion Processes* **1987,** *78*, 53-68.

109. Date, S.; Mizuno, H.; Tsuyama, N.; Harada, T.; Masujima, T., Direct drug metabolism monitoring in a live single hepatic cell by video mass spectrometry. *Anal. Sci.* **2012,** *28* (3), 201-201.

110. Masujima, T., Live single-cell mass spectrometry. *Anal. Sci.* **2009,** *25* (8), 953-960.

111. Küster, S. K.; Fagerer, S. R.; Verboket, P. E.; Eyer, K.; Jefimovs, K.; Zenobi, R.; Dittrich, P. S., Interfacing droplet microfluidics with matrix-assisted laser desorption/ionization mass spectrometry: label-free content analysis of single droplets. *Anal. Chem.* **2013,** *85* (3), 1285-1289.

112. Passarelli, M. K.; Winograd, N., Lipid imaging with time-of-flight secondary ion mass spectrometry (ToF-SIMS). *Biochim. Biophys. Acta* **2011,** *1811* (11), 976-90.

113. Zavalin, A.; Todd, E. M.; Rawhouser, P. D.; Yang, J.; Norris, J. L.; Caprioli, R. M., Direct imaging of single cells and tissue at sub-cellular spatial resolution using transmission geometry MALDI MS. *J. Mass Spectrom.* **2012,** *47* (11), 1473-81.

114. Lebedev, A. b. T., Ambient ionization mass spectrometry. *Russ. Chem. Rev.* **2015,** *84* (7), 665.

115. Feider, C. L.; Krieger, A. C.; Dehoog, R. J.; Eberlin, L. S., Ambient ionization mass spectrometry: recent developments and applications. *Anal. Chem.* **2019**.

116. Watrous, J. D.; Dorrestein, P. C., Imaging mass spectrometry in microbiology. *Nat. Rev. Microbiol.* **2011,** *9* (9), 683.

117. Castaing, R.; Slodzian, G. In *Microanalyse par émission ionique secondaire*, Proc. Eur. Reg. Conf. on Electron Microscopy, Delft, 1960; pp 169-72.

118. Passarelli, M. K.; Ewing, A. G., Single-cell imaging mass spectrometry. *Curr. Opin. Chem. Biol.* **2013,** *17* (5), 854-9.

119. Klitzing, H. A.; Weber, P. K.; Kraft, M. L., Secondary ion mass spectrometry imaging of biological membranes at high spatial resolution. *Methods Mol. Biol.* **2013,** *950*, 483-501.

120. Park, J.-W.; Jeong, H.; Kang, B.; Kim, S. J.; Park, S. Y.; Kang, S.; Kim, H. K.; Choi, J. S.; Hwang, D.; Lee, T. G., Multi-dimensional TOF-SIMS analysis for effective profiling of disease-related ions from the tissue surface. *Sci. Rep.* **2015,** *5*, 11077.

121. Bloom, A.; Winograd, N., Dye-enhanced imaging of mammalian cells with SIMS. *Surf. Interface Anal.* **2014,** *46* (S1), 177-180.

122. Bloom, A. N.; Tian, H.; Winograd, N., C60-SIMS imaging of nanoparticles within mammalian cells. *Biointerphases* **2016,** *11* (2), 02A306.

123. Karas, M.; Bachmann, D.; Hillenkamp, F., Influence of the wavelength in high-irradiance ultraviolet laser desorption mass spectrometry of organic molecules. *Anal. Chem.* **1985,** *57* (14), 2935-2939.

124. Hossen, M. A.; Nagata, Y.; Waki, M.; Ide, Y.; Takei, S.; Fukano, H.; Romero-Perez, G. A.; Tajima, S.; Yao, I.; Ohnishi, K., Decreased level of phosphatidylcholine (16: 0/20: 4) in multiple myeloma cells compared to plasma cells: a single-cell MALDI–IMS approach. *Anal. Bioanal. Chem.* **2015,** *407* (18), 5273-5280.

125. Krismer, J.; Tamminen, M.; Fontana, S.; Zenobi, R.; Narwani, A., Single-cell mass spectrometry reveals the importance of genetic diversity and plasticity for phenotypic variation in nitrogen-limited Chlamydomonas. *ISME J.* **2017,** *11* (4), 988.

126. Zavalin, A.; Yang, J.; Hayden, K.; Vestal, M.; Caprioli, R. M., Tissue protein imaging at 1 μm laser spot diameter for high spatial resolution and high imaging speed using transmission geometry MALDI TOF MS. *Anal. Bioanal. Chem.* **2015,** *407* (8), 2337-2342.

127. Kompauer, M.; Heiles, S.; Spengler, B., Atmospheric pressure MALDI mass spectrometry imaging of tissues and cells at 1.4-μm lateral resolution. *Nat. Methods* **2016,** *14* (1), 90.

128. Feenstra, A. D.; Dueñas, M. E.; Lee, Y. J., Five micron high resolution MALDI mass spectrometry imaging with simple, interchangeable, multi-resolution optical system. *J. Am. Soc. Mass. Spectrom.* **2017,** *28* (3), 434-442.

129. Bendall, S. C.; Nolan, G. P.; Roederer, M.; Chattopadhyay, P. K., A deep profiler's guide to cytometry. *Trends Immunol.* **2012,** *33* (7), 323-332.

130. Di Palma, S.; Bodenmiller, B., Unraveling cell populations in tumors by single-cell mass cytometry. *Curr. Opin. Biotechnol.* **2015,** *31*, 122-129.

131. Simoni, Y.; Chng, M. H. Y.; Li, S.; Fehlings, M.; Newell, E. W., Mass cytometry: a powerful tool for dissecting the immune landscape. *Curr. Opin. Immunol.* **2018,** *51*, 187-196.

132. Lombard-Banek, C.; Moody, S. A.; Nemes, P., Single-cell mass spectrometry for discovery proteomics: Quantifying translational cell heterogeneity in the 16-cell frog (Xenopus) embryo. *Angew. Chem. Int. Ed.* **2016,** *55* (7), 2454-2458.

133. Gaudillière, B.; Ganio, E. A.; Tingle, M.; Lancero, H. L.; Fragiadakis, G. K.; Baca, Q. J.; Aghaeepour, N.; Wong, R. J.; Quaintance, C.; El-Sayed, Y. Y., Implementing mass cytometry at the bedside to study the immunological basis of human

diseases: distinctive immune features in patients with a history of term or preterm birth. *Cytometry Part A* **2015,** *87* (9), 817-829.

134. Hoshino, K.; Huang, Y.-Y.; Lane, N.; Huebschman, M.; Uhr, J. W.; Frenkel, E. P.;Zhang, X., Microchip-based immunomagnetic detection of circulating tumor cells. *Lab Chip* **2011,** *11* (20), 3449-3457.

135. Kang, J. H.; Krause, S.; Tobin, H.; Mammoto, A.; Kanapathipillai, M.; Ingber, D. E., A combined micromagnetic-microfluidic device for rapid capture and culture of rare circulating tumor cells. *Lab Chip* **2012,** *12* (12), 2175-2181.

136. Wang, C.; Ye, M.; Cheng, L.; Li, R.; Zhu, W.; Shi, Z.; Fan, C.; He, J.; Liu, J.; Liu, Z., Simultaneous isolation and detection of circulating tumor cells with a microfluidic silicon-nanowire-array integrated with magnetic upconversion nanoprobes. *Biomaterials* **2015,** *54*, 55-62.

137. Wu, W.-T.; Martin, A. B.; Gandini, A.; Aubry, N.; Massoudi, M.; Antaki, J. F., Design of microfluidic channels for magnetic separation of malaria-infected red blood cells. *Microfluid. Nanofluid.* **2016,** *20* (2), 41.

138. Sofla, A.; Cirkovic, B.; Hsieh, A.; Miklas, J. W.; Filipovic, N.; Radisic, M., Enrichment of live unlabelled cardiomyocytes from heterogeneous cell populations using manipulation of cell settling velocity by magnetic field. *Biomicrofluidics* **2013,** *7* (1), 014110.

139. Liberale, C.; Cojoc, G.; Bragheri, F.; Minzioni, P.; Perozziello, G.; La Rocca, R.; Ferrara, L.; Rajamanickam, V.; Di Fabrizio, E.; Cristiani, I., Integrated microfluidic device for single-cell trapping and spectroscopy. *Scientific Reports* **2013,** *3*, 1258.

140. Chen, Y.; Wu, T.-H.; Kung, Y.-C.; Teitell, M. A.; Chiou, P.-Y., 3D pulsed laser-triggered high-speed microfluidic fluorescence-activated cell sorter. *Analyst* **2013,** *138* (24), 7308-7315.

141. Di Carlo, D.; Wu, L. Y.; Lee, L. P., Dynamic single cell culture array. *Lab Chip* **2006,** *6* (11), 1445-1449.

142. Lin, L.; Chu, Y.-S.; Thiery, J. P.; Lim, C. T.; Rodriguez, I., Microfluidic cell trap array for controlled positioning of single cells on adhesive micropatterns. *Lab Chip* **2013,** *13* (4), 714-721.

143. Wang, Y.; Tang, X.; Feng, X.; Liu, C.; Chen, P.; Chen, D.; Liu, B.-F., A microfluidic digital single-cell assay for the evaluation of anticancer drugs. *Anal. Bioanal. Chem.* **2015,** *407* (4), 1139-1148.

144. Wang, L.; Flanagan, L. A.; Jeon, N. L.; Monuki, E.; Lee, A. P., Dielectrophoresis switching with vertical sidewall electrodes for microfluidic flow cytometry. *Lab Chip* **2007,** *7* (9), 1114-1120.

145. Moon, H.-S.; Kwon, K.; Kim, S.-I.; Han, H.; Sohn, J.; Lee, S.; Jung, H.-I., Continuous separation of breast cancer cells from blood samples using multi-orifice flow fractionation (MOFF) and dielectrophoresis (DEP). *Lab Chip* **2011,** *11* (6), 1118-1125.

146. Agresti, J. J.; Antipov, E.; Abate, A. R.; Ahn, K.; Rowat, A. C.; Baret, J.-C.; Marquez, M.; Klibanov, A. M.; Griffiths, A. D.; Weitz, D. A., Ultrahigh-throughput screening in drop-based microfluidics for directed evolution. *Proc. Natl. Acad. Sci.* **2010,** *107* (9), 4004-4009.

147. Wang, X.; Chen, S.; Kong, M.; Wang, Z.; Costa, K. D.; Li, R. A.; Sun, D., Enhanced cell sorting and manipulation with combined optical tweezer and microfluidic chip technologies. *Lab Chip* **2011,** *11* (21), 3656-3662.

148. Ding, X.; Lin, S.-C. S.; Lapsley, M. I.; Li, S.; Guo, X.; Chan, C. Y.; Chiang, I.-K.; Wang, L.; McCoy, J. P.; Huang, T. J., Standing surface acoustic wave (SSAW) based multichannel cell sorting. *Lab Chip* **2012,** *12* (21), 4228-4231.

149. Zinchenko, A.; Devenish, S. R.; Kintses, B.; Colin, P.-Y.; Fischlechner, M.; Hollfelder, F., One in a million: flow cytometric sorting of single cell-lysate assays in monodisperse picolitre double emulsion droplets for directed evolution. *Anal. Chem.* **2014,** *86* (5), 2526-2533.
150. Warkiani, M. E.; Guan, G.; Luan, K. B.; Lee, W. C.; Bhagat, A. A. S.; Chaudhuri, P. K.; Tan, D. S.-W.; Lim, W. T.; Lee, S. C.; Chen, P. C., Slanted spiral microfluidics for the ultra-fast, label-free isolation of circulating tumor cells. *Lab Chip* **2014,** *14* (1), 128-137.
151. Shields IV, C. W.; Reyes, C. D.; López, G. P., Microfluidic cell sorting: a review of the advances in the separation of cells from debulking to rare cell isolation. *Lab Chip* **2015,** *15* (5), 1230-1249.
152. Hosic, S.; Murthy, S. K.; Koppes, A. N., Microfluidic sample preparation for single cell analysis. *Anal. Chem.* **2015,** *88* (1), 354-380.
153. Zaretsky, I.; Polonsky, M.; Shifrut, E.; Reich-Zeliger, S.; Antebi, Y.; Aidelberg, G.; Waysbort, N.; Friedman, N., Monitoring the dynamics of primary T cell activation and differentiation using long term live cell imaging in microwell arrays. *Lab Chip* **2012,** *12* (23), 5007-5015.
154. Deng, Y.; Zhang, Y.; Sun, S.; Wang, Z.; Wang, M.; Yu, B.; Czajkowsky, D. M.; Liu, B.; Li, Y.; Wei, W., An integrated microfluidic chip system for single-cell secretion profiling of rare circulating tumor cells. *Sci. Rep.* **2014,** *4*, 7499.
155. Ridley, A. J.; Schwartz, M. A.; Burridge, K.; Firtel, R. A.; Ginsberg, M. H.; Borisy, G.; Parsons, J. T.; Horwitz, A. R., Cell Migration: Integrating Signals from Front to Back. *Science* **2003,** *302* (5651), 1704-1709.
156. Kim, D.; Haynes, C. L., Neutrophil Chemotaxis within a Competing Gradient of Chemoattractants. *Analytical Chemistry* **2012,** *84* (14), 6070-6078.
157. Kim, D.; Haynes, C. L., On-Chip Evaluation of Neutrophil Activation and Neutrophil–Endothelial Cell Interaction during Neutrophil Chemotaxis. *Anal. Chem.* **2013,** *85* (22), 10787-10796.
158. Wu, X.; Kim, D.; Young, A. T.; Haynes, C. L., Exploring inflammatory disease drug effects on neutrophil function. *Analyst* **2014,** *139* (16), 4056-4063.
159. Nguyen, T. A.; Yin, T.-I.; Reyes, D.; Urban, G. A., Microfluidic chip with integrated electrical cell-impedance sensing for monitoring single cancer cell migration in three-dimensional matrixes. *Anal. Chem.* **2013,** *85* (22), 11068-11076.
160. Sarkar, S.; Cohen, N.; Sabhachandani, P.; Konry, T., Phenotypic drug profiling in droplet microfluidics for better targeting of drug-resistant tumors. *Lab Chip* **2015,** *15* (23), 4441-4450.
161. Chen, Q.; Wu, J.; Zhang, Y.; Lin, J.-M., Qualitative and quantitative analysis of tumor cell metabolism via stable isotope labeling assisted microfluidic chip electrospray ionization mass spectrometry. *Anal. Chem.* **2012,** *84* (3), 1695-1701.
162. Moon, H.-S.; Je, K.; Min, J.-W.; Park, D.; Han, K.-Y.; Shin, S.-H.; Park, W.-Y.; Yoo, C. E.; Kim, S.-H., Inertial-ordering-assisted droplet microfluidics for high-throughput single-cell RNA-sequencing. *Lab Chip* **2018,** *18* (5), 775-784.
163. Guo, S.; Lin, W. N.; Hu, Y.; Sun, G.; Phan, D.-T.; Chen, C.-H., Ultrahigh-throughput droplet microfluidic device for single-cell miRNA detection with isothermal amplification. *Lab Chip* **2018,** *18* (13), 1914-1920.
164. Hosokawa, M.; Nishikawa, Y.; Kogawa, M.; Takeyama, H., Massively parallel whole genome amplification for single-cell sequencing using droplet microfluidics. *Sci. Rep.* **2017,** *7* (1), 5199.
165. Marie, R.; Pødenphant, M.; Koprowska, K.; Bærlocher, L.; Vulders, R. C.; Wilding, J.; Ashley, N.; McGowan, S. J.; van Strijp, D.; van Hemert, F., Sequencing of

human genomes extracted from single cancer cells isolated in a valveless microfluidic device. *Lab Chip* **2018,** *18* (13), 1891-1902.

166. Huang, F.; Hartwich, T. M.; Rivera-Molina, F. E.; Lin, Y.; Duim, W. C.; Long, J. J.; Uchil, P. D.; Myers, J. R.; Baird, M. A.; Mothes, W., Video-rate nanoscopy using sCMOS camera–specific single-molecule localization algorithms. *Nat. Methods* **2013,** *10* (7), 653.

167. Xu, K.; Babcock, H. P.; Zhuang, X., Dual-objective STORM reveals three-dimensional filament organization in the actin cytoskeleton. *Nat. Methods* **2012,** *9* (2), 185.

168. Chen, B.-C.; Legant, W. R.; Wang, K.; Shao, L.; Milkie, D. E.; Davidson, M. W.; Janetopoulos, C.; Wu, X. S.; Hammer, J. A.; Liu, Z., Lattice light-sheet microscopy: imaging molecules to embryos at high spatiotemporal resolution. *Science* **2014,** *346* (6208), 1257998.

169. Lee, M. K.; Rai, P.; Williams, J.; Twieg, R. J.; Moerner, W. E., Small-molecule labeling of live cell surfaces for three-dimensional super-resolution microscopy. *J. Am. Chem. Soc.* **2014,** *136* (40), 14003-14006.

170. Ries, J.; Kaplan, C.; Platonova, E.; Eghlidi, H.; Ewers, H., A simple, versatile method for GFP-based super-resolution microscopy via nanobodies. *Nat. Methods* **2012,** *9* (6), 582.

171. Zanella, R.; Boccacci, P.; Zanni, L.; Bertero, M., Efficient gradient projection methods for edge-preserving removal of Poisson noise. *Inverse Problems* **2009,** *25* (4), 045010.

172. Levet, F.; Hosy, E.; Kechkar, A.; Butler, C.; Beghin, A.; Choquet, D.; Sibarita, J.-B., SR-Tesseler: a method to segment and quantify localization-based super-resolution microscopy data. *Nat. Methods* **2015,** *12* (11), 1065.
174. Lukinavičius, G. v.; Reymond, L.; Umezawa, K.; Sallin, O.; D'Este, E.; Göttfert, F.; Ta, H.; Hell, S. W.; Urano, Y.; Johnsson, K., Fluorogenic probes for multicolor imaging in living cells. *J. Am. Chem. Soc.* **2016,** *138* (30), 9365-9368.

173. Lukinavičius, G. v.; Reymond, L.; Umezawa, K.; Sallin, O.; D'Este, E.; Göttfert, F.; Ta, H.; Hell, S. W.; Urano, Y.; Johnsson, K., Fluorogenic probes for multicolor imaging in living cells. *J. Am. Chem. Soc.* **2016,** *138* (30), 9365-9368.

174. Jin, D.; Xi, P.; Wang, B.; Zhang, L.; Enderlein, J.; van Oijen, A. M., Nanoparticles for super-resolution microscopy and single-molecule tracking. *Nat. Methods* **2018**, 1.

175. He, H.; Liu, X.; Li, S.; Wang, X.; Wang, Q.; Li, J.; Wang, J.; Ren, H.; Ge, B.; Wang, S., High-density super-resolution localization imaging with blinking carbon dots. *Anal. Chem.* **2017,** *89* (21), 11831-11838.

176. Qin, P.; Parlak, M.; Kuscu, C.; Bandaria, J.; Mir, M.; Szlachta, K.; Singh, R.; Darzacq, X.; Yildiz, A.; Adli, M., Live cell imaging of low-and non-repetitive chromosome loci using CRISPR-Cas9. *Nat. Commun.* **2017,** *8*, 14725.

177. Morisaki, T.; Lyon, K.; DeLuca, K. F.; DeLuca, J. G.; English, B. P.; Zhang, Z.; Lavis, L. D.; Grimm, J. B.; Viswanathan, S.; Looger, L. L., Real-time quantification of single RNA translation dynamics in living cells. *Science* **2016,** *352* (6292), 1425-1429.

178. Freudiger, C. W.; Yang, W.; Holtom, G. R.; Peyghambarian, N.; Xie, X. S.; Kieu, K. Q., Stimulated Raman scattering microscopy with a robust fibre laser source. *Nat. Photonics* **2014,** *8* (2), 153.

179. Wei, L.; Yu, Y.; Shen, Y.; Wang, M. C.; Min, W., Vibrational imaging of newly synthesized proteins in live cells by stimulated Raman scattering microscopy. *Proc. Natl. Acad. Sci.* **2013,** *110* (28), 11226-11231.

180. Wei, L.; Hu, F.; Shen, Y.; Chen, Z.; Yu, Y.; Lin, C.-C.; Wang, M. C.; Min, W., Live-cell imaging of alkyne-tagged small biomolecules by stimulated Raman scattering. *Nat. Methods* **2014,** *11* (4), 410.

181. Al Jord, A.; Lemaître, A.-I.; Delgehyr, N.; Faucourt, M.; Spassky, N.; Meunier, A., Centriole amplification by mother and daughter centrioles differs in multiciliated cells. *Nature* **2014,** *516* (7529), 104.

182. Paez-Segala, M. G.; Sun, M. G.; Shtengel, G.; Viswanathan, S.; Baird, M. A.; Macklin, J. J.; Patel, R.; Allen, J. R.; Howe, E. S.; Piszczek, G., Fixation-resistant photoactivatable fluorescent proteins for CLEM. *Nat. Methods* **2015,** *12* (3), 215.

183. Odermatt, P. D.; Shivanandan, A.; Deschout, H.; Jankele, R.; Nievergelt, A. P.; Feletti, L.; Davidson, M. W.; Radenovic, A.; Fantner, G. E., High-resolution correlative microscopy: bridging the gap between single molecule localization microscopy and atomic force microscopy. *Nano Lett.* **2015,** *15* (8), 4896-4904.

184. Monserrate, A.; Casado, S.; Flors, C., Correlative Atomic Force Microscopy and Localization-Based Super-Resolution Microscopy: Revealing Labelling and Image Reconstruction Artefacts. *Chemphyschem* **2014,** *15* (4), 647-650.

185. Duim, W. C.; Chen, B.; Frydman, J.; Moerner, W., Sub-Diffraction Imaging of Huntingtin Protein Aggregates by Fluorescence Blink-Microscopy and Atomic Force Microscopy. *Chemphyschem* **2011,** *12* (13), 2387-2390.

186. Vangindertael, J.; Beets, I.; Rocha, S.; Dedecker, P.; Schoofs, L.; Vanhoorelbeke, K.; Hofkens, J.; Mizuno, H., Super-resolution mapping of glutamate receptors in C. elegans by confocal correlated PALM. *Sci. Rep.* **2015,** *5*, 13532.

187. Dudok, B.; Barna, L.; Ledri, M.; Szabó, S. I.; Szabadits, E.; Pintér, B.; Woodhams, S. G.; Henstridge, C. M.; Balla, G. Y.; Nyilas, R., Cell-specific STORM super-resolution imaging reveals nanoscale organization of cannabinoid signaling. *Nat. Neurosci.* **2015,** *18* (1), 75.

188. Barna, L.; Dudok, B.; Miczán, V.; Horváth, A.; László, Z. I.; Katona, I., Correlated confocal and super-resolution imaging by VividSTORM. *Nat. Protoc.* **2016,** *11* (1), 163.

189. Hamel, V.; Guichard, P.; Fournier, M.; Guiet, R.; Flückiger, I.; Seitz, A.; Gönczy, P., Correlative multicolor 3D SIM and STORM microscopy. *Biomed. Opt. Express* **2014,** *5* (10), 3326-3336.

190. Amos, A. N.; Roberts, J. G.; Qi, L.; Sombers, L. A.; McCarty, G. S., Reducing the sampling rate of biochemical measurements using fast-scan cyclic voltammetry for in vivo applications. *IEEE Sens. J.* **2014,** *14* (9), 2975-2980.

191. Kile, B. M.; Walsh, P. L.; McElligott, Z. A.; Bucher, E. S.; Guillot, T. S.; Salahpour, A.; Caron, M. G.; Wightman, R. M., Optimizing the temporal resolution of fast-scan cyclic voltammetry. *ACS Chem. Neurosci.* **2012,** *3* (4), 285-292.

192. Schmidt, A. C.; Dunaway, L. E.; Roberts, J. G.; McCarty, G. S.; Sombers, L. A., Multiple scan rate voltammetry for selective quantification of real-time enkephalin dynamics. *Anal. Chem.* **2014,** *86* (15), 7806-7812.

193. Tian, B.; Lieber, C. M., Synthetic nanoelectronic probes for biological cells and tissues. *Annu. Rev. Anal. Chem.* **2013,** *6*, 31-51.

194. Zhuang, L.; Zuo, H.; Wu, Z.; Wang, Y.; Fang, D.; Jiang, D., Enhanced Electrochemical Nanoring Electrode for Analysis of Cytosol in Single Cells. *Anal. Chem.* **2014,** *86* (23), 11517-11522.

195. Liu, Y.; Li, M.; Zhang, F.; Zhu, A.; Shi, G., Development of Au Disk Nanoelectrode Down to 3 nm in Radius for Detection of Dopamine Release from a Single Cell. *Anal. Chem.* **2015,** *87* (11), 5531-5538.

196. Yakushenko, A.; Kätelhön, E.; Wolfrum, B., Parallel On-Chip Analysis of Single Vesicle Neurotransmitter Release. *Anal. Chem.* **2013,** *85* (11), 5483-5490.

197. Huys, R.; Braeken, D.; Jans, D.; Stassen, A.; Collaert, N.; Wouters, J.; Loo, J.; Severi, S.; Vleugels, F.; Callewaert, G.; Verstreken, K.; Bartic, C.; Eberle, W., Single-cell recording and stimulation with a 16k micro-nail electrode array integrated on a 0.18 [small mu]m CMOS chip. *Lab Chip* **2012,** *12* (7), 1274-1280.

198. Sen, M.; Ino, K.; Shiku, H.; Matsue, T., Accumulation and detection of secreted proteins from single cells for reporter gene assays using a local redox cycling-based electrochemical (LRC-EC) chip device. *Lab Chip* **2012,** *12* (21), 4328-4335.

199. Kodandaramaiah, S. B.; Franzesi, G. T.; Chow, B. Y.; Boyden, E. S.; Forest, C. R., Automated whole-cell patch-clamp electrophysiology of neurons in vivo. *Nat. Methods* **2012,** *9* (6), 585.

200. Liu, G.; Ma, C.; Jin, B.-K.; Chen, Z.; Zhu, J.-J., Direct Electrochemiluminescence Imaging of a Single Cell on a Chitosan Film Modified Electrode. *Anal. Chem.* **2018,** *90* (7), 4801-4806.

201. Qiu, Y.; Zhou, B.; Yang, X.; Long, D.; Hao, Y.; Yang, P., Novel Single-Cell Analysis Platform Based on a Solid-State Zinc-Coadsorbed Carbon Quantum Dots Electrochemiluminescence Probe for the Evaluation of CD44 Expression on Breast Cancer Cells. *ACS Applied Materials & Interfaces* **2017,** *9* (20), 16848-16856.

202. Liu, X.; Savy, A.; Maurin, S.; Grimaud, L.; Darchen, F.; Quinton, D.; Labbé, E.; Buriez, O.; Delacotte, J.; Lemaître, F., A dual functional electroactive and fluorescent probe for coupled measurements of vesicular exocytosis with high spatial and temporal resolution. *Angew. Chem. Int. Ed.* **2017,** *56* (9), 2366-2370.

203. Huang, F.; Lin, M.; Duan, R.; Lou, X.; Xia, F.; Willner, I., Photoactivated Specific mRNA Detection in Single Living Cells by Coupling "Signal-on" Fluorescence and "Signal-off" Electrochemical Signals. *Nano Lett.* **2018,** *18* (8), 5116-5123.

204. Asakawa, D.; Hiraoka, K., Surface characterization and depth profiling of biological molecules by electrospray droplet impact/SIMS. *Surf. Interface Anal.* **2012,** *44* (2), 227-231.

205. Winograd, N., Imaging mass spectrometry on the nanoscale with cluster ion beams. *Anal. Chem.* **2014,** *87* (1), 328-333.

206. Barnes, C. A.; Brison, J.; Robinson, M.; Graham, D. J.; Castner, D. G.; Ratner, B. D., Identifying Individual Cell Types in Heterogeneous Cultures Using Secondary Ion Mass Spectrometry Imaging with C60 Etching and Multivariate Analysis. *Anal. Chem.* **2012,** *84* (2), 893-900.

207. Winograd, N., Gas cluster ion beams for secondary ion mass spectrometry. *Annu. Rev. Anal. Chem.* **2018,** *11*, 29-48.

208. Sheng, L.; Cai, L.; Wang, J.; Li, Z.; Mo, Y.; Zhang, S.; Xu, J.-J.; Zhang, X.; Chen, H.-Y., Simultaneous imaging of newly synthesized proteins and lipids in single cell by TOF-SIMS. *Int. J. Mass spectrom.* **2017,** *421*, 238-244.

209. Lanni, E. J.; Dunham, S. J.; Nemes, P.; Rubakhin, S. S.; Sweedler, J. V., Biomolecular imaging with a C60-SIMS/MALDI dual ion source hybrid mass spectrometer: instrumentation, matrix enhancement, and single cell analysis. *J. Am. Soc. Mass. Spectrom.* **2014,** *25* (11), 1897-1907.

210. He, C.; Hu, X.; Jung, R. S.; Weston, T. A.; Sandoval, N. P.; Tontonoz, P.; Kilburn, M. R.; Fong, L. G.; Young, S. G.; Jiang, H., High-resolution imaging and quantification of plasma membrane cholesterol by NanoSIMS. *Proc. Natl. Acad. Sci.* **2017,** *114* (8), 2000-2005.

211. Berthelot, H.; Duhamel, S.; L'Helguen, S.; Maguer, J.-F.; Wang, S.; Cetinić, I.; Cassar, N., NanoSIMS single cell analyses reveal the contrasting nitrogen sources for small phytoplankton. *ISME J.* **2018**, 1.

212. Kompauer, M.; Heiles, S.; Spengler, B., Autofocusing MALDI mass spectrometry imaging of tissue sections and 3D chemical topography of nonflat surfaces. *Nat. Methods* **2017,** *14* (12), 1156.

213. Passarelli, M. K.; Pirkl, A.; Moellers, R.; Grinfeld, D.; Kollmer, F.; Havelund, R.; Newman, C. F.; Marshall, P. S.; Arlinghaus, H.; Alexander, M. R., The 3D OrbiSIMS—label-free metabolic imaging with subcellular lateral resolution and high mass-resolving power. *Nat. Methods* **2017,** *14* (12), 1175.

214. Do, T. D.; Ellis, J. F.; Neumann, E. K.; Comi, T. J.; Tillmaand, E. G.; Lenhart, A. E.; Rubakhin, S. S.; Sweedler, J. V., Optically Guided Single Cell Mass Spectrometry of Rat Dorsal Root Ganglia to Profile Lipids, Peptides and Proteins. *Chemphyschem* **2018,** *19* (10), 1180-1191.

215. Comi, T. J.; Makurath, M. A.; Philip, M. C.; Rubakhin, S. S.; Sweedler, J. V., MALDI MS Guided Liquid Microjunction Extraction for Capillary Electrophoresis–Electrospray Ionization MS Analysis of Single Pancreatic Islet Cells. *Anal. Chem.* **2017,** *89* (14), 7765-7772.

216. Guillaume-Gentil, O.; Rey, T.; Kiefer, P.; Ibáñez, A. J.; Steinhoff, R.; Brönnimann, R.; Dorwling-Carter, L.; Zambelli, T.; Zenobi, R.; Vorholt, J. A., Single-Cell Mass Spectrometry of Metabolites Extracted from Live Cells by Fluidic Force Microscopy. *Anal. Chem.* **2017,** *89* (9), 5017-5023.

217. Steinhoff, R. F.; Karst, D. J.; Steinebach, F.; Kopp, M. R.; Schmidt, G. W.; Stettler, A.; Krismer, J.; Soos, M.; Pabst, M.; Hierlemann, A., Microarray-based MALDI-TOF mass spectrometry enables monitoring of monoclonal antibody production in batch and perfusion cell cultures. *Methods* **2016,** *104*, 33-40.

218. Xie, W.; Gao, D.; Jin, F.; Jiang, Y.; Liu, H., Study of phospholipids in single cells using an integrated microfluidic device combined with matrix-assisted laser desorption/ionization mass spectrometry. *Anal. Chem.* **2015,** *87* (14), 7052-7059.

219. Phelps, M. S.; Sturtevant, D.; Chapman, K. D.; Verbeck, G. F., Nanomanipulation-coupled matrix-assisted laser desorption/ionization-direct organelle mass Spectrometry: a technique for the detailed analysis of single organelles. *J. Am. Soc. Mass. Spectrom.* **2016,** *27* (2), 187-193.

220. Giesen, C.; Wang, H. A.; Schapiro, D.; Zivanovic, N.; Jacobs, A.; Hattendorf, B.; Schüffler, P. J.; Grolimund, D.; Buhmann, J. M.; Brandt, S., Highly multiplexed imaging of tumor tissues with subcellular resolution by mass cytometry. *Nat. Methods* **2014,** *11* (4), 417.

221. O'Brien, P. J.; Lee, M.; Spilker, M. E.; Zhang, C. C.; Yan, Z.; Nichols, T. C.; Li, W.; Johnson, C. H.; Patti, G. J.; Siuzdak, G., Monitoring metabolic responses to chemotherapy in single cells and tumors using nanostructure-initiator mass spectrometry (NIMS) imaging. *Cancer & Metabolism* **2013,** *1*, 4-4.

222. Nudnova, M. M.; Sigg, J.; Wallimann, P.; Zenobi, R., Plasma Ionization Source for Atmospheric Pressure Mass Spectrometry Imaging Using Near-Field Optical Laser Ablation. *Anal. Chem.* **2015,** *87* (2), 1323-1329.

223. Passarelli, M. K.; Newman, C. F.; Marshall, P. S.; West, A.; Gilmore, I. S.; Bunch, J.; Alexander, M. R.; Dollery, C. T., Single-Cell Analysis: Visualizing Pharmaceutical and Metabolite Uptake in Cells with Label-Free 3D Mass Spectrometry Imaging. *Anal. Chem.* **2015,** *87* (13), 6696-6702.

224. Kuznetsov, I.; Filevich, J.; Dong, F.; Woolston, M.; Chao, W.; Anderson, E. H.; Bernstein, E. R.; Crick, D. C.; Rocca, J. J.; Menoni, C. S., Three-dimensional nanoscale molecular imaging by extreme ultraviolet laser ablation mass spectrometry. *Nat Commun* **2015,** *6*.

225. O'Brien, P.; Lee, M.; Spilker, M.; Zhang, C.; Yan, Z.; Nichols, T.; Li, W.; Johnson, C.; Patti, G.; Siuzdak, G., Monitoring metabolic responses to chemotherapy in

single cells and tumors using nanostructure-initiator mass spectrometry (NIMS) imaging. *Cancer Metab.* **2013,** *1* (1), 1-14.

226. Hua, X.; Szymanski, C.; Wang, Z.; Zhou, Y.; Ma, X.; Yu, J.; Evans, J.; Orr, G.; Liu, S.; Zhu, Z., Chemical imaging of molecular changes in a hydrated single cell by dynamic secondary ion mass spectrometry and super-resolution microscopy. *Integr. Biol.* **2016,** *8* (5), 635-644.

227. Tarolli, J. G.; Jackson, L. M.; Winograd, N., Improving secondary ion mass spectrometry image quality with image fusion. *J. Am. Soc. Mass. Spectrom.* **2014,** *25* (12), 2154-2162.

228. Neupert, S.; Fusca, D.; Kloppenburg, P.; Predel, R., Analysis of Single Neurons by Perforated Patch Clamp Recordings and MALDI-TOF Mass Spectrometry. *ACS Chem. Neurosci.* **2018,** *9* (8), 2089-2096.

229. Li, Q.; Chen, P.; Fan, Y.; Wang, X.; Xu, K.; Li, L.; Tang, B., Multicolor Fluorescence Detection-Based Microfluidic Device for Single-Cell Metabolomics: Simultaneous Quantitation of Multiple Small Molecules in Primary Liver Cells. *Anal. Chem.* **2016,** *88* (17), 8610-8616.

230. Li, L.; Fan, Y.; Li, Q.; Sheng, R.; Si, H.; Fang, J.; Tong, L.; Tang, B., Simultaneous Single-Cell Analysis of Na+, K+, Ca2+, and Mg2+ in Neuron-Like PC-12 Cells in a Microfluidic System. *Anal. Chem.* **2017,** *89* (8), 4559-4565.

231. Altinagac, E.; Taskin, S.; Kizil, H., Single cell array impedance analysis in a microfluidic device. *JPCS* **2016,** *757*, 012010.

232. Lou, B.; Zhou, Z.; Gu, W.; Dong, S., Microelectrodes Integrated into a Microfluidic Chip for the Detection of CCRF-CEM Cells Based on the Electrochemical Oxidation of Hydrazine. *ChemElectroChem* **2016,** *3* (12), 2008-2011.

233. Yang, M.; Nelson, R.; Ros, A., Toward analysis of proteins in single cells: a quantitative approach employing isobaric tags with MALDI mass spectrometry realized with a microfluidic platform. *Anal. Chem.* **2016,** *88* (13), 6672-6679.

234. Yang, L.; Wang, Z.; Deng, Y.; Li, Y.; Wei, W.; Shi, Q., Single-Cell, Multiplexed Protein Detection of Rare Tumor Cells Based on a Beads-on-Barcode Antibody Microarray. *Anal. Chem.* **2016,** *88* (22), 11077-11083.

235. Chokkalingam, V.; Tel, J.; Wimmers, F.; Liu, X.; Semenov, S.; Thiele, J.; Figdor, C. G.; Huck, W. T., Probing cellular heterogeneity in cytokine-secreting immune cells using droplet-based microfluidics. *Lab Chip* **2013,** *13* (24), 4740-4744.

Chapter 2

1. Mace, K. E.; Arguin, P. M.; Tan, K. R., Malaria Surveillance—United States, 2015. *MMWR Surveill. Summ.* **2018,** *67* (7), 1-28.

2. This Year's World Malaria Report at a Glance. https://www.who.int/malaria/media/world-malaria-report-2018/en/ (accessed January 21, 2019).

3. Nadjm, B.; Behrens, R. H., Malaria: An update for physicians. *Infect. Dis. Clin.* **2012,** *26* (2), 243-259.

4. Tuteja, R., Malaria− an overview. *The FEBS journal* **2007,** *274* (18), 4670-4679.

5. Ridley, R. G., Medical need, scientific opportunity and the drive for antimalarial drugs. *Nature* **2002,** *415* (6872), 686.

6. Bloland, P. B., and World Health Organization. **2001** Drug Resistance in Malaria, World Health Organization.; pp 12-15.

7. Semple, J. W.; Italiano, J. E.; Freedman, J., Platelets and the immune continuum. *Nat. Rev. Immunol.* **2011,** *11* (4), 264.

8. McMorran, B. J.; Marshall, V. M.; de Graaf, C.; Drysdale, K. E.; Shabbar, M.; Smyth, G. K.; Corbin, J. E.; Alexander, W. S.; Foote, S. J., Platelets kill intraerythrocytic malarial parasites and mediate survival to infection. *Science* **2009,** *323* (5915), 797-800.

9. McMorran, B. J.; Wieczorski, L.; Drysdale, K. E.; Chan, J.-A.; Huang, H. M.; Smith, C.; Mitiku, C.; Beeson, J. G.; Burgio, G.; Foote, S. J., Platelet factor 4 and Duffy antigen required for platelet killing of Plasmodium falciparum. *Science* **2012,** *338* (6112), 1348-1351.

10. Peyron, F.; Polack, B.; Lamotte, D.; Kolodie, L.; Ambroise-Thomas, P., Plasmodium falciparum growth inhibition by human platelets in vitro. *Parasitology* **1989,** *99* (3), 317-   322.

11. Polack, B.; Delolme, F.; Peyron, F., Protective role of platelets in chronic (Balb/C) and acute (CBA/J) Plasmodium berghei murine malaria. *Pathophysiol. Haemost. Thromb.* **1997,** *27* (6), 278-285.

12. Kowalska, M. A.; Rauova, L.; Poncz, M., Role of the platelet chemokine platelet factor 4 (PF4) in hemostasis and thrombosis. *Thromb. Res.* **2010,** *125* (4), 292-296.

13. Kho, S.; Barber, B. E.; Johar, E.; Andries, B.; Poespoprodjo, J. R.; Kenangalem, E.; Piera, K. A.; Ehmann, A.; Price, R. N.; William, T., Platelets kill circulating parasites of all major Plasmodium species in human malaria. *Blood* **2018**, blood-2018-05-849307.

14. Grau, G. E.; Mackenzie, C. D.; Carr, R. A.; Redard, M.; Pizzolato, G.; Allasia, C.; Cataldo, C.; Taylor, T. E.; Molyneux, M. E., Platelet accumulation in brain microvessels in fatal pediatric cerebral malaria. *J. Infect. Dis.* **2003,** *187* (3), 461-466.

15. Gramaglia, I.; Velez, J.; Combes, V.; Grau, G. E.; Wree, M.; Van Der Heyde, H. C., Platelets activate a pathogenic response to blood-stage Plasmodium infection but not a protective immune response. *Blood* **2017**, blood-2016-08-733519.

16. Kim, D.; Koseoglu, S.; Manning, B. M.; Meyer, A. F.; Haynes, C. L., Electroanalytical eavesdropping on single cell communication. *Anal. Chem.* **2011,** *83* (19), 7242.

17. Ge, S.; Woo, E.; Haynes, Christy l., Quantal Regulation and Exocytosis of Platelet Dense-Body Granules. *Biophys. J.* **2011,** *101* (10), 2351-2359.

18. Ge, S.; Woo, E.; White, J. G.; Haynes, C. L., Electrochemical measurement of endogenous serotonin release from human blood platelets. *Anal. Chem.* **2011,** *83* (7), 2598-604.

19. Brass, L. F.; Newman, D. K.; Wannermacher, K. M.; Zhu, L.; Stalker, T. J., Signal transduction during platelet plug formation. In *Platelets (Third Edition)*, Elsevier: 2013; pp 367-398.

20. Huang, B. W.; Pearman, E.; Kim, C. C., Mouse models of uncomplicated and fatal malaria. *Bio-protocol* **2015,** *5* (13).

21. Kawagoe, K. T.; Zimmerman, J. B.; Wightman, R. M., Principles of voltammetry and microelectrode surface states. *J. Neurosci. Methods* **1993,** *48* (3), 225-240.

22. White, J. G., Electron microscopy methods for studying platelet structure and function. *Methods in molecular biology (Clifton, N.J.)* **2004,** *272*, 47-63.

23. Rendu, F.; Brohard-Bohn, B., The platelet release reaction: granules' constituents,   secretion and functions. *Platelets* **2001,** *12* (5), 261-273.

24. Mackman, N.; Gruber, A., Platelet polyphosphate: an endogenous activator of coagulation factor XII. *J. Thromb. Haemost.* **2010,** *8* (5), 865-867.

25. Podoba, J.; Stevenson, M., CD4+ and CD8+ T lymphocytes both contribute to acquired immunity to blood-stage Plasmodium chabaudi AS. *Infect. Immun.* **1991,** *59* (1), 51-58.

26. Artavanis-Tsakonas, K.; Tongren, J.; Riley, E., The war between the malaria parasite and the immune system: immunity, immunoregulation and immunopathology. *Clin. Exp. Immunol.* **2003,** *133* (2), 145-152.

Chapter 3

1. World Health Organization. 2019. World malaria report 2019. https://www.who.int/publications/i/item/world-malaria-report-2019 (accessed July 14, 2020)

2. Langhorne, J.; Buffet, P.; Galinski, M.; Good, M.; Harty, J.; Leroy, D.; Mota, M. M.; Pasini, E.; Renia, L.; Riley, E., The relevance of non-human primate and rodent malaria models for humans. *Malar. J.* **2011,** *10* (1), 1-4.

3. Stevenson, M. M.; Riley, E. M., Innate immunity to malaria. *Nat. Rev. Immunol.* **2004,** *4* (3), 169-180.

4. Mekori, Y. A.; Metcalfe, D. D., Mast cells in innate immunity. *Immunol. Rev.* **2000,** *173* (1), 131-140.

5. Lu, F.; Huang, S., The roles of mast cells in parasitic protozoan infections. *Front.Immunol.* **2017,** *8*, 363.

6. Marquis, B. J.; Haynes, C. L., The effects of co-culture of fibroblasts on mast cell exocytotic release characteristics as evaluated by carbon-fiber microelectrode amperometry. *Biophys. Chem.* **2008,** *137* (1), 63-69.

7. Manning, B. M.; Hebbel, R. P.; Gupta, K.; Haynes, C. L., Carbon-fiber microelectrode amperometry reveals sickle-cell-induced inflammation and chronic morphine effects on single mast cells. *ACS Chem. Biol.* **2012,** *7* (3), 543-551.

8. Manning, B. M.; Meyer, A. F.; Gruba, S. M.; Haynes, C. L., Single-cell analysis of mast cell degranulation induced by airway smooth muscle-secreted chemokines. *Biochim.Biophys. Acta* **2015,** *1850* (9), 1862-1868.

9. Manning, B. M.; Gruba, S. M.; Meyer, A. F.; Haynes, C. L., Neuropeptide-induced mast cell degranulation and characterization of signaling modulation in response to IgE conditioning. *ACS Chem. Biol.* **2016,** *11* (11), 3077-3083.

10. Kim, D.; Koseoglu, S.; Manning, B. M.; Meyer, A. F.; Haynes, C. L., Electroanalytical eavesdropping on single cell communication. *Anal. Chem* **2011**, 83 (19), 7242-7249.

11. Wernersson, S.; Pejler, G., Mast cell secretory granules: armed for battle. *Nature Rev. Immunol.* **2014,** *14* (7), 478-494.

12. Patzelt, J.; F Langer, H., Platelets in angiogenesis. *Curr. Vasc. Pharmacol.* **2012,** *10* (5), 489.

13. Huang, B. W.; Pearman, E.; Kim, C. C., Mouse models of uncomplicated and fatal malaria. *Bio-protocol* **2015,** *5* (13).

14. Kawagoe, K. T.; Zimmerman, J. B.; Wightman, R. M., Principles of voltammetry and microelectrode surface states. *J. Neurosci. Methods* **1993,** *48* (3), 225-240.

15. Gonon, F.; Fombarlet, C.; Buda, M.; Pujol, J. F., Electrochemical treatment of pyrolytic carbon fiber electrodes. *Anal. Chem.* **1981,** *53* (9), 1386-1389.

16. Xiong-Hang, K.; Kemnetz-Ness, K.; Krieger, A. C.; Haynes, C. L., Insight into the Effects of Plasmodium chabaudi on Platelets Using Carbon-Fiber Microelectrode Amperometry. *ACS Infect. Dis.* **2019,** *5* (4), 592-597.

17. Finkenstaedt-Quinn, S. A.; Gruba, S. M.; Haynes, C. L., Variations in fusion pore formation in cholesterol-treated platelets. *Biophys. J.* **2016,** *110* (4), 922-929.

18. Lorentz, A.; Baumann, A.; Vitte, J.; Blank, U., The SNARE machinery in mast cell secretion. *Front. Immunol.* **2012,** *3*, 143.
19. Reed, G. L., Platelet secretion. *Platelets* **2002,** *2*, 309-318.
20. Dvorak, A. M., Ultrastructural studies of human basophils and mast cells. *J. Histochem. Cytochem.* **2005,** *53* (9), 1043-1070.
21. Ponomareva, A.; Nevzorova, T.; Mordakhanova, E.; Andrianova, I.; Rauova, L.; Litvinov, R.; Weisel, J., Intracellular origin and ultrastructure of platelet-derived microparticles. *J. Thromb. Haemost.* **2017,** *15* (8), 1655-1667.
22. Kho, S.; Barber, B. E.; Johar, E.; Andries, B.; Poespoprodjo, J. R.; Kenangalem, E.; Piera, K. A.; Ehmann, A.; Price, R. N.; William, T., Platelets kill circulating parasites of all major Plasmodium species in human malaria. *Blood* **2018,** *132* (12), 1332-1344.
23. Love, M. S.; Millholland, M. G.; Mishra, S.; Kulkarni, S.; Freeman, K. B.; Pan, W.; Kavash, R. W.; Costanzo, M. J.; Jo, H.; Daly, T. M., Platelet factor 4 activity against P. falciparum and its translation to nonpeptidic mimics as antimalarials. *Cell host & microbe* **2012,** *12* (6), 815-823.
24. McMorran, B. J.; Burgio, G.; Foote, S. J., New insights into the protective power of platelets in malaria infection. *Commun. Integr. Biol.* **2013,** *6* (3), e23653.
25. McMorran, B. J.; Wieczorski, L.; Drysdale, K. E.; Chan, J.-A.; Huang, H. M.; Smith, C.; Mitiku, C.; Beeson, J. G.; Burgio, G.; Foote, S. J., Platelet factor 4 and Duffy antigen required for platelet killing of Plasmodium falciparum. *Science* **2012,** *338* (6112), 1348-1351.
26. McMorran, B. J., Immune role of platelets in malaria. *ISBT Science Series* **2019,** *14* (1), 67-76.

Chapter 4

1. Malaria, http://www.who.int/en/news-room/fact-sheets/detail/malaria (accessed November 16, 2019).
2. Müller, I. B.; Hyde, J. E., Antimalarial drugs: modes of action and mechanisms of parasite resistance. *Future microbiol.* **2010,** *5* (12), 1857-1873.
3. Weyrich, A. S.; Zimmerman, G. A., Platelets: signaling cells in the immune continuum. *Trends Immunol.* **2004,** *25* (9), 489-495.
4. Morrell, C. N., Understanding platelets in malaria infection. *Curr. Opin. Hematol.* **2014,** *21* (5), 445-449.
5. Grau, G. E.; Mackenzie, C. D.; Carr, R. A.; Redard, M.; Pizzolato, G.; Allasia, C.; Cataldo, C.; Taylor, T. E.; Molyneux, M. E., Platelet accumulation in brain microvessels in fatal pediatric cerebral malaria. *J. Infect. Dis.* **2003,** *187* (3), 461-466.
6. McMorran, B. J.; Marshall, V. M.; de Graaf, C.; Drysdale, K. E.; Shabbar, M.; Smyth, G. K.; Corbin, J. E.; Alexander, W. S.; Foote, S. J., Platelets kill intraerythrocytic malarial parasites and mediate survival to infection. *Science* **2009,** *323* (5915), 797-800.
7. Combes, V.; Coltel, N.; Faille, D.; Wassmer, S. C.; Grau, G. E., Cerebral malaria: role of microparticles and platelets in alterations of the blood–brain barrier. *Int. J. Parasitol.* **2006,** *36* (5), 541-546.
8. Gyulkhandanyan, A. V.; Mutlu, A.; Freedman, J.; Leytin, V., Markers of platelet apoptosis: methodology and applications. *J. Thromb. Thrombolysis* **2012,** *33* (4), 397-411.
9. Gruba, S. M.; Koseoglu, S.; Meyer, A. F.; Meyer, B. M.; Maurer-Jones, M. A.; Haynes, C. L., Platelet membrane variations and their effects on δ-granule

secretion kinetics and aggregation spreading among different species. *Biochim. Biophys. Acta Biomembr.* **2015,** *1848* (7), 1609-1618.

10.   Ge, S.; Woo, E.; White, J. G.; Haynes, C. L., Electrochemical measurement of endogenous serotonin release from human blood platelets. *Anal. Chem.* **2011,** *83* (7), 2598-2604.

11.   Ge, S.; White, J. G.; Haynes, C. L., Quantal release of serotonin from platelets. *Anal. Chem.* **2009,** *81* (8), 2935-2943.

12.   Holmsen, H.; Weiss, H. J., Secretable storage pools in platelets. *Annu. Rev. Med.* **1979,** *30* (1), 119-134.

13.   Jančinová, V.; Danihelová, E., Chloroquine: a multipotent inhibitor of human platelets in vitro. *Thromb. Res.* **2000,** *98* (5), 411-421.

14.   Osim, E.; Mbajiorgu, F.; Nkomo, I.; Coutts, A.; Munjeri, O.; Vaz, R.; Arthur, S.; Musabayane, C., The effects of chloroquine on bleeding time and disappearance of platelet 5-hydroxytryptamine in rabbits. *J. Cardiovasc. Pharmacol. Therapeut.* **2000,** *5* (3), 223-228.

15.   Robinson, D. L.; Hermans, A.; Seipel, A. T.; Wightman, R. M., Monitoring rapid chemical communication in the brain. *Chem. Rev.* **2008,** *108* (7), 2554-2584.

16.   Trouillon, R.; Passarelli, M. K.; Wang, J.; Kurczy, M. E.; Ewing, A. G., Chemical analysis of single cells. *Anal. Chem.* **2013,** *85* (2), 522-542.

17.   van Kempen, G. T. H.; van den Berg, R.; Eilers, P.; Westerink, R., Three distinct modes of exocytosis revealed by amperometry in neuroendocrine cells. *Biophys. J.* **2011,** *100* (4), 968-977.

18.   Marquis, B. J.; Haynes, C. L., The effects of co-culture of fibroblasts on mast cell exocytotic release characteristics as evaluated by carbon-fiber microelectrode amperometry. *Biophys. Chem.* **2008,** *137* (1), 63-69.

19.   Ge, S.; Woo, E.; Haynes, C. L., Quantal regulation and exocytosis of platelet dense- body granules. *Biophys. J.* **2011,** *101* (10), 2351-2359.

20.   Mockenhaupt, F. P.; May, J.; Bergqvist, Y.; Ademowo, O. G.; Olumese, P. E.; Falusi, A. G.; Großterlinden, L.; Meyer, C. G.; Bienzle, U., Concentrations of chloroquine and malaria parasites in blood in Nigerian children. *Antimicrob. Agents Chemother.* **2000,** *44* (4), 835-839.

21.   Babalola, C. P.; Bolaji, O. O.; Ogunbona, F. A.; Sowunmi, A.; Walker, O., Pharmacokinetics of quinine in African patients with acute falciparum malaria. *Pharm. World Sci.* **1998,** *20* (3), 118-122.

22.   Gruba, S. M.; Meyer, A. F.; Manning, B. M.; Wang, Y.; Thompson, J. W.; Dalluge, J. J.; Haynes, C. L., Time-and concentration-dependent effects of exogenous serotonin and inflammatory cytokines on mast cell function. *ACS Chem. Biol.* **2014,** *9* (2), 503-509.

23.   Kawagoe, K. T.; Zimmerman, J. B.; Wightman, R. M., Principles of voltammetry and microelectrode surface states. *J. Neurosci. Meth.* **1993,** *48* (3), 225-240.

24.   Jancinova, V.; Nosal, R.; Petrikova, M., On the inhibitory effect of chloroquine on blood platelet aggregation. *Thromb. Res.* **1994,** *74* (5), 495-504.

25.   Bradley, C.; Deacon, S.; Connellan, J.; Thurlow, P., Electron microscopic studies of quinine induced ultrastructural changes to platelets. *Thromb. Res.* **1991,** *63* (5), 563-568.

26.   Connellan, J.; Deacon, S.; Thurlow, P., Changes in platelet function and r eactivity induced by quinine in relation to quinine (drug) induced immune thrombocytopenia. *Thromb. Res.* **1991,** *61* (5-6), 501-514.

27.   McMorran, B. J.; Wieczorski, L.; Drysdale, K. E.; Chan, J.-A.; Huang, H. M.; Smith, C.; Mitiku, C.; Beeson, J. G.; Burgio, G.; Foote, S. J., Platelet factor 4 and

Duffy antigen required for platelet killing of Plasmodium falciparum. *Science* **2012,** *338* (6112), 1348-1351.

28. Pretorius, E.; Humphries, P.; Ekpo, O.; Smit, E.; Van der Merwe, C. F., Comparative ultrastructural analyses of mouse, rabbit, and human platelets and fibrin networks. *Microsc. Res. Tech.* **2007,** *70* (9), 823-827.

29. Leytin, V.; Allen, D.; Lyubimov, E.; Freedman, J., Higher thrombin concentrations are required to induce platelet apoptosis than to induce platelet activation. *Br. J. Haematol.* **2007,** *136* (5), 762-764.

30. Mackman, N.; Gruber, A., Platelet polyphosphate: an endogenous activator of coagulation factor XII. *J. Thromb. Haemostasis* **2010,** *8* (5), 865.

Kang Xiong-Hang

4479 Atlas Trail, Woodbury, MN 55129

Cell: (651) 278 – 9485   E-mail: xion1300@umn.edu

EDUCATION

Chemistry Ph.D., University of Minnesota, Twin Cities,		Minneapolis, MN
Advisor:	Christy L. Haynes	
GPA:	3.449	
Graduation:	Aug 2020	
Chemistry M.S., University of Minnesota, Twin Cities,		Minneapolis, MN
Advisor:	Christy L. Haynes	
GPA:	3.449	
Graduation:	Feb 2017	
Chemistry M.S., California State University, Fresno,		Fresno, CA
Advisor:	Joy J. Goto	
GPA:	4.000	
Graduation:	Dec 2013	
Chemistry B.A., California State University, Fresno,		Fresno, CA
GPA:	3.720	
Graduation:	May 2011	
Honors:	Magna Cum Laude	

AWARDS & SCHOLARSHIPS

NIH Biotechnology Training Grant	2017 - 2019
Diversity of Views and Experiences Fellowship	2015 - 2016
Outstanding Graduate Student, CSUF, Fresno	2013
NSF Graduate Scholarship	2011 - 2013
Faculty Sponsored Student Research Award	2011 - 2013
Graduate rGrant	2011 - 2012
Fresno State Asian Faculty and Staff Association Award	2012
President's List	2009 - 2011
Dean's List	2007 - 2008

RESEARCH EXPERIENCE

Graduate Student Researcher, UMN, Twin Cities   2015 - 2020
    Mentor: Christy L. Haynes, Ph.D.
    Platelet involvement in malaria
- Study the role of platelets during malarial infection and their responses to common anti-malarial drugs

    Mast cell involvement in malaria

- Study the responses of mast cells during malarial infection

Antimalarial drugs on platelet
- Study the role of platelets during malarial infection and their responses to common anti-malarial drugs
- Cholesterol depletion in platelets
- Study cholesterol depletion affects the shapes of platelets and functions

Multiplex electrode sensors development
- Work with electrical engineers and neuroscientists to develop a device to measure brain activity and neurotransmitter levels

Graduate Student Intern, Boston Scientific, Maple Grove, MN   2020
    Mentors: Andrew Ro, Ph.D., Audrey Meyer, Ph.D.
    Drug coating characterization and method development

Graduate Student Researcher, CSU, Fresno, Fresno, CA   2011 - 2013
    Mentor: Joy J. Goto, Ph.D.
    β-methylamino-L-alanine (BMAA) and oxidative stress
- Study the effects of BMAA in inducing oxidative stress in *Drosophila melanogaster*

BMAA and metal chelation
- Study the effect of BMAA on metal chelation

BMAA and viability
- Study the dosage dependent and long-term effects of BMAA in *Drosophila melanogaster* viability and locomotion

Student Researcher, Agriculture & Priority Pollutants Laboratories, Clovis, CA   2011
    Mentor: Eric Person, Ph.D.
- Field water collection and analysis
- Collected, analyzed, and interpreted field water samples for appearance, pH, viscosity, metals, and volatile compounds

Academic Research Associates, UCSF Fresno Medical, Fresno, CA   2010
    Medical research in the emergency department
- Assisted with patient data collection

TEACHING EXPERIENCE

General Chemistry Lab TA, Department of Chemistry, UMN, Twin Cities   2016 - 2017
- General chemistry laboratory teaching and tutoring including student evaluation and records

General Chemistry Lab TA, Department of Chemistry, CSU, Fresno   2011 - 2013
- General chemistry laboratory teaching and tutoring including student evaluation and records

PUBLICATIONS

- <u>Xiong-Hang, K.</u>; Haynes, C.L., *Plasmodium chabaudi* Affects Mast Cell Degranulation as Measured by Carbon Fiber Microelectrode Amperometry. *In Preparation.*
- Gruba, S.M.; Wu, X.; <u>Xiong-Hang, K</u>.; Spanolios, E.; He, J.; Haynes, C.L., Platelets in Asthma: Platelet Response to Allergens, CXCL10, and CCL5. *In preparation.*

- Gruba, S.M.; Francis, D.H.; Meyer, A.F.; Meyer, B.M.; Kim, D.; Spanolios, E.; He, J.; X<u>iong-Hang, K</u>.; Haynes, C.L., Characterization of the Presence and Function of Platelet Opioid Receptors. *In preparation*.
- <u>Xiong-Hang, K</u>.; He, J.; Kemnetz-Ness, K.; Haynes, C., Antimalarial Drugs Impact Chemical Messenger Secretion by Blood Platelets. *Biochem. Biophys. Rep.* **2020,** *22*, 100758.
- <u>Xiong-Hang, K</u>.; Kemnetz-Ness, K.; Krieger, A. C.; Haynes, C. L., Insight into the Effects of *Plasmodium chabaudi* on Platelets Using Carbon-Fiber Microelectrode Amperometry. *ACS Infect. Dis.* **2019,** *5* (4), 592-597.
- McGillis, E.; Arens, A.; Olives, T.; Gray, T.; Blanchard, S.; Love, S. A.; Haynes, C. L.; <u>Xiong-Hang, K</u>.; Lee, A.; Cole, J. Rapid-Onset Hyperthermia and Hypercapnea Peceding Rigor Mortis and Cardiopulmonary Arrest in a DNP Overdose, *Clin. Toxicol.* **2018**, 994-995.

PRESENTATIONS

Chemistry Biology Interface Training Grant Symposium, UMN, Twin Cities	2020
Exploring Platelets Response to Malaria and Antimalarial Drugs Using Electrochemical Techniques	
Graduate Student Research Symposium, UMN, Twin Cities	2018
Exploring Platelet Response to Malaria at the Single Cell Level	
Pittcon, Orlando, FL	2018
Exploring Platelet Response to Malaria and Common Antimalarial Drugs at the Single Cell Level	
IEM Annual Conference and Retreat, UMN, Twin Cities	
Exploring Platelets Response to Malaria at the Single Cell Level	2017
Exploring the Effects of Chloroquine and Quinine on Platelets Using Electrochemical Techniques	2018
245th ACS National Meeting & Exposition, New Orleans, LA	Apr 2013
Induced oxidative stress in *Drosophila melanogaster* exposed to an environmental neurotoxin	
Graduate Research & Creative Activities Symposium, CSU, Fresno	May 2013
Oxidative stress in *Drosophila melanogaster* exposed to the environmental neurotoxin β-N-methylamino-L-alanine (BMAA)	
College of Science and Mathematics Academic Assembly and Poster Session, CSU, Fresno	
Detection of CuZnSOD in mutant and wild type *Drosophila melanogaster* using western blot and in-gel-activity assay	2012
Induced oxidative stress in *Drosophila melanogaster* exposed to an environmental neurotoxin	2013
32nd Annual Central California Student Research Symposium, CSU, Fresno	Mar 2012
Detection of CuZnSOD in mutant and wild type *Drosophila melanogaster* using western blot and in-gel-activity assay	
9th International Conference on Plant Medicine, St. George, UT	Oct 2012
Induced oxidative stress in *Drosophila melanogaster* exposed to an environmental neurotoxin	

RELEVANT COURSEWORK

Analytical Spectroscopy   Biochemistry

Chemical Biology	Genetics
Physical Chemistry	Cell Biology
Electrochemistry	Immunology
Atmospheric Chemistry	Biology
Adv. Organic Chemistry	Calculus I, I, III
General Chemistry	Physics
Analytical Chemistry	System Biology
Instrumental Analysis	

TECHNICAL SKILLS

Lab: HPLC, UV-vis spectrometer, TEM, SEM, cell culture, ELISA assays, SDS-PAGE, CFMA, Microscopy, aggregometer, pH meter, Viscometer, animal handling (mouse and fruit flies), ICP-MS, Western blots, colorimetric assays
Data Analysis: Microsoft Word, Microsoft Excel, Microsoft PowerPoint, GraphPad Prism, ImageJ, Mini Analysis Program

SYNERGISTIC ACTIVITIES

Lab Safety Officer	2019 - 2020
• Analysis & Compliance Committee Member	
The Council for the Advancement of Underrepresented Scientists and Engineers co-founder	2017 - 2020
American Chemical Society	2013 - 2014
Engineers Without Boarders Club	2010 - 2011
Health Career Opportunity Program	2007 - 2011
Educational Opportunity Program	2006 - 2011
Hmong Nationalities Organization	2013 - 2015
• Planner for the 1st Empowering Youth Conference	
The Leukemia and Lymphoma Society, Fresno, CA	2010 - 2013
• Fresno County Cancer Resource Guide development (English & Hmong)	